Doctoral theses at NTNU, 2014:76

Dmitry Lysenko

On Numerical Simulation of Turbulent Flows and Combustion

Doctoral Thesis

Dmitry Lysenko

ISBN 978-82-326-0076-2 (printed version)
ISBN 978-82-326-0077-9 (electronic version)
ISSN 1503-8181

NTNU – Trondheim
Norwegian University of
Science and Technology

NTNU
Norwegian University of Science and Technology
Thesis for the degree of Philosophiae Doctor
Faculty of Engineering Science & Technology
Department of Energy and Process Engineering

Doctoral theses at NTNU, 2014:76

NTNU

NTNU – Trondheim
Norwegian University of
Science and Technology

Dmitry Lysenko

On Numerical Simulation of Turbulent Flows and Combustion

Thesis for the degree of Philosophiae Doctor

Trondheim, February 2014

Norwegian University of Science and Technology
Faculty of Engineering Science & Technology
Department of Energy and Process Engineering

NTNU – Trondheim
Norwegian University of
Science and Technology

NTNU
Norwegian University of Science and Technology

Thesis for the degree of Philosophiae Doctor

Faculty of Engineering Science & Technology
Department of Energy and Process Engineering

ISBN 978-82-326-0076-2 (printed version)
ISBN 978-82-326-0077-9 (electronic version)
ISSN 1503-8181

Doctoral theses at NTNU, 2014:76

Printed by Skipnes Kommunikasjon as

Abstract

The goal of the present doctoral thesis was to develop a turbulence-chemistry interaction model for turbulent combustion simulations for high Reynolds number flows of practical interest. Present simulations were carried out using the unsteady Reynolds-averaged Navier-Stokes (URANS) and the Large Eddy Simulation (LES) formulations. The compressible flow treatment was used for both cases in order to model the coupling between hydromechanics and thermodynamics. The transient Navier-Stokes equations were applied to catch up unsteady combustion physics properly. The interaction between turbulence and chemistry was modeled based on the Eddy Dissipation Concept (EDC) with a detailed chemistry treatment. The open source OpenFOAM toolbox was used as the main frame for mathematical modeling and numerical simulations.

First, non-reacting turbulent bluff-body flows were investigated with the goal of validation, verification and understanding of the capabilities of the numerical method using the conventional URANS approach. These results were analyzed in detail and agreed fairly well with experimental data.

Then, the validation of the URANS approach (based on the standard k-ϵ model) was extended for reacting turbulent flows: the Sandia Flame D, the Sandia Flame CHNa and the Sydney Bluff-Body Flame HM1E. The chemistry was described by the full GRI-3.0 mechanism. There was relatively good agreement between simulations and measurements and it is believed that one of the main reasons for the observed discrepancies was the round-jet anomaly of the standard k-ϵ model.

Furthermore, the numerical method was extended to a large-eddy simulation model. A sub-critical circular cylinder flow at a Reynolds number Re $= 3.9 \times 10^3$ and a Mach number M $= 0.2$ was simulated to evaluate the applicability of the implemented LES approach. In general, the LES results agreed fairly well with the available experimental and numerical data and gave an indication of the adequacy and the accuracy of the implemented method.

As a next step, LES validation was extended for a modest sub-critical circular cylinder flow at Re $= 2 \times 10^4$. Both an incompressible and a compressible (M $= 0.2$) flow treatment was used. The predicted results revealed significant inaccuracies like spurious oscillations of the compressible flow solution. The incompressible flow results were found to be consistent with the existing LES studies as well as with measurements.

Testing of the non-reflecting boundary conditions was performed for the Aeolian tones aeroacoustic predictions. The laminar flow over a circular cylinder at Re $= 140$ and M $= 0.2$ was calculated by direct solution of the unsteady compressible Navier-Stokes equations. The sound generated by a circular cylinder at Re $= 2.2 \times 10^4$ and M $= 0.2$ was predicted using LES. The calculated acoustic fields showed a dipole directivity, similar to a natural vortex shedding. The impact of the Doppler effect was investigated and discussed as well. In general, (in spite of spurious oscillations in the near field) the computed aerodynamic and far-field acoustic results were found to be in satisfactory agreement with measurements and analytical relationships.

Finally, the method was extended for the turbulent reactive flow predictions using LES. The LES formulation of the Eddy-Dissipation Concept was proposed. The validation was performed for the Sandia Flame D, where reasonable agreement between predicted and measured data was achieved. It is believed, that the observed discrepancies were related with the lack of grid resolution and inaccurate boundary conditions for the turbulence at inlet boundaries.

Preface

This thesis is submitted to the Norwegian University of Science and Technology (NTNU) for partial fulfilment of the requirements for the degree of philosophiae doctor. This doctoral work has been performed at the Department of Energy and Process Engineering, NTNU, Trondheim, with Ivar S. Ertesvåg as main supervisor and Kjell Erik Rian as co-supervisor. This PhD was conducted as part of CenBio Center for environmentally friendly energy and funded by NTNU.

Trondheim, February 2014

Dmitry Lysenko

Acknowledgements

I would like to thank my supervisor, Professor Ivar S. Ertesvåg, for trusting me to pursue my own ideas and thoughts, and for his continuous interest and support. Thanks are also due to my co-supervisor, Dr. Kjell Erik Rian, for his valuable support, fruitful discussions and inspiring enthusiasm.

I am pleased to express my acknowledgment to Dominik Christ and Bjørn Lilleberg for the further possibility to develop the Eddy-Dissipation Concept in OpenFOAM. Special thanks to Dominik Christ for the useful advises regarding model implementation and critical remarks of one of my manuscripts.

The Norwegian Notur project (national infrastructure for computational science in Norway) and the NTNU HPC team are also thanked for making the present simulations possible. Special thanks to the people from the faculty IT department for their help and support with different IT issues.

My wife, Elena, deserves special thanks for their support and understanding during these years of study. A special thanks go to my mother for permanent pushing me to complete my PhD project.

Finally, I would like to thank all the co-workers. My gratitude goes out to all these colleagues.

Papers and presentations

Papers included in thesis

Paper A - Lysenko, D.A., Ertesvåg, I.S., Rian, K.E., Modeling of turbulent separated flows using OpenFOAM. Comput. Fluids, 80, 408-422 (2013)

Paper B - Lysenko, D.A., Ertesvåg, I.S., Rian, K.E., Numerical simulation of turbulent flames using the Eddy Dissipation Concept, *Submitted to a journal*

Paper C - Lysenko, D.A., Ertesvåg, I.S., Rian, K.E., Large-eddy simulation of the flow over a circular cylinder at Reynolds number 3900 using the OpenFOAM toolbox, Flow Turbul. Combust., 89, 491–518 (2012)

Paper D - Lysenko, D.A., Ertesvåg, I.S., Rian, K.E., Large-eddy simulation of the flow over a circular cylinder at Reynolds number 2×10^4, Flow Turbul. Combust., DOI 10.1007/s10494-013-9509-1

Paper E - Lysenko, D.A., Ertesvåg, I.S., Rian, K.E., Towards simulation of far-field aerodynamic sound from a circular cylinder using OpenFOAM, Accepted for publication in Int. J. Aeroacoustics

Paper F - Lysenko, D.A., Ertesvåg, I.S., Rian, K.E., Numerical simulations of the Sandia Flame D using the Eddy-Dissipation Concept, *Submitted to a journal*

Identification of the candidate's contribution on joint papers

Ivar S. Ertesvåg and Kjell Erik Rian are my main supervisor and co-supervisor, respectively. Their contribution in writing these papers has been discussions, suggestions and critical review.

Conference papers with peer review

Lysenko, D.A., Ertesvåg, I.S., Rian, K.E., Testing of OpenFOAM CFD code for plane turbulent bluff body flows within conventional URANS approach, Proceedings: 8th International Conference on CFD in Oil and Gas, Metallurgical and Process Industries, Trondheim, 2011, ISBN 9788214052626 (SINTEF Report A22601).

Lysenko, D.A., Ertesvåg, I.S., Rian, K.E., Turbulent bluff body flows modeling using OpenFOAM technology, MekIT'11, Sixth National Conference on Computational Mechanics, 23-24 May, 2011, Trondheim, Norway.

Lysenko, D.A., Ertesvåg, I.S., Rian, K.E., Lilleberg, B., Christ, D., Numerical simulation of turbulent flames using the Eddy Dissipation Concept with detailed chemistry, MekIT'13, 7th National Conference on Computational Mechanics, 13-14 May, 2013, Trondheim, Norway.

Presentations

Lysenko, D.A., Ertesvåg, I.S., Rian, K.E., Turbulent separated flows modeling using OpenFOAM and ANSYS FLUENT technologies in HPC environment, 23rd International Conference on Parallel Computational Fluid Dynamics 2011. May 16-20, 2011, Barcelona, Spain.

Lysenko, D.A., Ertesvåg, I.S., Rian, K.E., Large-eddy simulation of the flow past a circular cylinder at Reynolds numbers 3900, 20000 and 140000, Proceedings: 4th International Workshop "Computational Experiment in Aeroacoustics", 19-22 September, 2012, Svetlogorsk, Russia.

Lysenko, D.A., Ertesvåg, I.S., Rian, K.E., Large-eddy simulation of the flow over a circular cylinder at Reynolds number 3900, Proceedings: 7th OpenFOAM Workshop, 25-28 June, 2012, Darmstadt, Germany.

Lysenko, D.A., Ertesvåg, I.S., Rian, K.E., Turbulent combustion modeling using the Eddy Dissipation Concept with detailed chemistry, MCS'13, Eighth Mediterranean Combustion Symposium, 9-13 September, 2013, Çeşme, Izmir, Turkey.

Lysenko, D.A., Ertesvåg, I.S., Rian, K.E., Advancing Turbulent Combustion Modeling Using the Eddy Dissipation Concept with Detailed Chemistry, OSCIC'13, Seventh Open Source CFD International Conference, 24th-25th October, 2013, Hamburg, Germany

Contents

Chapter 1

Introduction

1.1 General background and motivation

The present study is part of CenBio (Bioenergy Innovation Centre) project, which aims to develop technology for increased, sustainable use of bioenergy. This means both that the efficiency of energy conversion in combustion plants has to be improved, and that the formation of pollutants (e.g. NOx and CO) has to be controlled and reduced. Hence, improved combustion technology is needed, which requires deeper understanding and more accurate and more detailed prediction methods.

Improved efficiency of biomass energy conversion can be achieved by gasification of biomass and subsequent combustion in gas turbines. This has similarities with, but also distinctions from, coal- and natural-gas utilization. Efficient and clean utilization of biomass depends (among other) on combustion technologies. Both with regards to these technologies and in general, abatement of pollutants such as NOx is important. This requires a deeper understanding of the basic processes of turbulent reacting flows. The underlying challenges include the flame behavior, turbulence mixing properties, flame stability (including extinction/ ignition and combustibility of certain mixtures) at high pressure, peak temperatures, pollutant formation, etc.

Computational modeling of turbulent combustion comprises modeling of the turbulent flow ("turbulence model", mixing, acoustics, etc.), the turbulence-combustion interaction ("combustion model"), chemistry model (kinetics, including extinction, pollutant formation, etc.), radiation modeling, and numerical solvers. Computational Fluid Dynamics (CFD) is used as the main framework for numerical modeling in the present study. The Eddy Dissipation Concept of turbulent combustion (EDC) developed by Bjørn F. Magnussen and coworkers at NTNU and SINTEF over nearly four decades has become the standard model for turbulent combustion in state-of-the-art commercial CFD codes. Although considerable success, there is still potential for its further development.

The present study has emphasis on advancing the modeling of interactions between tur-

bulence and reactions by integrating current practice of chemical kinetics into new combustion models.

1.2 Turbulent combustion modeling

The number of works dealing with unsteady turbulent non-reacting and reacting flows have grown tremendously over the past few decades mainly due to increase computational capabilities of modern computers, improvement in accuracy and efficiency of numerical methods and advancing in modeling of turbulent flow features [26]. From the modeling point of view, several approaches are existed to model non-reacting and reacting turbulent flows.

The conventional Reynolds-averaging simulations (RAS) may be considered as the most popular approach by now. One of the most important scientific achievements of the CFD in the 1980s was a numerical solution of the diffusion problem, associated with approximation errors of convective terms. An application of schemes with a low numerical viscosity (etc., second-order upwind schemes [83]) became a necessary condition to obtain an accurate results in simulation of turbulent separated flows.

Progress in computational engineering and, especially, widespread usage of personal computers in the 1980s and subsequent years have made it possible to develop general purpose CFD codes, such as PHOENIX, FLOW3D, FIDAP etc. Moreover, when computers with a large memory and a high speed processors appeared, instead of the Navier–Stokes equations in transformed variables, Navier-Stokes equations written in physical variables – Cartesian velocity and pressure components – began to be predominantly used. Moreover, this made it possible to substantially (by an order of magnitude and more) increase the number of computational cells in numerical simulations [35].

In spite of the rapid progress in the computational (parallel) systems there are engineering problems (etc., gas turbine combustors) where an achievement of the grid independent solution is quite difficult still even for RAS [54], [55]. The gas turbine combustor is an excellent example of multi-physics and multi-scales applications where a wide spectrum of length and time scales may vary in several orders of magnitude [54], [55]. Many of mathematical models for the turbulence, the turbulence-chemistry interaction, radiative heat transfer, soot formation and etc. designed for RAS are not perfect and their further development is not yet finished. Moreover, the boundaries of applicability of the majority of models are also not clearly understood. Furthermore, new, advanced combustion technologies require further development and improvement and testing of the acceptability of mathematical models.

Another approach, the large-eddy simulation (LES) is the most suitable and sophisticated approach to obtain the medium-cost three-dimensional unsteady solution of the turbulent flows, which was pioneered to compute meteorological flows in the 1950s and the early 1960s [25]. In spite of the fact that LES has been developed over a few decades, the first

rigorous derivation of the LES governing equations in general coordinates was published only in 1995 [74]. However, up to the present, the number of available fundamental monographs in the literature (e.g., the books by P. Sagaut, Large eddy simulation for incompressible flows, Springer, B. Geurts, Elements of direct and large-eddy simulations, Edwards, E. Garnier, N. Adams and P. Sagaut, Large eddy simulation for compressible flows, Springer) shows that LES was recognized as a power tool in fundamental and applied research as well as in engineering analysis.

One of the main issues (besides the mathematical models, definition of boundary conditions, the coupling with numerical errors, etc.) raised by LES is a closure problem [26], [74], [25]. Development of the adequate subgrid scale models of LES has been the main area of investigation since the 1960s, and numerous closures, have been proposed (e.g. Smagorinsky model [77]).

Most existing subgrid models have been built based on the physics of the direct kinetic energy cascade from large to small scales observed in isotropic turbulence and high-Reynolds fully developed turbulent flows [25]. In general, the very large number of existing physical models, referred to as subgrid models are distinguished between two main groups such as functional and structural models [74]. However, the most popular paradigm for interscale energy transfer modeling is the sub-grid viscosity yet, and several models of this type are utilized in the present study.

The vast majority of existing works dealing with sub-grid modeling use the incompressible flow treatment. Some extension was done for variable-density flows (e.g. for meteorological flows) and low-speed reacting flows. However the problem is much more complex when compressible flows are considered: the number of mathematical and physical symmetries of the continuous equations to be preserved by the numerical method is larger than in the incompressible case, and that additional constraints, such as preservation of fundamental thermodynamic laws, arise [26], [25]. For the compressible LES, both the numerical method and the sub-grid models, or at least their sum, should satisfy these new requirements [25]. Another point is that many popular numerical methods (e.g. convective linearUpwind schemes [83]) designed to compute flows with shocks within the conventional Reynolds-averaged Navier-Stokes (RANS) approach have been observed to be badly suited for LES purposes, since they are too dissipative.

LES of compressible flows remains unexplored, and based on variable density extensions of models, methods and paradigms developed within the incompressible-flow framework and limitations of the available compressible LES theory are evident, and may prohibit improvement of the results in many cases [26], [25]. However, the coupling between thermodynamics and hydrodynamics is important, especially for combustion applications.

Combustion LES are providing an effective platform for modeling the entire spectrum of turbulent reacting flows [80], [26], [25]. Relevant sub-grid scale models for combustion are being developed but a universally accepted model is not yet available as well as for combustion models (turbulence-chemistry interaction) [18]. In the present study one of the most widely-used combustion models is the Eddy Dissipation Concept (EDC) [19]

is used. The advantages of this model are that it is relatively easy to implement in CFD codes, it is computationally fast, and it is tractable with complex chemistry. Moreover, the concept is readily adaptable for use with LES and represents a great potential for the prediction of premixed combustion.

In most cases chemical reactions occur on time scales which are much wider than that of the flow and the molecular transport processes [82]. Therefore, information is needed about the chemical kinetics (the rate of chemical reactions). Detailed mechanisms for even moderately complex hydrocarbons (C7 and C8) contain hundreds of species reacting through thousands of reactions and involve complex paths in conversion of fuel and oxidants, via intermediate species, to products. Chemical systems exhibit strong nonlinear dependency towards temperature and pressure, which can not be described by very simplified one-step global reactions [82]. For this purpose the concept of the perfectly stirred reactor (PSR) model [48] is integrated with EDC. The PSR model assumes that perfect mixing is achieved instantaneously inside the combustor, and the properties inside the combustor are uniform. The advantage of using of PSR for turbulent combustion is that effects of chemical kinetics are isolated and in detail.

Another interesting aspect of the turbulent combustion phenomena is the radiation. Most practical combustion devices operate at high temperatures where the thermal radiation plays an important role. The interactions between chemistry, turbulence and radiation arise due to nonlinear coupling between the fluctuations of temperature, radiative intensity and species concentrations. This coupling results in higher heat loss due to increased radiative emission and reduced temperatures [46]. Consequently, accurate prediction of the temperature is key point for pollution species (e.g. Nox, CO, Sox) [23] and heat transfer calculations.

The fact that the combustion involves nonlinear interaction of turbulent mixing, heat transfer and chemistry, which makes it not only a highly multidisciplinary topic, but also a highly challenging one. The scientific problem of turbulent combustion has been nominated as one of the "Grand Challenges" problems [87] to be solved using high performance computing (HPC) facilities. The quality of parallel implementation of the numerical method becomes of great importance due to impossibility to solve combustion LES problems using usual desktop computers.

The implemented numerical method incorporates all physical aspects of the turbulent combustion phenomena. The turbulence is treated with the filtered compressible Navier-Stokes equations. However, the incompressible sub-grid scales hypothesis, which assumes that the compressibility affects only large scales, is utilized, since the present simulations are carried out at the low-Mach number limit. An one equation eddy-viscosity model [91],[26] is used for the closure problem. The turbulence-chemistry interaction is based on the Eddy-Dissipation concept [19] which assumes that combustion takes place in the 'fine structures'. Detailed chemical kinetics mechanisms are used to describe the chemical system based on the concept of PSR [48]. The radiation is included in simulations as well using a simple P-1 approximation [12]. The parallelization of the method is based on the message-passing interface (MPI) [87] and demonstrates its high efficiency

(approximately 70% from the ideal) both for reacting and non-reacting cases at the Vilje HPC facility (www.notur.no) which is comparable with the state-of-the-art commercial CFD solvers.

Chapter 2

Mathematical modeling and numerical methods

2.1 Reacting flows - fundamentals

In this section the fundamental governing equations for reacting compressible flows for the Reynolds-averaged and Large-eddy simulations are presented. All calculations of the present thesis were carried out in the frame of the Computational Fluid Dynamics (CFD). The Cartesian tensor notation, where t and x_i are independent variables representing time and spatial coordinates of a Cartesian coordinate system **x**, is used.The three components of the velocity vector **u** are denoted $u_i \quad (i = 1, 2, 3)$. The summation convection over repeated indices applies unless otherwise is noted.

2.2 URANS for turbulent combustion modeling

2.2.1 Governing equations

The Favre-averaged (i.e. mass-density-weighted) equations of mass, momentum and energy for the turbulent compressible flows are:

$$\frac{\partial \bar{\rho}}{\partial t} + \frac{\partial \bar{\rho}\tilde{u}_j}{\partial x_j} = 0 \tag{2.1}$$

$$\frac{\partial \bar{\rho}\tilde{u}_i}{\partial t} + \frac{\partial \bar{\rho}\tilde{u}_i\tilde{u}_j}{\partial x_j} = -\frac{\partial \bar{p}}{\partial x_i} + \frac{\partial}{\partial x_j}\left(\bar{\tau}_{ij} - \bar{\rho}\widetilde{u_i'' u_j''}\right) \tag{2.2}$$

$$\frac{\partial \bar{\rho}\tilde{h}}{\partial t} + \frac{\partial \bar{\rho}\tilde{h}\tilde{u}_j}{\partial x_j} = \frac{\partial}{\partial x_j}\left(\bar{\rho}\alpha\frac{\partial \tilde{h}}{\partial x_j} - \bar{\rho}\widetilde{u_j'' h''}\right) - \frac{\partial}{\partial x_j}\left(\bar{q}_r\right) + \bar{S}_{hc} \tag{2.3}$$

Here, the overbar denotes Reynolds averaging, while the tilde denotes Favre averaging: ρ denotes the density, $\mathbf{u}$ is the velocity, p is the pressure, $h = \sum_s Y_s \int C_{p,s}\ dT$ is the enthalpy, T is the temperature, Y_s is the species mass fraction, $C_{p,s}$ is the heat capacity for species s in the mixture, α is the thermal diffusivity, q_r represents the radiative heat loss and S_{hc} represents the source term due to combustion.

Here, $C_{p,s}$ is calculated as a function of temperature from a set of coefficients taken from NIST-JANAF thermochemical tables [10]. The thermal diffusivity is modeled as

$$\bar{\rho}\alpha = \mu \frac{C_v}{C_{pBar}} \left(1.32 + 1.77 \frac{R}{C_v}\right), \tag{2.4}$$

where μ is the molecular viscosity (calculated according to the Sutherland law), R is the gas constant, C_v represents heat capacity at constant volume and

$$C_{pBar} = \frac{\partial\tilde{T}\partial\tilde{h} + C_p}{\left(\partial\tilde{T}\right)^2 + 1}. \tag{2.5}$$

Here, $\partial\tilde{T} = \tilde{T} - T_{ref}$, $\partial\tilde{h} = \tilde{h}\,(T) - \tilde{h}\,(T_{ref})$ and C_p is the mixture heat capacity at constant pressure.

The stress tensor for a Newtonian fluid is expressed as

$$\bar{\tau}_{ij} = \mu \left(\frac{\partial\tilde{u}_i}{\partial x_j} + \frac{\partial\tilde{u}_j}{\partial x_i}\right) - \frac{2}{3}\mu\delta_{ij}\frac{\partial\tilde{u}_k}{\partial x_k}, \tag{2.6}$$

where δ_{ij} is the Kronecker symbol.

$\bar{S}_{hc}$ is modeled according to

$$\bar{S}_{hc} = -\sum_{s=1}^{N} \frac{\bar{\omega}_s}{M_s} h^{\theta}_{f,s}\ , \tag{2.7}$$

where $h^{\theta}_{f,s}$ is the species formation enthalpy, M_s is the species molecular weight and ω_s is the species reaction rate.

The turbulence flux $\widetilde{u''_j h''}$ is derived according to the gradient hypothesis

$$-\bar{\rho}\widetilde{u''_j h''} \approx \frac{\mu_t}{\mathrm{Pr}_t}\frac{\partial\tilde{h}}{\partial x_j} \tag{2.8}$$

where μ_t is the turbulence viscosity and Pr_t is a turbulence Prandtl number (here $\mathrm{Pr}_t = 0.7$).

For a mixture of N_s species (where $s = 1 \ldots N_s$), a transport equation for the mean mass fraction of an individual species Y_s can be defined according to

$$\frac{\partial\bar{\rho}\tilde{Y}_s}{\partial t} + \frac{\partial\bar{\rho}\tilde{Y}_s\tilde{u}_j}{\partial x_j} = \frac{\partial}{\partial x_j}\left(\left(\bar{\rho}D_{m,s} + \frac{\mu_t}{\mathrm{Sc}_t}\right)\frac{\partial\tilde{Y}_s}{\partial x_j}\right) + \bar{\omega}_s,\ s = 1, \ldots, N_s \tag{2.9}$$

where $D_{m,s}$ is the mass diffusion coefficient for species s in a mixture, Sc_t is the turbulence Schmidt number ($\mathrm{Sc}_t = \mu_t/\rho \mathrm{D}_t$, where D_t is a turbulence diffusivity). Here, Fick's law is introduced and the diffusion coefficient was set equal for all species, $D_{m,s} = D_m = 2.88\times10^{-5}$ m^2/s. The turbulence Schmidt number was set to 0.7. Finally, the temperature is related to the density and the pressure by the ideal gas law.

The Reynolds stresses are modeled according to

$$\widetilde{\bar{\rho} u_i'' u_j''} = -\mu_t \left(\frac{\partial \tilde{u}_i}{\partial x_j} + \frac{\partial \tilde{u}_j}{\partial x_i} - \frac{2}{3}\delta_{ij} \frac{\partial \tilde{u}_k}{\partial x_k} \right) + \frac{2}{3}\bar{\rho}\tilde{k}\delta_{ij} \tag{2.10}$$

The standard k-ϵ model [44] is based on the turbulence kinetic energy ($\tilde{k}$) and its dissipation rate ($\tilde{\epsilon}$). The turbulence viscosity is defined here as $\mu_t = C_\mu \bar{\rho}\tilde{k}^2/\tilde{\epsilon}$.

The modeled transport equations are:

$$\frac{\partial \bar{\rho}\tilde{k}}{\partial t} + \frac{\partial \bar{\rho}\tilde{k}\tilde{u}_j}{\partial x_j} = \frac{\partial}{\partial x_j}\left(\left(\mu + \frac{\mu_t}{\sigma_k} \right) \frac{\partial \tilde{k}}{\partial x_j} \right) + G - \bar{\rho}\tilde{\epsilon} \tag{2.11}$$

$$\frac{\partial \bar{\rho}\tilde{\epsilon}}{\partial t} + \frac{\partial \bar{\rho}\tilde{\epsilon}\tilde{u}_j}{\partial x_j} = \frac{\partial}{\partial x_j}\left(\left(\mu + \frac{\mu_t}{\sigma_\epsilon} \right) \frac{\partial \tilde{\epsilon}}{\partial x_j} \right) + C_{\epsilon 1}\frac{\tilde{\epsilon}}{\tilde{k}} G - C_{\epsilon 2}\bar{\rho}\frac{\tilde{\epsilon}^2}{\tilde{k}} \tag{2.12}$$

where the rate of turbulence kinetic energy production G is given as

$$G = -\bar{\rho}\widetilde{u_i'' u_j''}\frac{\partial \tilde{u}_i}{\partial x_j} \tag{2.13}$$

The standard values [44] are used for the model constants C_μ,$C_{\epsilon 1}$, $C_{\epsilon 2}$, σ_k and σ_ϵ.

2.2.2 EDC for turbulent combustion

The Eddy Dissipation Concept for turbulent combustion [57],[19] is based on the energy cascade model [71]. The EDC assumes that molecular mixing and chemical reactions occur in the fine structures of the turbulent flow where the smallest dissipative eddies are present. The characteristic length L^* and velocity u^* scales of the fine structures are of the same order of magnitude as the Kolmogorov scales and can be expressed as

$$L^* = \frac{2}{3}\left(\frac{3C_{D2}^3}{C_{D1}^2} \right)^{1/4} \left(\frac{\nu^3}{\tilde{\epsilon}} \right)^{1/4} \tag{2.14}$$

$$u^* = \left(\frac{C_{D2}}{3C_{D1}^2} \right)^{1/4} (\nu\tilde{\epsilon})^{1/4} \tag{2.15}$$

where $C_{D1} = 0.134$ and $C_{D2} = 0.5$ [19]. The RANS-based EDC assumes that the full cascade takes place at each numerical cell, and the connection between the fine structure and the larger eddies is achieved through the cascade. Thus, characteristics of the large

eddies such as the velocity u' are evaluated using the turbulence model (in the present case, the standard $k-\epsilon$ model).

In the model expressed below, different superscripts refer to states inside the fine structures (*), the surroundings ($\circ$) and the mean values of the computational cell ($\sim$).

The ratio between the mass in the fine structures and the total mass is postulated as

$$\gamma^* = \frac{u^*}{u'} = \left(\frac{3C_{D2}}{4C_{D1}^2}\right)^{1/4} \left(\frac{\nu\tilde{\epsilon}}{\tilde{k}^2}\right)^{1/4} \tag{2.16}$$

The mass exchange between the fine structures and the surroundings, divided by the mass of the fine structures, is defined as

$$\dot{m}^* = 2\frac{u^*}{L^*} = \left(\frac{3}{C_{D2}}\right)^{1/2} \left(\frac{\tilde{\epsilon}}{\nu}\right)^{1/2} \tag{2.17}$$

The mass exchange between the fine structures and the surroundings, divided by the total mass, is calculated according to

$$\dot{m} = \gamma^* \dot{m}^* \tag{2.18}$$

The mass-averaged mean reaction rate for the s specie is given as

$$-\bar{\omega}_s = \frac{\bar{\rho}\dot{m}\chi}{1-\gamma^*\chi}\left(\tilde{Y}_s - Y_s^*\right),\ s = 1, \ldots, N_s \tag{2.19}$$

and the relationship between the mass-averaged mean state, fine-structure state and surrounding state is expressed as

$$\tilde{\Psi} = \gamma^*\chi\Psi^* + (1-\gamma^*\chi)\Psi^\circ \tag{2.20}$$

Here, χ is the reacting fraction of the fine structures, which can depend on the probability of co-existence of the reactants, the degree of heating and reaction limitations. In the present study, $\chi = 1$, as suggested by Gran and Magnussen [27]. The mean mass fraction $\tilde{Y}_s$ for species s is calculated from solving the species mass transport equation for each individual species. The fine-structure mass fraction Y_s^* is computed through the detailed chemistry approach.

2.2.3 EDC detailed chemistry approach

Finite-rate chemical kinetics are taken into account by treating the fine structures as constant pressure and adiabatic homogeneous reactors. Thus, the fine structures mass fractions values Y_s^* can be calculated by solving a system of ordinary differential equations (ODE) describing a Perfectly Stirred Reactor (PSR) [27],

$$\frac{dY_s^*}{dt} = \frac{\omega_s^*}{\rho^*} + \frac{1}{\tau^*}\left(Y_s^\circ - Y_s^*\right),\ s = 1, \ldots, N_s \tag{2.21}$$

The reaction rate ω_s^* is evaluated from a chemical kinetics mechanism, and Y_s° is the mass fraction of the inflow stream to the reactor. In the present study, it is assumed adiabatic and isobaric PSRs. Further, it is assumed that the PSRs are at steady state [27], meaning that the steady-state solution of Eq.2.21 is achieved by integrating it in time to steady state.

It is worth noticing that the residence or mixing time scale τ^* is evaluated using the molecular viscosity and the dissipation rate

$$\tau^* = \frac{1}{\dot{m}^*} \tag{2.22}$$

The applied chemical kinetic mechanisms are provided separately in the test case description of the Sandia flame D, the Sandia flame CHNa and the Sydney flame HM1E.

2.3 LES for turbulent combustion modeling

2.3.1 Governing equations

In present LES, the relevant flow variables are filtered in the physical space (assuming weighted averaging in a given volume). The filtered variable $\bar{f}(x)$ denotes by overbar is defined as

$$\bar{f}(x) = \int_V G(x - x^*) f(x^*) \, dx^*, \tag{2.23}$$

where V is the volume of the LES filter and G is a filter kernel. In the present study a top-hat (or sometimes called 'box') filter [26], where the filter operations in each x_j direction are identical, is employed. The filter width Δ is defined as $\Delta = (\Delta_x \Delta_y \Delta_z)^{1/3}$ assuming the filter kernel as

$$G(x) = G(x_1, x_2, x_3) \begin{cases} 1/\Delta & |x_i| < \Delta_i/2, \quad i = 1, 2, 3 \\ 0 & \text{otherwise} \end{cases} \tag{2.24}$$

where (x_1, x_2, x_3) are the spatial coordinates of the location x.

A mass-weighted, Favre filtering is introduced as:

$$\bar{\rho}\tilde{f}(x) = \int_V \rho G(x - x^*) f(x^*) \, dx^*. \tag{2.25}$$

The filtered Favre-averaged balance equations of mass, momentum, energy and species are:

$$\frac{\partial \bar{\rho}}{\partial t} + \frac{\partial \bar{\rho}\tilde{u}_j}{\partial x_j} = 0 \tag{2.26}$$

$$\frac{\partial \bar{\rho}\tilde{u}_i}{\partial t} + \frac{\partial \bar{\rho}\tilde{u}_i\tilde{u}_j}{\partial x_j} = -\frac{\partial \bar{p}}{\partial x_i} + \frac{\partial \tilde{\tau}_{ij}}{\partial x_j} - \frac{\partial}{\partial x_j}\left(\bar{\rho}\left(\widetilde{u_i u_j} - \tilde{u}_i\tilde{u}_j\right)\right) \tag{2.27}$$

$$\frac{\partial \bar{\rho}\tilde{Y}_s}{\partial t} + \frac{\partial \bar{\rho}\tilde{Y}_s\tilde{u}_j}{\partial x_j} = \frac{\partial}{\partial x_j}\left(\bar{\rho}D_s\frac{\partial \tilde{Y}_s}{\partial x_j}\right) - \frac{\partial}{\partial x_j}\left(\bar{\rho}\left(\widetilde{u_j Y_s} - \tilde{u}_j\tilde{Y}_s\right)\right) + \bar{\omega}_s \tag{2.28}$$

$$\frac{\partial \bar{\rho}\tilde{h}}{\partial t} + \frac{\partial \bar{\rho}\tilde{h}\tilde{u}_j}{\partial x_j} = \frac{\partial}{\partial x_j}\left(\overline{\xi_j^h} + \overline{u_i\tau_{ij}}\right) - \frac{\partial}{\partial x_j}\left(\bar{\rho}\left(\widetilde{u_j h} - \tilde{u}_j\tilde{h}\right)\right) + \frac{\partial \bar{p}}{\partial t} - \frac{\partial}{\partial x_j}\left(\bar{q}_r\right) + \bar{S}_{hc} \tag{2.29}$$

where $\bar{f}$ and $\tilde{f}$ denote Favre-filtered quantities instead of ensemble means. Here, ρ is the density, $\mathbf{u}$ is the velocity, p is the pressure, $h = \sum_s \tilde{Y}_s \int C_{p,s}\, d\tilde{T}$ represents the enthalpy, T is the temperature, Y_s is the species mass fraction, D_s is the mass diffusion coefficient for species s in a mixture ($D_s = D = 2.88 \times 10^{-5}$ m^2/s), ω_s is the species reaction rate, q_r is the radiative heat loss, S_{hc} represents the source term due to combustion and $\overline{\xi_j^h}$ is the filtered laminar diffusion flux and $\bar{S}_{hc}$ is modeled according to Eq. 2.7.

The subgrid flow physics is concealed in the subgrid stress tensor $\mathbf{B} = \bar{\rho}\left(\widetilde{u_i u_j} - \tilde{u}_i\tilde{u}_j\right)$ and flux vectors $\mathbf{b}_s = \bar{\rho}\left(\widetilde{u_j Y_s} - \tilde{u}_j\tilde{Y}_s\right)$ and $\mathbf{b}_h = \bar{\rho}\left(\widetilde{u_j h} - \tilde{u}_j\tilde{h}\right)$. The subgrid pressure fluctuations and dissipation terms are neglected. Moreover, the subgrid-scales incompressibility hypothesis [25] is used for derivation of the energy balance equation, assuming low Mach number limit.

It is assumed that the gas mixture behaves as a linear viscous (Newtonian) fluid, which assumes that $\bar{\rho}$, $\bar{p}$ and $\tilde{T}$ are linked by the equation of state $\bar{p} = \bar{\rho}R\tilde{T}$, where R the composition dependent gas constant.

The shear-stress tensor τ_{ij} is given by

$$\tilde{\tau}_{ij} = 2\mu\widetilde{\mathbf{S}}_{ij} - \frac{2}{3}\mu\delta_{ij}\widetilde{\mathbf{S}}_{kk} = 2\mu\widetilde{\mathbf{S}}_D, \tag{2.30}$$

where $\widetilde{\mathbf{S}}_{ij}$ the components of the viscous stress (rate-of-strain) tensor $\widetilde{\mathbf{S}}$ defined as,

$$\widetilde{\mathbf{S}}_{ij} = \frac{1}{2}\left(\frac{\partial \tilde{u}_i}{\partial x_j} + \frac{\partial \tilde{u}_j}{\partial x_i}\right), \tag{2.31}$$

μ the viscosity, δ_{ij} the Kronecker symbol and

$$\widetilde{\mathbf{S}}_D = \frac{1}{2}\left(\frac{\partial \tilde{u}_i}{\partial x_j} + \frac{\partial \tilde{u}_j}{\partial x_i}\right) - \frac{1}{3}\delta_{ij}\frac{\partial \tilde{u}_i}{\partial x_j} \tag{2.32}$$

the deviatoric part of $\mathbf{S}$.

Explicit LES closures can typically be classified as functional or structural models [74], [25]. Functional models are designed based on the turbulence energy cascade from large- to small-scales considered for fully developed turbulent flows. The energy drain for the energy cascade is modeled using the hypothesis of a subgrid viscosity μ_B [20] resulting in

$$\mathbf{B} = \frac{2}{3}\bar{\rho}\delta_{ij}\tilde{k} - 2\mu_B\widetilde{\mathbf{S}}_D. \tag{2.33}$$

To close these models, the one equation eddy viscosity model [91] is utilized for which the subgrid viscosity is given by $\mu_B = c_k\overline{\rho}\sqrt{\tilde{k}}\Delta$, and the subgrid kinetic energy $\tilde{k}$ is estimated by solving a separated modeled transport equation of the form,

$$\frac{\partial\bar{\rho}\tilde{k}}{\partial t} + \frac{\partial\bar{\rho}\tilde{k}\tilde{u}_j}{\partial x_j} = \mathbf{F}_p + \mathbf{F}_d - \mathbf{F}_\epsilon, \tag{2.34}$$

$$\mathbf{F}_p = -\mathbf{B}\cdot\widetilde{\mathbf{S}}, \tag{2.35}$$

$$\mathbf{F}_d = \frac{\partial}{\partial x_j}\left((\mu_B + \mu)\frac{\partial\tilde{k}}{\partial x_j}\right), \tag{2.36}$$

$$\mathbf{F}_\epsilon = c_\epsilon\ \overline{\rho}\ \tilde{k}^{3/2}/\Delta, \tag{2.37}$$

where $\mathbf{F}_p$ is production, $\mathbf{F}_d$ diffusion and $\mathbf{F}_\epsilon$ dissipation terms, respectively, and c_k, c_ϵ are model coefficients. It is worth noticing that both models coefficients can be calculated dynamically using two levels of filtering and scale similarity. However, it was found that the dynamic procedure leads to the numerical instabilities for the combustion LES with the EDC, and static coefficients $c_k = 0.07$ and $c_\epsilon = 1.048$ [74] were used in the present study. For the assumed β-PDF approach both c_k and c_ϵ are computed dynamically.

The subgrid fluxes are modeled according to a simple gradient diffusion approximation

$$\mathbf{b}_s = \frac{\mu_B}{\mathrm{Sc}_{t,s}}\left(\frac{\partial\tilde{Y}_s}{\partial x_j}\right), \tag{2.38}$$

$$\mathbf{b}_h = \frac{\mu_B}{\mathrm{Pr}_t}\left(\frac{\partial\tilde{h}}{\partial x_j}\right), \tag{2.39}$$

where $\mathrm{Sc}_{t,s}$ and Pr_t are turbulence Schmidt and Prandtl numbers, which were set to $\mathrm{Sc}_{t,s} = \mathrm{Pr}_t = 0.7$.

2.3.2 EDC for turbulent combustion

The Eddy Dissipation Concept is based on the energy cascade model and assumes that molecular mixing and chemical reactions occur on the smaller dissipative eddies, which

are close to the Kolmogorov length scales and are termed 'fine structures'. The characteristic length L^* and velocity u^* scales of the fine structures are of the same order of magnitude as Kolmogorov scales and can be expressed as

$$L^* = \frac{2}{3}\left(\frac{3C_{D2}^3}{C_{D1}^2}\right)^{1/4}\left(\frac{\nu^3}{\tilde{\epsilon}}\right)^{1/4} \tag{2.40}$$

$$u^* = \left(\frac{C_{D2}}{3C_{D1}^2}\right)^{1/4}(\nu\tilde{\epsilon})^{1/4} \tag{2.41}$$

where $C_{D1} = 0.134$ and $C_{D2} = 0.5$ [19]. Here, we assume that the full cascade takes place at each numerical cell, and the connection between the fine structure and the larger eddies is achieved through the cascade. Thus, characteristics of the large eddies such as velocity u' can be evaluated using the turbulence model. The turbulence kinetic energy $\tilde{k}$ is found from the the solved transport equation (Eqn. 2.34). The dissipation of the subgrid kinetic energy $\tilde{\epsilon}_{sgs}$ is expressed as

$$\tilde{\epsilon}_{sgs} = c_\epsilon\, \overline{\rho}\, \tilde{k}^{3/2}/\Delta, \tag{2.42}$$

where the model constant $c_\epsilon = 1.048$.

In the model expressed below, different superscripts refer to states inside fine structures (*), surroundings ($\circ$) and filtered values of the computational cell ($\sim$).

The ratio between the mass in the fine structures and the total mass is postulated as

$$\gamma^* = \frac{u^*}{u'} = \left(\frac{3C_{D2}}{4C_{D1}^2}\right)^{1/4}\left(\frac{\nu\tilde{\epsilon}}{\tilde{k}^2}\right)^{1/4} \tag{2.43}$$

The mass exchange between the fine structures and the surroundings, divided by the mass of the fine structures, is defined as

$$\dot{m}^* = 2\frac{u^*}{L^*} = \left(\frac{3}{C_{D2}}\right)^{1/2}\left(\frac{\tilde{\epsilon}}{\nu}\right)^{1/2} \tag{2.44}$$

The mass exchange between the fine structures and the surroundings, divided by the total mass, is calculated according to

$$\dot{m} = \gamma^*\dot{m}^* \tag{2.45}$$

The mass-averaged filtered reaction rate for the s-th specie is given as

$$-\bar{\omega}_s = \frac{\bar{\rho}\dot{m}\chi}{1-\gamma^*\chi}\left(\tilde{Y}_s - Y_s^*\right),\ s = 1, \ldots, N_s \tag{2.46}$$

and the relationship between the mass-averaged mean state, fine-structure state and surrounding state is expressed as

$$\tilde{\Psi} = \gamma^*\chi\Psi^* + (1-\gamma^*\chi)\Psi^\circ \tag{2.47}$$

Here, χ is the reacting fraction of the fine structures, which can depend on probability of co-existence of the reactants, degree of heating and a limiter to the reaction due to lack of reactants. In the present study, $\chi = 1$, as suggested by Gran and Magnussen [27]. The mass fraction $\tilde{Y}_s$ for species s is calculated from solving the species mass transport equation for each individual species. The fine-structure mass fraction Y_s^* is computed through the detailed chemistry approach.

Finite-rate chemical kinetics are taken into account by treating the fine structures as constant pressure and adiabatic homogeneous reactors in the same way as described in Sec. 2.2.3.

2.4 Modeling radiation

The radiation is modeled by the P1-approximation, which is the simplest form of the more generalized P-N method (or spherical harmonics) [12] assuming that a flame is optically thin. The radiative heat loss $\bar{q}_r$ is calculated as

$$-\frac{\partial}{\partial x_j}\bar{q}_r = \alpha_c G - 4e_c\sigma T^4, \tag{2.48}$$

where α_c is the absorption coefficient (m^{-1}), e_c is the emission coefficient (m^{-1}) and σ is the Stefan-Boltzmann constant. The incident radiation G is modeled according to

$$\frac{\partial}{\partial x_j}\left(\Gamma\frac{\partial}{\partial x_j}G\right) - \alpha_c G + 4e_c\sigma T^4 = 0, \tag{2.49}$$

$$\Gamma = \frac{1}{3\left(\alpha_c + \sigma_s\right)}, \tag{2.50}$$

where σ_s is the scattering coefficient ($\sigma_s = 1\ \mathrm{m}^{-1}$), respectively. The absorption coefficient and the emission coefficient are calculated using a weighted-sum-of-gray-gases model (WSGGM) [32] as a function of local concentrations of CO_2 and H_2O, path-length and pressure. The emissivity weighting factors for CO_2 and H_2O are taken from Smith et al. [78].

2.5 Numerical method and its implementation

2.5.1 Core numerical method

The OpenFOAM code [85] was used for the numerical simulations. The new solver was developed based on the finite-volume (FVM) method [26] and the the PISO (pressure implicit with splitting of operators) algorithm [81] for the pressure-velocity coupling, implemented according to Rhie and Chow type interpolation for the cell-centered data

storage structure [36]. The preconditioned (bi-) conjugate gradient method [30] with incomplete-Cholesky preconditioner (ICCG) by Jacobs [37] was used for solving linear systems with a local accuracy of 10^{-7} for all dependent variables at each time step.

The numerical method had second-order accuracy in space and time. The linear-upwind interpolation scheme (sometimes referred to as the 'second-order upwind' scheme [83]), was applied for all convective terms approximation for the URANS formulation. Linear interpolation [83] was used to calculate all other spatial derivatives.

The central-difference scheme (CDS-2, [26]) was applied for all convective-term approximations for the non-reacting LES, while the blended NVD(TVD)/CDS-2 scheme by Jasak [38] was used for the momentum equations for the reacting LES. As is common practice, a total variation diminishing (TVD) scheme [29] was used for the scalars to avoid unphysical overshoots and second law violations [65], [39].

A second-order implicit Euler method (BDF-2, [26]) was used both for URANS/LES to provide time integration together with the dynamic adjustable time stepping technique to guarantee a local Courant number less than 0.4.

The calculation of the species reaction rate $\bar{\omega}_s$ requires the integration of Eq.2.21 for each cell in the domain. For this purpose, the robust RADAU5 algorithm [28] was used [50]. The RADAU5 algorithm was designed for the solving stiff ODE systems and applied a 5th order accurate implicit Runge-Kutta method based on the Radau quadrature formula. The relative tolerance, absolute tolerance and maximum number of iterations to meet the target accuracy were set to 5×10^{-5}, 1×10^{-5} and 10^7, respectively.

2.5.2 High performance computing

Parallel scalability analysis is required to understand and optimize the existing software for high-performance computing (HPC). OpenFOAM is the massive parallel open source C++ classes library based on message-passing interface (MPI). For the assessment of the parallel performance, such parameters as strong scalability, weak scalability and system efficiency were used with their standard definition according to Wilkinson and Allen [87].

For the assessment of the parallel performance, such parameter as strong scalability $S(p)$ (where p is the number of cores) was used with its standard definition according to Wilkinson and Allen [87]. $S(p)$ is defined as the ratio of a execution time using a single core system (T_s) to an execution time using a multiprocessor system with p cores (T_p): $S(p) = T_s/T_p$.

Preliminary results shown the modest parallel efficiency of $\sim 40\%$ and were obtained on the STALLO HPC facility (`www.notur.no`) installed at the end of 2007. However, the most of the present calculations were carried out using the VILJE HPC facility (`www.notur.no`) which was installed in 2012.

These results for non-reacting flow simulations are presented in Fig. 2.1. Scaling was

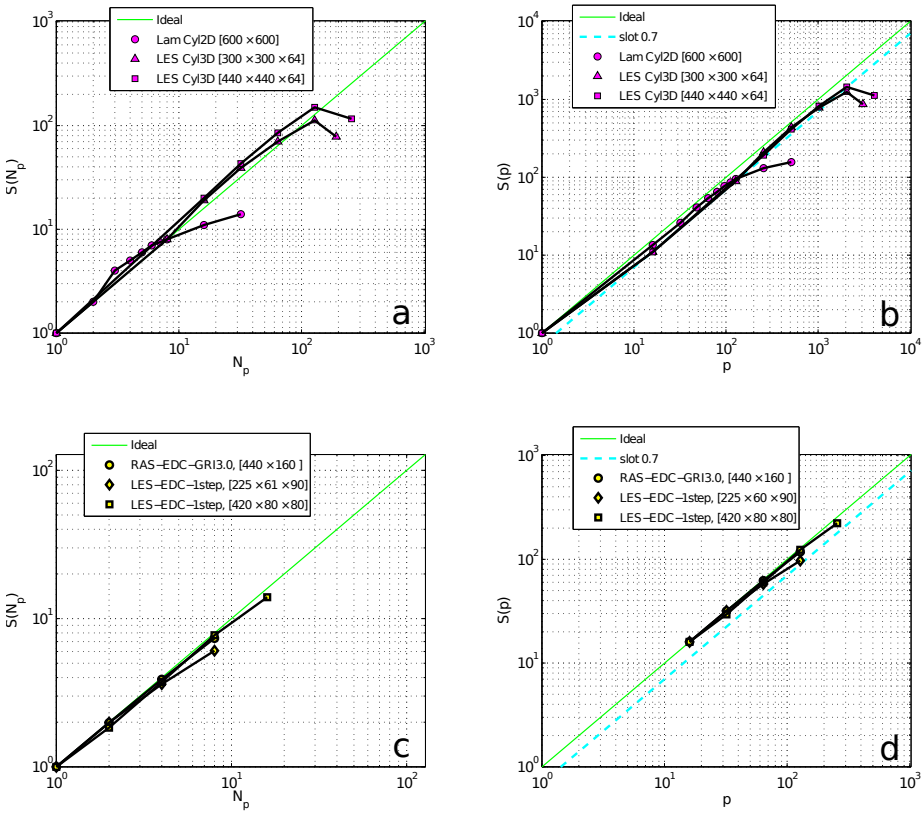

Figure 2.1: OpenFOAM parallel performance on the VILJE HPC facility. Strong scalability studies for the 2D and 3D non-reacting flows over a circular cylinder and for the 2D and 3D reacting simulations of the Sandia flame D as function of number of nodes (a,c) and total number of cores (b,d), respectively. The grid size is shown in brackets for each case. One node has 16 cores.

done both for one node consisting of 16 cores (Fig. 2.1a) and one core (Fig. 2.1b). Three cases were considered, including one $2D$ case for the laminar compressible flow over a circular cylinder (Re $= 140$, M $= 0.2$) on the O-type mesh size of 600×600 and two compressible LES cases for the flow over a circular cylinder (Re $= 20 \times 10^3$, M $= 0.2$) on the O-type grids size of $300 \times 300 \times 64$ and $440 \times 440 \times 64$, respectively. In general, OpenFOAM demonstrated good strong scalability with the average efficiency of $\sim 70\%$ comparable with state-of-the-art commercial CFD codes like ANSYS FLUENT. It worth noticing that some optimization (etc. using of OEM SGI MPI libraries and its further tunning) of the OpenFOAM code was carried out to improve the strong scaling from $\sim 40\%$ on STALLO up to $\sim 70\%$ on VILJE.

Due to strong non-linear coupling between turbulence, chemistry and thermal radiation

parallel implementation of the numerical methods for such flows simulations are quite challenging. Some results for reacting flow simulations are presented in Fig. 2.1c,d. However, it can be seen clearly that the implemented method demonstrated good parallel scalability with the same average efficiency of $\sim 70\%$ for the reacting cases as well.

2.6 Mathematical tools for spectral analysis

All spectral data processing was performed using a commercial software package (MATLAB R2012a, The MathWorks Inc., Natick, MA, 2012). Since an adaptive-time stepping technique was used for the time integration (due to varying time steps), the collected time series were not evenly sampled. To obtain the one-dimensional energy spectra, the Welch periodogram technique (WPD hereafter) [84] was used for the two signal sequences with a number of time steps of 6×10^5 and with an overlapping factor of 0.7. The one-dimensional energy spectra calculated from these time series were then averaged in the span-wise direction to increase the statistical sample [42]. The frequency was nondimensionalized by the Strouhal shedding frequency (f_{vs}).

Like the Fourier transform, the continuous wavelet transform (CWT hereafter) uses inner products to measure the similarity between a signal ($f(t)$) and an analyzing function (wavelet $\psi(t)$). Comparing $f(t)$ to $\psi(t)$ at various scales and positions leads to the two-dimensional representation of $f(t)$. For a scale parameter, $a > 0$, and position, b, the CWT coefficients $C(a,b)$ are:

$$C(a,b;f(t),\psi(t)) = \int_{-\infty}^{\infty} f(t) \frac{1}{\sqrt{a}} \psi^* \left(\frac{t-b}{a} \right) dt, \tag{2.51}$$

where $*$ denotes the complex conjugate. Expressing the CWT as an inverse Fourier transform enables the use of the computationally efficient fast Fourier transform (FFT) algorithm to reduce the cost of computing convolutions. Thus, rewriting of Eq. 2.51 as an inverse Fourier transform gives:

$$C(a,b;f(t),\psi(t)) = \frac{1}{2\pi} \int_{-\infty}^{\infty} \hat{f}(\omega) \sqrt{a} \left(\hat{\psi}(a\omega) \right)^* \exp(i\omega b) \, d\omega, \tag{2.52}$$

where $\hat{f}(\omega)$ and $\hat{\psi}(a\omega)$ are the Fourier transforms of the signal and wavelet, respectively. In this study we use a continuous wavelet transform based on the FFT algorithm. One of the most popular continuous wavelets is the Morlet wavelet, which allows to determine efficiently the energy containing structures (coherent structures) in the flow signal [22],[8]. The analytic Morlet wavelet is defined in the Fourier domain by

$$\hat{\psi}(a\omega) = \pi^{-1/4} \exp\left(\frac{(a\omega - \omega_0)^2}{2} \right) U(a\omega), \tag{2.53}$$

where $U(a\omega)$ is the Heaviside step function [79]. The default value of ω_0 was 6. The relation between the pseudo-frequencies and corresponding scales a for this wavelet was:

$$f = \frac{4\pi a}{\omega_0 + \sqrt{2 + \omega_0^2}}. \tag{2.54}$$

Finally, a scalogram $\mathrm{E}(a, b)$ by definition represents the percentage of energy for each coefficient or, in other words, the contribution to the total energy at a specific a scale and b location: $\mathrm{E}(a, b) = |C(a, b; f(t), \psi(t))|^2$. The dominant structures are then characterized by large local $\mathrm{E}(a, b)$ values [2].

Chapter 3

Present contribution

The main contribution of this work is six papers which are published, submitted and to be submitted to peer-review journals. In this section, a brief summary of each paper is given.

3.1 Paper A

Modeling of turbulent separated flows using OpenFOAM
Co-authors: Ivar S. Ertesvåg and Kjell Erik Rian

In this paper turbulent separated bluff-body flows were numerically analyzed using the state-of-the-art OpenFOAM and ANSYS FLUENT technologies, based on the conventional compressible URANS approach. A low-Reynolds-number k-ϵ model by Launder and Sharma [43] and a Realizable k-ϵ model of Shih [76] with an enhanced wall treatment approach [11] were used for the closure problem. Several popular in fluid dynamics test problems such as laminar and turbulent flows over a circular cylinder and turbulent fully developed flows over a triangular cylinder in a channel were numerically replicated with the goal of validation of the selected numerical methods. The detailed, face-to-face comparison between OpenFOAM, FLUENT and experimental data was discussed. Parallel performance of the OpenFOAM toolbox in the terms of a strong and weak scalability was assessed up to 1024 cores at the STALLO HPC facility (`www.notur.no`) and shown the modest parallel efficiency of $\sim 40\%$. In general, the present results demonstrated minimum deviations between OpenFOAM and FLUENT and agreed fairly well with the experimental data and other numerical solutions.

3.2 Paper B

Paper B - Numerical simulation of turbulent flames using the Eddy Dissipation Concept with detailed chemistry
Co-authors: Ivar S. Ertesvåg and Kjell Erik Rian

This paper presents numerical simulations of the Sandia flame CHNa and Sydney bluff-body stabilized flame HM1E.

The Eddy Dissipation Concept with the detailed chemistry approach and the standard k-ϵ turbulence model (with the standard constants) were applied to simulate the Sandia flame CHNa and the Sydney flame HM1E. The finite-rate chemistry effects were described by the FFR and the GRI3.0 mechanisms. The robust implicit Runge-Kutta method (RADAU5) was used for integrating stiff ordinary-differential equations to compute the reaction rates. The radiation heat transfer was treated with the simple P-1 model. Statistically stationary results were obtained and compared in detail with the available experimental data. In general, there was good agreement between the present simulations and measurements for both flames. It is believed that one of the main reasons for the observed discrepancies between the EDC-based predictions and experimental data for the Sandia flame CHNa was the round-jet anomaly of the k-ϵ turbulence model. The Sydney flame HM1E was calculated with the k-ω SST turbulence model as well. However, the predicted results did not reveal any significant deviations between the standard k-ϵ and the SST model which could be explained by the SST model implementation in OpenFOAM.

The steady laminar flamelet model was applied to investigate the influence of the turbulence-chemistry interaction. For this purpose the commercial code ANSYS FLUENT was utilized. It worth noticing that the same grids were used and the quite similar numerical methods, boundary conditions and the sub-models for the turbulence and radiative heat transfer were chosen. The finite-rate chemistry effects were taken into account using the FFR and the GRI3.0 mechanisms. It was found that the most accurate SLF-based predictions for the Sandia flame CHNa was obtained with the modified constant $C_{\epsilon 1} = 1.52$. The present results obtained with the SLF-based approach and the default value of the PDF turbulence Schmidt number $\mathrm{Sc}_t = 0.85$ were found to be less accurate than the EDC-based for the Sydney flame HM1E due to the lack of the turbulence mixing. The calculation with the modified Schmidt number $\mathrm{Sc}_t = 0.4$ showed some improvement in the prediction of the composition and temperature but was not sufficient to match the experimental data well.

Overall, the present results give a good indication on the adequacy and accuracy of the implemented solver in the OpenFOAM toolbox and its readiness for further combustion application development.

3.3 Paper C

Paper C - Large-eddy simulation of the flow over a circular cylinder at Reynolds number 3900 using the OpenFOAM toolbox
Co-authors: Ivar S. Ertesvåg and Kjell Erik Rian

The objective of this paper was an extensive investigation of the numerical aspects influencing the quality of LES solutions, implemented in the OpenFOAM toolbox. With this purpose, the flow past a circular cylinder at a sub-critical Reynolds number of 3900 and Mach number of 0.2 was simulated using an LES technique with the dynamic k-equation SGS model [91]. To check SGS influence, an additional run was carried out with the conventional Smagorinsky model [77]. Particular attention was put on the statistical convergence. To achieve fully converged data in the present LES, the statistics were collected for a time interval of about 150 vortex shedding periods. Predicted integral flow parameters, local first-order statistics and one-dimensional energy spectra were analyzed in detail and compared with existing experimental data [53],[64].

Analysis of the available experimental data, DNS data and LES data revealed the existence of the flow bifurcation (the U–shaped and V–shaped states) for this benchmark case. Recently, Wissink and Rodi [88] performed a DNS study using extremely-high mesh resolution for the flow over a circular cylinder at Re $= 3300$ and concluded that a U–shaped solution was more likely. This finding was confirmed partially by the present results: the solution based on the dynamic k-equation SGS model converged to the U–shaped state, while the conventional Smagorinsky model converged to the V–shaped state. However, both flow states have been identified experimentally by Lourenco and Shih [53] and Parnaudeau et al. [64].

3.4 Paper D

Paper D - Large-eddy simulation of the flow over a circular cylinder at Reynolds number 2×10^4
Co-authors: Ivar S. Ertesvåg and Kjell Erik Rian

This paper presents a further detailed investigation of the numerical aspects influencing the quality of LES solutions, implemented in the OpenFOAM toolbox. For this purpose, the flow past a circular cylinder at an intermediate sub-critical Reynolds number of 2×10^4 was simulated using both incompressible and compressible setups. In general, there were good agreement between the present incompressible flow results, the available experimental data and the LES results by Wornom et al. [89]. Calculated integral flow parameters, local first-order statistics and one-dimensional energy spectra agreed fairly well with the experimental data as well as with other LES studies ([75], [89]). All flow

features such as thin laminar boundary layers, unsteady separation, wake dynamics and shear-layer instabilities were captured as well.

Provided computer visualization of the cylinder's near wake revealed clearly the separation of the shear layers and their intermittent nature. Application of continuous wavelet analysis allowed to precisely quantify the Kelvin-Helmholtz instability of the separated shear layer (KH) [68] and identify the dependency between Reynolds number and the ratio between an asymmetric vortex shedding (the Bénard / von Kármán instability [68]) and the KH instability as a power law with $n = 0.47$. This finding is consistent with available experimental ([6], [41], [63]) and numerical ([15], [40]) data. However, there is another set of measurements [70] available in the literature indicating the higher value of $n = 0.67$.

Another important conclusion following from the present results is the solution inaccuracies revealed by the compressible flow algorithm at a low-Mach number (M = 0.2). The present results showed that for this particular case the compressible flow setup produced spurious oscillations in the vicinity of the cylinder, where the grid density is extremely high. Here, the filtered CDS-2 scheme, the blended NVD(TVD)/CDS-2 scheme by Jasak [38] and the LUST scheme by Weller [85] were tested to eliminate these numerical waves. It was shown that the filtered CDS-2 scheme seemed to have only minor impact on the oscillations. The Gamma scheme damped the spurious wave significantly but not sufficiently, meanwhile the LUST scheme damped all oscillations completely. However, the provided spectral analysis and the visualization of the coherent structures of the flow revealed that these schemes had a too dissipative nature (compared to the pure CDS-2 scheme) witch further indicate their impracticability for the high-fidelity large-eddy simulation.

3.5 Paper E

Paper E - Towards simulation of far-field aerodynamic sound from a circular cylinder using OpenFOAM
Co-authors: Ivar S. Ertesvåg and Kjell Erik Rian

The objective of this paper was an investigation of the OpenFOAM capabilities for the Aeolian tones aeroacoustic predictions and the different numerical aspects influencing the quality of solutions. With this purpose, two test cases were considered: the laminar flow past a circular cylinder at the Reynolds number of 140 and Mach number of 0.2 and the flow past a circular cylinder at the sub-critical Reynolds number of 2.2×10^4 and Mach number of 0.06. In both cases, the sound generated by a circular cylinder was investigated by direct solution of the unsteady compressible Navier-Stokes equations. The second case was simulated using an LES technique with the conventional Smagorinsky SGS model. In general, the present results agreed fairly well with the experimental data for both aerodynamic and acoustic fields. Several interesting findings can be outlined:

- In both cases, the generated sound had a dipole nature. The influence of the turbulent wake at the Reynolds number Re $= 2.2 \times 10^4$ on the tonal waves was non-significant and had the local near-field nature; The results of the numerical simulation at Re $= 2.2 \times 10^4$ indicated that most aerodynamic quantities were in good agreement with the existing experimental data. It is worth noticing, that both types of the instabilities (an asymmetric vortex shedding or the Bénard / von Kármán instability and the Kelvin-Helmholtz instability of the separated shear layer [68]) were captured well and quantified accurately using Fourier and wavelet continuous analysis. Finally, observed small discrepancies can be explained by the lack of resolution;

- The present results confirmed that the Doppler effect played the important role. The maximum propagation angle of the pressure waves could be approximated well by the simple relationship $\theta_p = \cos^{-1} \mathrm{M}$ (where M is a Mach number) derived by Inoue and Hatakeyama [34] which was consistent with the present results and the experiment by Casalino and Jacob [9];

- The sound pressure waves were generated primarily by the vortex shedding and had a tendency to decay in proportion to $1/\sqrt{r}$ for both simulations. This finding was was consistent with the theoretical prediction of Landau and Lifshitz [45]. The scaling law for the fluctuating pressure at Re $= 140$ could be approximated well by the simple relationship $p' \approx \mathrm{M}^{2.5}/\sqrt{r}$ estimated by Inoue and Hatakeyama [34] based on Curl's acoustic analogy for low Mach numbers. However, the present results did not confirm this scaling for the higher Reynolds number Re $= 2.2 \times 10^4$;

- We did not apply any extra filtering in the present simulations. However, in the vicinity of the cylinder, where the grid was extremely dense, spurious numerical waves were generated affecting the near-field region of the flow. However, based on the previous calculations we can concluded that these artificial waves had minor impact on the main integral (mean) flow parameters and far-field sound, but influenced on the local near-field quantities such as the drag and lift forces and the root mean square of the pressure coefficient.

3.6 Paper F

Paper F - Numerical simulations of the Sandia Flame D using the Eddy-Dissipation concept
Co-authors: Ivar S. Ertesvåg and Kjell Erik Rian

In this paper the Eddy Dissipation Concept was extended for the compressible large-eddy simulation technique. The Eddy Dissipation Concept, which has been successfully used in RANS calculations of turbulent flames has been formulated as a combustion model for the large-eddy simulations and implemented in the OpenFOAM toolbox. The model

has been applied both for RAS and LES of the turbulent methane/air combustion for the Sandia flame D. The assumed β-PDF approach was used as well to check the influence of modeling of the turbulence-chemistry interaction. The EDC-based and the β-PDF-based results were compared to the experimental data. It is important, that the present results were obtained without any adjustment or calibration of the model constants and agreement was quite reasonable for all quantities for both RAS and LES predictions. The remaining differences have been discussed. It is believed that one of the main reasons for the observed discrepancies between the RAS predictions and experimental data was the round-jet anomaly of the standard k-ϵ turbulence model. The lack of the grid resolution and the insufficient inlet boundary conditions can be considered as the main limitations for the present LES.

Chapter 4

Concluding remarks

Conclusions are given in each separate paper. Here some general conclusions and critical remarks are drawn.

The core numerical method was based on the open source toolbox OpenFOAM [85], which is very popular today in industrial engineering as well as in academic research. Nevertheless, in spite of many attractive features, the OpenFOAM toolbox has some disadvantages as well. The absence of the high quality academic documentation and references is the most critical due to several reasons. First, an excessive validation and verification effort is required to test an implemented numerical method. Second, high quality academic documentation is required as well in any scientific research. Thus, one of the additional goals of the present study was to deliver high quality academic documentation. It is believed that the provided results and discussion will be useful to the community and could be referenced as further validation, documentation and development of the OpenFOAM capabilities.

The large-eddy simulation of turbulent combustion may be considered as one of grand challenge problems [87] and requires an intensive usage of high performance computing facilities. Moreover, the turbulent combustion modeling belongs to the multi-physics and multi-scales science with strong nonlinear coupling between chemistry, turbulence and radiation. The high parallel scalability of the numerical method is required to provide efficient simulations. Most of the present results were obtained using the VILJE HPC facility (`www.notur.no`), where the implemented numerical method demonstrated a good strong scalability for both non-reacting and reacting flows ($\approx 70\%$), which is comparable with the state-of-the-art commercial CFD codes like ANSYS FLUENT.

The compressible URANS with the Eddy Dissipation Concept [56], [57], [27], [19], [50] was applied to simulate the Sandia flame CHNa [4], the Sydney flame HM1E [14] and Sandia flame D [3]. In general, there was good agreement between present simulations and measurements for all flames. Here, the standard k-ϵ model [44] was used to model the turbulent flow and it would be worthwhile to investigate the performance of other turbulence models (etc., Scale-adaptive simulation or Detached-eddy simulation) in future

work. The detailed chemical kinetics mechanisms (FFR [24], GRI3.0 [7]) were applied to take into account the finite-rate chemistry effects. It is important, that the results were obtained without any adjustment or calibration of the model constants and agreement was very reasonable. It is believed that one of the main reasons for the observed discrepancies between the predictions and experimental data is the round-jet anomaly of the standard k-ϵ turbulence model [67],[61]. Another reasons may be related with the point that k-ϵ model could not capture some effects associated with the influence of heat release on the turbulence [47], [51].

The non-reacting LES was validated against the flows over a circular cylinder at Re $=$ 3900 and Re $=$ 20000. High resolution grids were used for the both simulations which allowed to investigate and revealed some new flow features like the frequencies of the shear-layer instability. Another important conclusion following from these results is the solution inaccuracies revealed by the compressible flow algorithm at a low-Mach number (M $=$ 0.2). For this particular case the compressible flow setup produced spurious oscillations in the vicinity of the cylinder, where the grid density is extremely high. Here, the filtered CDS-2 scheme, the blended NVD(TVD)/CDS-2 scheme by Jasak [38] and the LUST scheme by Weller [86] were tested to eliminate these numerical waves. It was shown that the filtered CDS-2 scheme seemed to have only minor impact on the oscillations. The Gamma scheme damped the spurious wave significantly but not sufficiently, meanwhile the LUST scheme damped all oscillations completely.

The Eddy Dissipation Concept has been formulated as a combustion model for the compressible large-eddy simulations and applied for the Sandia flame D [3]. The results were compared with experimental data. In general, agreement was very reasonable for all quantities. It is believed, that the remaining difference related with the lack of the grid resolution and the insufficient turbulence inlet boundary conditions can be considered as the main limitations for the present LES and should be explored in more detail in future work.

The test flames (Sandia flame D, Sandia flame CHNa and Sydney HM1E) were computed with the EDC combustion model as well as the assumed β-PDF approach and the Steady Laminar Flamelet (SLF) model. However, it is interesting to compare results obtained by the EDC with other groups of advanced combustion models based on the conditional moment closure (CMC) and the PDF transport equation. The CMC group of models was not available during the present study. The second group, based on the PDF transport equation is available in the commercial code ANSYS FLUENT. However, the author have faced with some numerical/convergence difficulties applying this model for the selected test cases (results are excluded from the thesis). Besides, the PDF transport model is very computationally expensive due to accounting the finite-rate chemical kinetics as well. Of course, it will be interesting to investigate it in more detail in future work.

It is worth to noticing that the present computed results based on the EDC combustion model (both for URANS and LES) were obtained without any model constant adjustments. The Eddy Dissipation Concept was designed for the fully-developed turbulent flows. It is assumed that the full cascade takes place at each numerical cell, and the con-

nection between the fine structure and the larger eddies is achieved through the cascade. The EDC model constants $C_{D1} = 0.134$ and $C_{D2} = 0.5$ were proposed based on these assumptions and it is recommended to use them without any adjustments. Further 'playing' with constants does not lead to any significant influence in RANS/URANS predictions ([58] and private communication with Prof. Dirk Roekaerts). The combustion LES was performed with these (default) EDC constants as well. The further investigation of the influence of the constants for LES was not conducted due to time limitation.

The results obtained for the Sydney flame HM1E by the SLF model revealed significant dependence on the PDF turbulence Schmidt number. It was found that strong discrepancies between the measured data and the results by the SLF model for the Sydney flame HM1E are strongly related with the lack of the turbulence mixing due to the fixed PDF Schmidt number. Within, another run with the modified PDF Schmidt number $\mathrm{Sc}_t = 0.4$ (instead of the default value $\mathrm{Sc}_t = 0.85$) was performed which indicated that the influence on the flow field was minor, while the composition was changed significantly but still not sufficient to match the experimental temperature.

The influence of the constants in the standard k-ϵ model for the EDC-based URANS calculations was not assessed. However, it was found that for the PDF-based URANS results for the jet flames, the best results were achieved with the modified constant $C_{\epsilon 1} = 1.52$ which is lower than the convenient recommended value $C_{\epsilon 1} = 1.6$ [67],[61]. The k equation subgrid scale model [91] was tested and used for the large-eddy simulation. The EDC-based LES was carried out using static model constants $c_k = 0.07$ and $c_\epsilon = 1.048$ recommended by Sagaut [74]. It was found that the present EDC-based LES has become numerically unstable while using the dynamic procedure. So, it will be interesting to investigate the influence of c_k and c_ϵ on the solution in future work as well as understand the reasons of numerical instabilities. One of the possible explanation for such instabilities probably may be in the not correct behavior of the subgrid dissipation near the wall [1], [33]. The PDF-based LES was conducted using the dynamic k-equation model.

Another important aspect of combustion modeling is the radiative heat transfer. In the present study it was treated in a simplest way using the P-1 approximation [12], assuming that a flame is optically thin. Sometimes, the optically thin radiation submodel could not accurately predict the radiant fraction for partially premixed CH_4 /air jet flames [23]. Thus, it will be interesting in future work to investigate these flames with more sophisticated radiation submodel (like a Discrete Ordinate (DO) model [69]). It is worth noticing that unphysical results for temperature were obtained using the DO model at the center axis while applying it for axi-symmetrical test problems in the present study. These results were confirmed for both OpenFOAM and ANSYS FLUENT. Thus, the full $3D$ simulations are required in order to get accurate predictions with the DO model.

Furthermore, the finite-rate chemical kinetics were taken into account by treating the fine structures as constant pressure and adiabatic homogeneous reactors calculated using the Perfectly Stirred Reactor model [27]. Here the effect of radiation losses in the PSRs was neglected and more accurate formulation should be formulated and investigated in future work.

Further interesting aspect related to PSRs is the solution of stiff systems of ordinary differential equations (ODEs) describing chemical kinetics. The implicit method of Runge-Kutta of 5th-order of accuracy (RADAU5) was used in the present study. This heavy-duty method is applicable for both usual and stiff systems of ODEs, but is quite computationally expensive. Thus, it will be interesting to compare RADAU5 with other methods (especially with lower-order methods, for example, based on backward differentiation formula or Rosenbrock formula) with respect both to the solution accuracy and computational efficiency in future work.

Finally, the effect of heat release on the turbulent flow (both for URANS and LES) was not investigated in the present study and should be taken into account in future work.

Overall, the present results (together with previously obtained results) give a good indication on the adequacy and accuracy of the implemented solver and its readiness for further combustion application development.

Bibliography

[1] Abe, K., An investigation of SGS stress anisotropy modeling in complex turbulent flow fields, Flow, Turbul. Combust., 92, 503-525 (2014)

[2] Addison P.S., Murray, K.B., Watson, J.N., Wavelet transform analysis of open channel wake flows, J. Eng. Mech., 127, 58-70 (2001)

[3] Barlow, R.S., Frank, J.H., Effects of turbulence on species mass fractions in methane/air jet flames, Proc. Combust. Inst., 27, 1087–1095 (1998)

[4] Barlow, R.S., Fiechtner, G.J., Carter, C.D., Chen, J.-Y., Experiments on the Scalar Structure of Turbulent CO/H2/N2 Jet Flames, J. Combust. Flame, 120, 549-569 (2000)

[5] Beaudan, P., Moin, P., Numerical experiments on the flow past a circular cylinder at sub- critical Reynolds number. Technical Report TF-62, CTR Annual Research Briefs, NASA Ames/Stanford University (1994)

[6] Bloor, M.S., The transition to turbulence in the wake of a circular cylinder, J. Fluid Mech., 19, 290–304 (1964)

[7] Bowman, C.T., Hanson, R.K., Davidson, D.F., Gardiner, W.C., Lissianski, V., Smith, G.P., Golden, D.M., Frenklach, M., Goldenberg, M.: GRI-Mech (2008). http://www.me.berkeley. edu/gri-mech/. Accessed February 2013

[8] Brun, C., Aubrun, S., Goossens, T., Ravier, Ph., Coherent structures and their frequency signature in the separated shear layer on the sides of a square cylinder, J. Flow Turbul. Combust., 81, 97-114 (2008)

[9] Casalino, D., Jacob, M., Prediction of aerodynamic sound from circular rods via spanwise statistical modelling, J. Sound Vibr., 262, 815-844 (2003)

[10] Chase, M., NIST-JANAF Thermochemical tables, 4th Ed., J. Phys. Chem. Ref. Data, Monographs and Supplements, 9 (1998)

[11] Chen, H., Patel, V., Near-wall turbulence models for complex flows including separation, AIAA J., 26, 641-648 (1988)

[12] Cheng, P., Dynamics of a radiating gas with application to flow over a wavy wall, AIAA J., 4, 238-245 (1966)

[13] Cuoci, A., Frassoldati A., Buzzi Ferraris, G., Faravelli, T., Ranzi, E., The ignition, combustion and flame structure of carbon monoxide/hydrogen mixtures. Note 2: Fluid dynamics and kinetic aspects of syngas combustion, Int. J. Hydrogen Energy, 32, 3486-3500 (2007)

[14] Dally, B.B., Masri, A.R., Barlow, R.S., Fiechtner, G.J., Instantaneous and mean compositional structure of bluff- body stabilised nonpremixed flames, J. Combust. Flame, 114, 119-148 (1998)

[15] Dong, S., Karniadakis, G.E., Ekmekci, A., Rockwell, D., A combined direct numerical simulation particle image velocimetry study of the turbulent air wake, J. Fluid Mech. 569, 185–207 (2006)

[16] Dunn, M.J., Masri, A.R., Bilger, R.W., A new piloted premixed jet burner to study strong finite-rate chemistry effects, J. Combust. Flame, 151, 46–60 (2007)

[17] Dunn, M.J., Masri, A.R., Bilger, R.W., Barlow, R.S., Wang, G.H., The compositional structure of highly turbulent piloted premixed flames issuing into a hot coflow, Proc. Combust. Inst., 32, 1779–1786 (2009)

[18] Echekki T., Mastorakos E., Turbulent Combustion Modeling: Advances, New Trends and Perspectives. Springer (2011)

[19] Ertesvåg, I.S., Magnussen, B.F., The eddy dissipation turbulence energy cascade model, J. Combust. Sci. Technol., 159, 213–235 (2000)

[20] Feymark, A., Alin, N., Bensow, R., Fureby, C., Numerical simulation of an oscillating cylinder using large eddy simulation and implicit large eddy simulation, J. Fluids Eng., 134, 031205 (2012)

[21] Fox, R.O., Computational models for turbulent reacting flows. Cambridge University Press. Cambridge (2003)

[22] Farge, M., Wavelet transforms and their application to turbulence, Ann. Rev. Fluid. Mech., 24, 395-457 (1992)

[23] Frank, J.H., Barlow, R.S., Lundquist, C., Radiation and nitric oxide formation in turbulent non-premixed jet flames, Proc. Combust. Inst., 28, 447–454 (2000)

[24] Frassoldati, A., Faravelli, T., Ranzi, E., The ignition, combustion and flame structure of carbon monoxide/hydrogen mixtures. Note 1: Detailed kinetic modeling of syngas combustion also in presence of nitrogen compounds, Int. J. Hydrogen Energy, 32, 3471-3485 (2007)

[25] Garnier, E., Adams, N., Sagaut, P., Large Eddy Simulation for Compressible Flows. Springer. New York (2009)

[26] Geurts, B., Elements of direct and large-eddy simulation. R.T.Edwards. Philadelphia (2004)

[27] Gran, I.R., Magnussen, B.F., A numerical study of a bluff-body stabilized diffusion flame. Part 2. Influence of combustion modeling and finite-rate chemistry, J. Combust. Sci. Technol., 119, 191-217 (1996)

[28] Hairer, E., Wanner, G., Solving ordinary differential equations II: Stiff and differential-algebraic problems, 2nd ed. Springer Series in Computational Mathematics. Springer-Verlag (1996)

[29] Harten, A., High resolution schemes for hyperbolic conservation laws, J. Comput. Phys., 49, 357-393 (1983)

[30] Hestens, M., Steifel, E., Methods of conjugate gradients for solving systems of algebraic equations, J. Res. Nat. Bur. Stand, 29, 409-436 (1952)

[31] Hewson, J.C., Kerstein, A.R., Stochastic simulation of transport and chemical kinetics in turbulent CO/H2/N2 flames, J. Combust. Theory Model., 5, 669-897 (2001)

[32] Hottel, H.C., Sarofim, A.F., Radiative Transfer. McGraw-Hill. New York (1967)

[33] Inagaki, M., A new wall-damping function for large eddy simulation employing Kolmogorov velocity scale, Int. J. Heat Fluid Flow, 32, 26-40 (2011)

[34] Inoue, O., Hatakeyama, N., Sound generation by a two-dimensional circular in a uniform flow, J. Fluid Mech., 471, 285-314 (2002)

[35] Isaev, S.A., Baranov, P.A., Kudryavtsev, N.A., Lysenko, D.A., Usachov, A.E., Simulation of a circulation laminar flow around a square cavity with a mobile boundary at high Reynolds numbers with the use of VP2/3 and the FLUENT package, J. Eng. Phys. Thermophys., 78, 799-816 (2005)

[36] Issa, R., Solution of the implicitly discretized fluid flow equations by operator splitting, J. Comput. Phys., 62, 40–65 (1986)

[37] Jacobs, D., Preconditioned conjugate gradient methods for solving systems of algebraic equations, Tech. rep., Central Electricity Research Laboratories, Leatherhead, Surrey, England (1980)

[38] Jasak, H., Weller, H.G., Gosman A.D., High resolution NVD differencing scheme for arbitrarily unstructured meshes, Int. J. Numer. Meth. Fluids, 31, 431–449 (1999)

[39] Jones, W.P., Prasad V.N., Large eddy simulation of the Sandia Flame Series (D-F) using the Eulerian stochastic field method, J. Combust. Flame, 157, 1621-1636 (2010)

[40] Jordan, S., Investigation of the cylinder separated shear-layer physics by large-eddy simulation, Int. J. Heat Fluid Flow, 23, 1-12 (2002)

[41] Kourta, A., Boisson, H., Chassing, P., Ha Minh, H., Non-linear interactions and the transition to turbulence in the wake of a circular cylinder, J. Fluid Mech, 181, 41-161 (1987)

[42] Kravchenko, A., Moin, P., Numerical studies of flow over a circular cylinder at Re = 3900, J. Phys. Fluids, 12, 403-417 (2000)

[43] Launder B., Sharma B., Application of the energy-dissipation model of turbulence to the calculation of flow near a spinning disc, Lett. Heat Mass Transfer, 1, 131-138 (1974)

[44] Launder, B.E., Spalding, D.B., The numerical computation of turbulent flows, J. Comput. Method Appl. M., 3, 269–289 (1974)

[45] Landau, L.D., Lifshitz, E.M., Fluid Mechanics, Course of theoretical physics, 6, 2nd ed. Pergamon (1987)

[46] Li, G., M.F., Application of composition PDF methods in the investigation of turbulence-radiation interactions, J. Quant. Spectrosc. Radiat. Transfer, 73, 461-472 (2002)

[47] Lieuwen, T.C., Unsteady combustor physics, Cambridge University Press. New York (2012)

[48] Lilleberg, B., Ertesvåg, I.S., Rian, K.E., Modeling instabilities in lean premixed turbulent combustors using detailed chemical kinetics, J. Combust. Sci. Technol., 181, 1107–1122 (2009)

[49] Lilleberg, B., On mathematical modeling and numerical simulation of chemical kinetics in turbulent lean premixed combustion, PhD thesis, ISSN 1503-8181, Trondheim (2011)

[50] Lilleberg, B., Christ D., Ertesvåg, I.S., Rian, K.E., Kneer, R., Numerical Simulation with an Extinction Database for Use with the Eddy Dissipation Concept for Turbulent Combustion, J. Flow Turbul. Combust., 91, 319-346 (2013)

[51] Lipatnikov, A., Fundamentals of premixed combustion, CRC Press. Boca Raton (2013)

[52] Liu, K., Pope, S.B., Caughey, D.A., Calculations of bluff-body stabilized flames using a joint probability density function model with detailed chemistry, J. Combust. Flame, 141, 89–117 (2005)

[53] Lourenco, L.M., Shih, C., Characteristics of the plane turbulent near wake of a circular cylinder, a particle image velocimetry study. Published in Ref. [5] (1993)

[54] Lysenko, D.A., Solomatnikov, A.A., Numerical modeling of turbulent heat exchange in the combustion chambers of gas turbine with the use of the FLUENT package, J. Eng. Phys. Thermophys., 76, 888-891 (2003)

[55] Lysenko, D.A., Solomatnikov, A.A., Numerical analysis of aerodynamics and hydraulic loss in the GTE-150 combustion chamber of gas-turbine power plant with the use of the FLUENT suite, J. Eng. Phys. Thermophys., 79, 673-678 (2006)

[56] Magnussen, B.F., Hjertager, B.H., On mathematical modeling of turbulent combustion with special emphasis on soot formation and combustion, Proc. Combust. Inst. 16, 719–729 (1976)

[57] Magnussen, B.F., Modeling of NOx and soot formation by the Eddy Dissipation Concept, Int. Flame Research Foundation, 1st topic Oriented Technical Meeting., 17-19 Oct., Amsterdam, Holland (1989)

[58] Mahmoudi, Y., Sarras, G., Mendez, L.D. Arteaga, Çelik, M., Tummers, M.J., Roekaerts, D.J.E.M., Flame structure and stabilization mechanism of Biogas flame in a jet-in-hot-coflow burner, In proceedings of Eight Mediterranean Combustion Symposium, Çesme, Izmir, Turkey, 8-13 September (2013)

[59] Marshak, R.E., Note on the spherical harmonics method as applied to the Milne problem for a sphere, J. Phys. Rev., 71, 443-446 (1947)

[60] Marzouk, O.A., Huckaby, E.D., A comparative study of eight finite-rate chemistry kinetics for CO/H_2 combustion, J. Eng. App. Comput. Fluid Mech., 4, 331-356 (2010)

[61] McGuirk, J.J., Rodi, W., The calculation of three-dimensional turbulent free jets. In turbulent Shear Flows I: Selected papers from the First International Symposium on Turbulent Shear Flows, editors: Durst, F., Launder, B.E., Schmidt, F.W., and Whitelaw, J.H., Springer-Verlag, Germany, 71-83 (1979)

[62] Menter, F.R., Kuntz, M., Langtry, R., Ten years of experience with the SST turbulence model. In K. Hanjalic, Y. Nagano and M. Tummers, editors, Turbulence, Heat and Mass Transfer 4, Begell House, Inc., 625-632 (2003)

[63] Mihailovic, J., Corke, T.C., Three-dimensional instability of the shear layer over a circular cylinder, J. Phys. Fluids, 9, 3250–3257 (1987)

[64] Parnaudeau, P., Carlier, J., Heitz, D., Lamballais, E., Experimental and numerical studies of the flow over a circular cylinder at Reynolds number 3900, J. Phys. Fluids, 20, 085101 (2008)

[65] Pitsch, H., Steiner, H., Large-eddy simulation of a turbulent piloted methane/air diffusion flame (Sandia Flame D), J. Phys. Fluids, 12, 2541-2554 (2000)

[66] Poinsot, T., Veynante, D., Theoretical and numerical combustion. 2nd ed., Edwards (2005)

[67] Pope, S.B., An Explanation of the turbulent round-jet/plane-jet anomaly, AIAA J., 16, 279-281 (1978)

[68] Prasad A., Williamson, C.H.K., The instability of the shear layer separating from a bluff body, J. Fluid Mech., 333, 375–402 (1997)

[69] Raithby, G.D., Chui, E.H., A finite-volume method for predicting a radiant heat transfer in enclosures with participating media, J. Heat Transfer, 122, 415-423 (1990)

[70] Rajagopalan, S., Antonia R.A., Flow around a circular cylinder—structure of the near wake shear layer, J. Exp. Fluids, 38, 393–402 (2005)

[71] Richardson, L.F., Weather prediction by numerical process. Cambridge University Press, Cambridge (1922)

[72] McGuirk, J.J., Rodi, W., The calculation of three-dimensional turbulent free jets. In turbulent Shear Flows I: Selected papers from the First International Symposium on Turbulent Shear Flows, editors: Durst, F., Launder, B.E., Schmidt, F.W., and Whitelaw, J.H., Springer-Verlag, Germany, 71-83 (1979)

[73] Sabelnikov, V., Fureby, C., LES combustion modeling for high Re flames using a multi-phase analogy, J. Combust. Flame, 160, 83–96 (2013)

[74] Sagaut, P., Large eddy simulation for incompressible flows, 3rd ed. Springer. Berlin (2006)

[75] Salvatici, E., Salvetti, M.V., Large-eddy simulations of the flow around a circular cylinder: effects of grid resolution and subgrid scale modeling, J. Wind Struct., 6, 419–436 (2003)

[76] Shih, T.-H., Liou W., Shabbir, A., Yang, Z., Zhu, J., A new k-ϵ eddy-viscosity model for high Reynolds number turbulent flows – model development and validation, J. Comput. Fluids, 24, 227–38 (1995)

[77] Smagorinsky, J.S., General circulation experiments with primitive equations, J. Mon. Weather Rev., 91, 99–164 (1963)

[78] Smith, T.F., Shen, Z.F., Friedman, J.N. , Evaluation of coefficients for the weighted sum of gray gases model, J. Heat Trans-T., ASME, 104, 602–608 (1982)

[79] Torrence, C., Compo, G.P., A practical guide to wavelet analysis, Bull. Am. Meteorol. Soc., 79, 61-78 (1998)

[80] Turns S.R., An introduction to combustion, concepts and application, 2nd ed. McGraw-Hill (2000)

[81] Vandoormaal, J.P., Raithby, G.D., Enhancements of the SIMPLE method for predicting incompressible fluid flows, J. Numer. Heat Transfer, 7, 147-163 (1984)

[82] Warnatz J., Maas U., Dibble R.W., Combustion, 4th ed. Springer. Berlin Heidelberg New York (2006)

[83] Waterson, N.P., Deconinck, H., Design principles for bounded higher-order convection schemes - a unified approach, J. Comput. Phys., 224, 182–207 (2007)

[84] Welch, P., The use of fast Fourier transform for the estimation of power spectra: a method based on time averaging over short, modified periodograms, IEEE Transactions on Audio Electroacoustics, 15, 70-73 (1967)

[85] Weller, H.G., Tabor, G., Jasak H., Fureby, C., A tensorial approach to computational continuum mechanics using object-oriented techniques, J. Comp. Phys., 12, 620–631 (1998)

[86] Weller, H., Controlling the computational modes of the arbitrarily structured C grid, J. Mon. Weather Rev., 140, 3220–3234 (2012)

[87] Wilkinson, B, Allen, M., Parallel programming: techniques and applications using networked workstations and parallel computers, 2nd ed. Prentice Hall (2004)

[88] Wissink, J.G., Rodi, W., Numerical study of the near wake of a circular cylinder, Int. J. Heat Fluid Flow, 29, 1060–1070 (2008)

[89] Wornom, S., Ouvrard, H., Salvetti, M.V., Koobus, B., Dervieux, A., Variational multiscale large-eddy simulations of the flow past a circular cylinder: Reynolds number effects, J. Comput. Fluids, 47, 44–50 (2011)

[90] Yan, J., Thiele, F., Buffat, M., A turbulence model sensitivity study for CH4/H2 bluff-body stabilized flames, J. Flow Turb. Combust., 73, 1–24 (2004)

[91] Yoshizawa, A., Statistical theory for compressible shear flows, with the application to subgrid modelling, J. Phys. Fluids, 29, 1416-1429 (1986)

Chapter 5

Selected Papers

5.1 Paper A

Computers & Fluids 80 (2013) 408–422

Contents lists available at SciVerse ScienceDirect

Computers & Fluids

journal homepage: www.elsevier.com/locate/compfluid

Modeling of turbulent separated flows using OpenFOAM

Dmitry A. Lysenko [a,*], Ivar S. Ertesvåg [a], Kjell E. Rian [b]

[a] Norwegian University of Science and Technology, Kolbjørn Hejes vei 1B, 7491-NO Trondheim, Norway
[b] Computational Industry Technologies AS, 7462-NO Trondheim, Norway

ARTICLE INFO

Article history:
Received 13 September 2011
Received in revised form 3 January 2012
Accepted 22 January 2012
Available online 3 February 2012

Keywords:
Strong and weak scalability
Compressible URANS
Turbulent separated flows
$k-\epsilon$ turbulence models

ABSTRACT

Turbulent separated planar bluff-body flows were numerically analyzed using the state-of-the-art OpenFOAM and ANSYS FLUENT technologies, based on the conventional URANS approach. Several popular in fluid dynamics test problems such as laminar and turbulent flows over a circular cylinder and turbulent fully developed flows over a triangular cylinder in a channel were numerically replicated with the goal of validation of the selected numerical methods. The detailed, face-to-face comparison between OpenFOAM, FLUENT and experimental data was discussed. Parallel performance in the terms of a strong and weak scalability was assessed up to 1024 cores and compared as well. In general, the present results demonstrated minimum deviations between OpenFOAM and FLUENT and agreed fairly well with the experimental data and other numerical solutions.

1. Introduction

The long-term goal of the present work is to develop URANS (unsteady Reynolds averaged Navier–Stokes) and LES (large-eddy simulation) models for high Reynolds number flows of practical interest with further adaptation for turbulent combustion modeling. The aim of this particular study was to validate a numerical method based on the conventional compressible URANS approach for modeling of turbulent separated flows. Since the flows around bluff-bodies are a common test case for URANS due to the large eddies formed in the wake, several well referenced benchmarks were selected keeping in mind their further adaption for the combustion and LES simulations.

The core numerical method was implemented in the open source OpenFOAM toolbox (hereafter OF). This code was chosen because of several reasons. OF was originally developed as a hi-end C++ classes library (Field Operation and Manipulation) for a broad range of fluid dynamics applications and quickly became very popular in industrial engineering as well as in academic research. OF is open source and there are no limitations for parallel computing and no black boxes compare to commercial solvers like ANSYS FLUENT (hereafter AF). From respect to combustion OF has no limitations for detailed-chemistry modeling (for example, AF has the limit for maximum number of species transport equations). From respect to programing OF is more effective than methods like user-defined functions in AF. The wide list of the numerical schemes and mathematical models, implemented in OF, provides robustness and efficiency of this technology for a wide spectrum of fluid dynamics problems.

Nevertheless, in spite of many attractive features, OF has some disadvantages as well. The most crucial among them is the absence of the quality certification and as a consequence – the lack of high-quality documentation and references. Thus, the problem of OF validation and verification becomes more principal and fundamental

Abbreviations: ΔP, static pressure drop; ΔP, $2\Delta P \Big/ \left(\rho U_\infty^2\right)$; Δt, time step (s); Ω, mean vorticity magnitude; ϵ, dissipation rate of turbulence kinetic energy (m^2/s^3); γ, NVD GAMMA differencing scheme parameter; κ, Von Kármán constant; κ, 0.4187; μ, dynamic molecular viscosity (kg/m/s); μ_τ, turbulent viscosity (kg/m/s); ω, specific rate of turbulence energy dissipation (Hz); ϕ, ratio of specific heats; ρ, mass density (kg/m^3); θ, circumferential coordinate (°); θ_{sep}, mean separation angle (°); v^2, velocity scale; A,B,C, constants; A_μ, A_ϵ, C_1^*, constants; C_μ, constant, $C_\mu = 0.09$; C_d, mean drag coefficient, $C_d = 0.5F_x/\rho_\infty U_\infty^2 Z_x$; C_l, mean lift coefficient, $C_l = 0.5F_y/\rho_\infty U_\infty^2 Z_y$; C_p, mean pressure coefficient, $Cp = 2(P - P_\infty)/\left(\rho U_\infty^2\right)$; $C_{\epsilon 1}$, $C_{\epsilon 3}$, constants in the production and sink terms of the ϵ equation; $C_{p,b}$, mean base suction coefficient; CFL, courant number; D, bluff-body diameter or base (m); $E(p)$, parallel efficiency, $E(p) = T_s/(T_p \times p) = S(p)/p$; F, force in stream-wise direction, consisting of the friction force F_f and the pressure force F_p (Pa); H, channel height (m); K, normalized turbulence kinetic energy, $K = \sqrt{4/3k}/U_\infty$; L, channel length (m); L_r, recirculation zone length (m); M, Mach number, $M = U_\infty/c_\infty$; N, number of cells; P, static pressure (Pa); Pr, Prandtl number; Re, Reynolds number, $Re = \rho_\infty U_\infty D/\mu$; Re_y, turbulent Reynolds number, $Re = \rho y^* \sqrt{k}/\mu$; $S(p)$, strong scalability, $S(p) = T_s/T_p$; St, Strouhal number, $St = f\,D/U_\infty$; T, temperature (K); T_p, execution time using multiple processor system (s); T_s, execution time using single processor system (s); U, velocity magnitude (m/s); $W(p)$, weak scalability, $W(p) = T_p/T_s$; Z, projected bluff-body surface in stream-wise or transverse direction (m); c, speed of sound (m/s); f, Von Kármán vortex shedding frequency (Hz); f_2, function in the sink term of the ϵ equation; k, turbulence kinetic energy, $k = \frac{3}{4}(\langle u'^2\rangle + \langle v'^2\rangle)$ (m^2/s^2); l_μ, l_ϵ, length scales; p, number of processors (cores); t, time (s); u,v, stream-wise and transverse velocity components (m/s); x,y, stream-wise and transverse directions (m); y^*, wall-normal distance (m); Subscripts: ∞, value in an incoming flow; $\langle\rangle$, mean or time-averaged value; o, stagnation value; x,y, stream-wise and transverse components of a vector; $'$, fluctuation component; min, minimum value.

* Corresponding author.
E-mail address: dmitry.lysenko@ntnu.no (D.A. Lysenko).

0045-7930/$ - see front matter © 2012 Elsevier Ltd. All rights reserved.
doi:10.1016/j.compfluid.2012.01.015

compared to other commercial computational fluid dynamics (CFD) codes. The stretched goal of this study is to provide high-quality verification and documentation of the selected numerical methods. With this purpose we performed face-to-face results comparison with the 'best-in-the-class' commercial solver AF. Besides an accurate prediction of the turbulent separated flows with quantitative and qualitative representation of fluid mechanics complexity and behavior, the parallel performance of the numerical method is important as well (specially for unsteady, combustion and LES applications). Therefore a parallel performance was assessed and compared for both codes in terms of a weak and strong scalability up to 1024 cores.

The paper is organized as follows. Test case descriptions are given in Section 2. In Section 3 the main features of the employed numerical methods are summarized. The computational results are presented and analyzed in Section 4 and concluding remarks are given in Section 5.

2. Test cases description

The selected numerical methods were validated against test problems listed and referenced in Table 1. Any of these benchmarks has been replicated numerically with different assumptions and approaches in dozens of papers during several decades. The overall accumulated experience in mathematical and experimental modeling dedicated to these data yields a high level of compliance for any of them.

3. Brief description of numerics

The main emphasis of this work was put on the problem of validation and verification of a numerical method implemented in the OpenFOAM toolbox [10]. However, to achieve a more consistency and validity of the results ANSYS FLUENT [11] was used as well. The quite similar numerical methods were chosen for the present calculations. In both codes, a so-called pressure-density solver, based on the projection method [12] for a solution of compressible URANS equations, was used. One should notice that both codes have the broad lists of turbulence models for the closure problem including one-equation Spalart–Allmaras model, the family of $k-\epsilon$ models, $k-\omega$ SST (Shear Stress Transport) model, etc. In this study the family of $k-\epsilon$ models was chosen based on the strong previous author's experience. Another reason for this pragmatic choice is the fact that $k-\epsilon$ models are still dominant for combustion applications using RANS/URANS approach. The modified low-Reynolds-number $k-\epsilon$ turbulence model of Launder and Sharma (hereafter LSKE) [13] was chosen as the 'baseline' model for OF. This model has been implemented in AF as an undocumented feature, however, we stayed at the Realizable $k-\epsilon$ model (hereafter RKE) [14] for our simulations as 'baseline' for AF. It should be noticed that RKE model is implemented in OF, but in its original high-Reynolds-number formulation only. Special attention was drawn to the treatment of a near-the-wall region. In all cases the low-Reynolds-number formulation was used. With this purpose so-called 'damping functions' were developed in the LSKE model, and a two-layer approach was implemented for the RKE model [11]. A side-by-side comparison of the OF and AF numerical methods, models and assumptions are given in Table 2 with the description in the next several sections.

Table 1
Test matrix of the selected plane bluff-body flows.

Test case description	Re	M	Refs.
Laminar flow over a circular cylinder	140	0.2	[1]
Turbulent flow over a circular cylinder	3900	0.2	[2–6]
Turbulent flow over a triangular rod	1.75×10^4	0.03	[7,8]
Turbulent flow over a triangular rod	4.5×10^4	0.05	[9]

Table 2
OF/AF numerical methods, schemes and models.

	AF	OF
Numerical method		
Algorithm	URANS	
Method	Unstructured FVM	
Solver	Pressure-based	rhoPisoFoam
Pressure–velocity coupling	PISO	PISO
Linear algebra and accuracy	GS/ILU, 10^{-7}	ICCG, 10^{-7}
Multigrid	AMG	–
Under-relaxation factors	Default	0.3 – pressure, 0.7 – others
Spatial discretization		
Convective terms	QUICK	NVD, $\gamma = 0.1$
Pressure	Standard	4th order
Temporal discretization		
Scheme	Implicit dual-stepping	BDF2
Time step	Constant Δt, CFL < 1,	Dynamic $\Delta\, t$, CFL < 1
Thermodynamics		
Compressibility	Ideal gas law	
Dynamic viscosity, μ	Constant, 1.7894×10^{-5}	
Prandtl number, Pr	Constant, 0.75	
Turbulence model		
Modified $k-\epsilon$	RKE	LSKE
Near-the-wall treatment	Low-Reynolds-number formulation	
Boundary conditions		
Inlet	Fixed profiles	
Outlet	Pressure-far-field	Wave-transmissive
Walls	Isothermal non-slip	

3.1. OpenFOAM

The OpenFOAM code [10] v.1.7.1 was used for the numerical simulations. The standard solver rhoPisoFOAM was utilized for the compressible URANS modeling based on the finite-volume (FVM) factorized method [15] and the predictor–corrector PISO (pressure implicit with splitting of operators) algorithm [16]. Two and one iterations were set for a PISO loop and for non-orthogonal corrections, respectively. The generalized fully second-order setup (in space and time) was used for all simulations. The normalized variable diagram (NVD) type differencing scheme – GAMMA [17] with $\gamma = 0.1$ was applied for all convective terms approximation. All other inviscid terms and the pressure gradient were approximated with a fourth order accuracy. A second order implicit Euler method (backward differentiation formula, BDF2 [15]) was used for the time integration together with the dynamic adjustable time stepping technique to guarantee the local Courant number less then CFL < 1. Preconditioned (bi-) conjugate gradient method [18] with incomplete-Cholesky preconditioner (ICCG) by Jacobs [19] was used for solving linear systems with a local accuracy of 10^{-7} for all dependent variables at each time step.

The modified low-Reynolds-number $k-\epsilon$ turbulence model of Launder and Sharma was chosen [13] for the Navier–Stokes equations closure. Such approach does not require the specification of the 'wall-functions' as used in a high-Reynolds-number formulations to describe a near-the-wall region treatment. So-called 'damping functions' were introduced and incorporated in $k-\epsilon$ model by Jones and Launder [50]. It was later re-optimized by Launder and Sharma [13], and demonstrated satisfactory results in many applications. The wide acceptance of such formulation

gradually granted the status of the benchmark for low-Reynolds-number $k-\epsilon$ turbulence model [20]. In this work the model was applied with the following differences in the sink term of the ϵ equation compared to the 'original' LSKE model [13]:

1. Low-Reynolds-number function f_2 was slightly changed: $f_2 = 1 - 0.3\exp\left(-\min\left(\mathrm{Re}_y^2, 50\right)\right)$.
2. The model constant $C_{\epsilon 3}$ was updated from the 'original' value $C_{\epsilon 3} = 2$ to $C_{\epsilon 3} = \left(-0.33 - \frac{2}{3}C_{\epsilon 1}\right)$.

3.2. ANSYS FLUENT

Using the factorized FVM [15] we solved compressible URANS equations with a second order accuracy in space and time. The linear system of equations was solved with Gauss–Seidel smoother or the incomplete lower upper (ILU) decomposition smoothers, which was accelerated by an algebraic multi-grid (AMG) technique, based on the additive-correction strategy [21]. The convective terms were represented according to the Leonard quadratic upwind scheme (QUICK) [11]. It is worth to noticing, that due to its implementation in AF, it is possible to use the QUICK scheme for the unstructured non-hexahedral grids. However in this case the method is switched to a second order upwind discretization scheme. The velocity and pressure fields were matched with a centered computational template within the spirit of Rhie and Chou [22]. The PISO [16] algorithm with a fixed time-stepping for physical-time integration was used.

To close the system of equations we used the Realizable $k-\epsilon$ model of Shih [14]. Originally this model was developed in a high-Reynolds-number formulation. However, a two-layer approach has been employed in FLUENT to specify both the ϵ and the turbulent viscosity in near-the-wall cells. The main idea of this approach is to subdivide a fluid domain in a vicinity of a wall into viscosity-affected and fully-turbulent regions. For this purpose, turbulent Reynolds number, Re_y, is introduced. The boundary between these two regions is defined at $\mathrm{Re}_y^* \equiv 200$. In the fully-turbulent region ($\mathrm{Re}_y > \mathrm{Re}_y^*$) Realizable $k-\epsilon$ model is used. In the viscosity-affected near-the-wall region ($\mathrm{Re}_y < \mathrm{Re}_y^*$) the one equation model of Wolfshtein [23] is employed for the turbulent viscosity calculation, which is computed from: $\mu_\tau = \rho C_\mu l_\mu \sqrt{k}$. The ϵ field in the viscosity-affected region is defined from $\epsilon = k^{3/2}/l_\epsilon$. The length scales ($l_\mu$ and l_ϵ) are calculated according to Chen and Patel [24]:

$$l_\mu = y^* C_l^* (1 - \exp(-\mathrm{Re}_y/A_\mu)),$$
$$l_\epsilon = y^* C_l^* (1 - \exp(-\mathrm{Re}_y/A_\epsilon)),$$

were the dimensionless constants are: $C_l^* = \kappa C_\mu^{-3/4}$, $A_\mu = 70$, $A_\epsilon = 2C_l^*$. The blending functions for a smooth transition between the near-the-wall algebraically predicted ϵ and μ_τ and their values obtained from a solution of the Realizable $k-\epsilon$ model transport equations in the outer region are implemented according to Jongen [25].

3.3. Boundary and initial conditions

The following boundary conditions were applied. Inlet: fixed values for velocity, temperature, turbulence kinetic energy and its dissipation rate; pressure – zero gradient. At the outlet wave-transmissive [26] or characteristic conditions were applied. Bluff-body and channel walls were treated as isothermal no-slip conditions. For the problems where a bluff-body was located in a channel (assuming that the flow is fully-developed and turbulent), additional inlet buffer domains were applied. In such cases the upper and lower buffer domain boundaries were used as symmetry planes. The reason for the inlet buffer domain was to avoid setting of the turbulent velocity and temperature boundary profiles at a channel inlet since it was not measured in lab tests and to avoid investigating the influence of the boundary layer width on the flow development.

The turbulence intensity at the inlet was set equal to 3–4% which is common for the typical wind tunnels. The characteristic scale of the turbulence was set equal to the bluff-body diameter. The molecular viscosity and the thermal conductivity were taken to be constant. The Prandtl number was assumed to be $\mathrm{Pr} = 0.75$, and the ratio of specific heats was $\phi = 1.4$. The compressibility was treated with the ideal gas law. The initial conditions, at the moment of time $t = 0$, corresponded to the conditions of sudden stopping of a bluff-body in a flow, i.e., the input conditions were extended to the whole computational region.

3.4. Data sampling

The turbulent wake has been considered as fully established after a duration of $t = 150D/U_\infty$. Statistics were collected over 40–50 shedding cycles after that. Since the compressible formulation with the stability condition CFL < 1 and the grids with high resolution of boundary layers were used, the typical values of Δt did not exceed 1×10^{-5} s. Thus the number of time steps per one shedding cycle varied in a range of 1000–2000. The main integral flow parameters were: the mean pressure coefficient, mean drag coefficient, mean base suction coefficient, mean separation angle (determined from the condition of vanishing wall shear stress), mean recirculation length (corresponded to the distance between the base of a bluff-body and the sign change of the centerline mean stream-wise velocity) and Strouhal number.

3.5. Mesh independence

It is common knowledge that the disagreement between experimental data and numerical results is determined by two groups of errors (apart from experimental errors): (1) 'model' errors due to the inadequate assumptions made in selecting one turbulence model or another and (2) 'discretization' errors caused by the inadequate resolution of the employed finite-element grids and computational methods. Whereas the errors of the first group are assumed to be 'systematic' under certain assumptions, e.g., for a fixed computational methodology, 'discretization' errors are controlled by the method of adaptation (increase in the resolution) of a computational grid. The grid independence of the present results was confirmed by:

- the application of the two different CFD technologies (AF and OF);
- the use of the projection method [12] for a solution of the compressible URANS equations (or so-called pressure-based solver) with the quite similar implementation in both codes;
- the use of different grid topologies (structured vs. unstructured) and cell types (quadrilateral vs. triangular). This aspect was not discussed there, since the investigated difference between the results obtained for the grids with a different topology could be considered as non-significant (less than 5%) and was discussed in details earlier [27];
- some results of the grid convergence study are presented in Fig. 1. The recirculation zone length was chosen as the most important integral parameter since the quality of its prediction may be considered as the deciding factor about the agreement between experimental and numerical results [6]. One can see clearly that a deviation for L_r as a function of a cells number was bounded by ±2.5%.

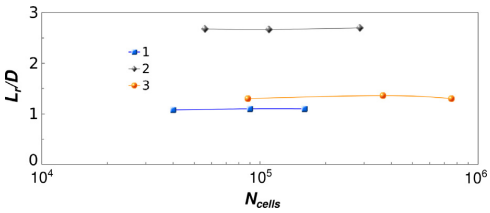

Fig. 1. Grid convergence study for the recirculation zone length: 1 – the flow over a circular cylinder at Re = 3900; 2 – the flow over a triangular rod at Re = 17500; 3 – the flow over a triangular rod at Re = 45000.

3.6. HPC and scalability analysis

Parallel scalability analysis is required to understand and optimize the existing software for high-performance computing (HPC). Both, AF and OF are massive-parallel solvers, based on message-passing (MPI) interface. In general, compressible flow solvers (or so-called density-based) have a higher parallel performance compared to incompressible (and compressible) flow algorithms that are based on projection methods (pressure-based), i.e., they require a solution of the pressure Poisson equation. However, many state-of-the-art numerical algorithms are implemented in an implicit manner, which significantly affects the parallel performance irrespective of the method for solving the Navier–Stokes (NS) equations.

For the assessment of the parallel performance, such parameters as strong scalability, weak scalability and system efficiency were used with their standard definition according to Wilkinson and Allen [28].

The most of the present calculations were carried out using Stallo [29] HPC facility. This system (HP BL 460c cluster) was installed at the end of 2007 and has a total of 704 nodes with 5632 cores. Each computer node has a 2.66 GHz quad-core Intel Xeon processor with 16 GB of memory and 120 GB disk. The facility is provided with 128 TB central storage. AF was not tested since it was not installed at the Stallo. Instead, we used the official AF data available in the literature [30]. The best reported scalability for the pressure-based implicit solver implemented in AF demonstrated at the 2009 Parallel CFD conference (ParCFD 2009) was about 70% up to 512 cores. OF parallel performance, both in terms of strong (starting from $p = 1$) and weak scalability (from $p = 8$), was tested at the Stallo up to $p = 1024$ cores. The code demonstrated quite good weak scalability, which was achieved for a size of $35 \times 35 \times 35$ grid points (43 K) per one core (Fig. 2a) and the modest (Fig. 2b) strong scalability with the average efficiency of ~40%. It should be noted that OF data were collected including all input/output (I/O) operations and that special network-hardware tuning was not maintained. Concluding this paragraph, one can see clearly from Fig. 2b that the parallel performance of the state-of-the-art implicit pressure-based solvers varies from 40–70% of an ideal.

4. Results

4.1. Laminar unsteady flow over circular cylinder

Methodical investigation of the laminar flow around a circular cylinder at Re = 140 was carried out with the goal of validation, verification and understanding of the numerical methods and their capabilities implemented in the OF. Both incompressible and compressible Ma = 0.2 formulations of the URANS approach were applied.

Two types of the grids were used:

- The computational domain for the O-type grid (S1) had the form of a circle (Fig. 3a). A cylinder of diameter, $D = 0.1$ m was located in the center of the computational domain. The size of the integration domain was $20 \times D$. S1 grid was used for the incompressible flow simulation. The grid points were clustered in the vicinity of the cylinder (Fig. 3b). The obstacle as well as the outer boundary profiles were divided into 325 equal intervals. Radial states were divided into 325 intervals with an expansion factor in the radial direction of 1.020. For the compressible flow simulation the O-type grid (S2) with the size of the computational domain of $50 \times D$ was used consisting 600×600 cells. The expansion factor for radial states was the same as for S1.
- Unstructured triangular grid (U1) had the rectangle computational region of a size $L \times H = 6.5$ m $\times$ 2 m. For a consistency with the previous results, the computational domain replicated solutions discussed by Isaev et al. [31]. A cylinder of diameter, $D = 0.1$ m was located at a distance of $17.5 \times D$ from the inlet and symmetrically relative to the upper and bottom boundaries (Fig. 3c). The obstacle was surrounded by a structured ring grid or so-called a viscous boundary layer (BL hereafter) with a minimum near-the-wall step size 5×10^{-6} m (Fig. 3d). The cylinder's surface was divided by 100 equal intervals. The cell size at the outer boundaries was fixed and equal to 0.015 m, leading to smooth grid refinement in the vicinity of a cylinder.

It should be noted that the present results were obtained for OF only. The same data for AF were reported earlier [31]. Figs. 4–6

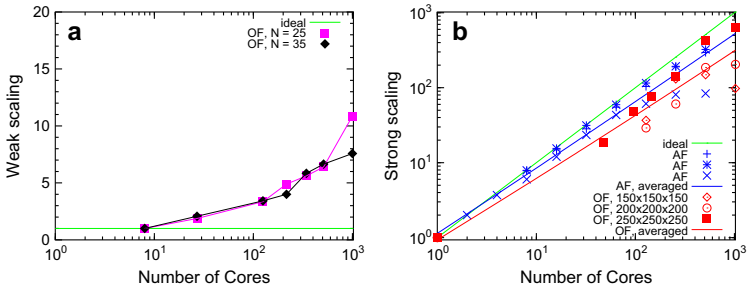

Fig. 2. OF parallel performance. Weak scalability tests (a) for the 3D laminar lid-driven cavity flow using $25 \times 25 \times 25$ (□) and $35 \times 35 \times 35$ (◇) grid points per one core and an ideal case (–). Strong scalability (b) for the 3D laminar lid-driven cavity flow with different grid's sizes: $150 \times 150 \times 150$ (◇), $200 \times 200 \times 200$ (○) and $250 \times 250 \times 250$ (□) with an ideal case (–) and AF data (+, ∗, ×) [30]. Note that OF data include I/O operations.

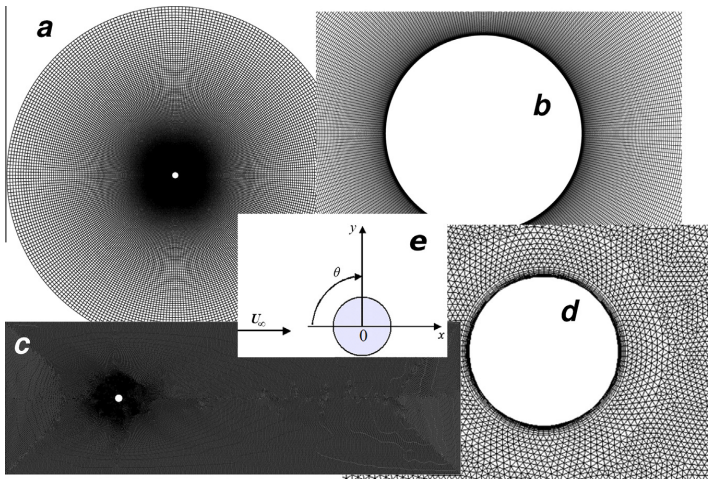

Fig. 3. Description of the grids for the laminar flow over a circular cylinder at Re = 140: S1 (a) and U1 (c) grids and zoom of the near-the-wall regions (b and d), respectively and a general scheme (e).

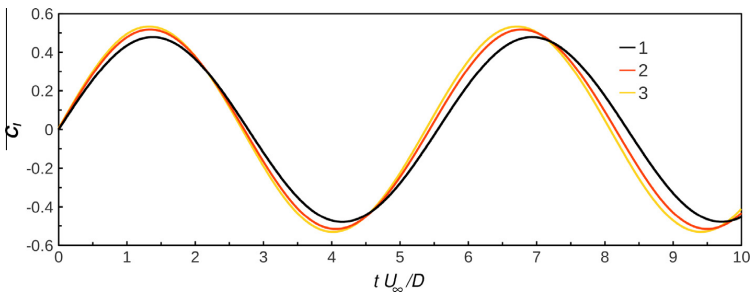

Fig. 4. Time evolution of the lift coefficient for the laminar flow over a circular cylinder at Re = 140 (1 – compressible flow, S2; 2, 3 – incompressible flow, S1 and U1 respectively).

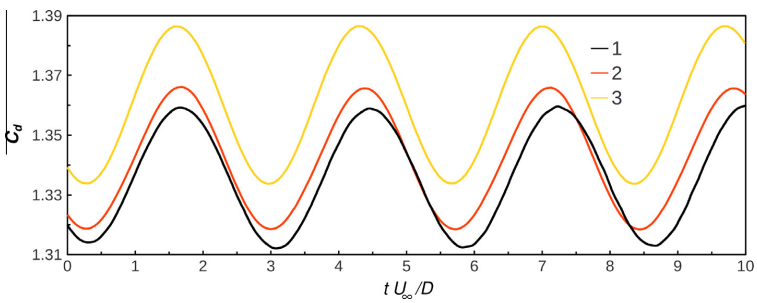

Fig. 5. Time evolution of the drag coefficient for the laminar flow over a circular cylinder at Re = 140. For details, see the caption for Fig. 4.

show some results. The deviations between the lift coefficients, obtained for the different grids and the incompressible/compressible formulation, may be considered as non-significant (Fig. 4). However, the discrepancies for the drag coefficient may be associated with distinct mesh topologies resulted in the slightly different pressure field prediction (Fig. 5). The signals obtained at the O-type grids (1–2) are quite close to each other in opposite to another curve (3) related with the unstructured triangular mesh. With respect to AF, the same trend was confirmed in the previous study [31] as well. The mean drag coefficient was determined in the range C_d = 1.34–1.36. These values agree with the direct numerical simulation (DNS) results reported by Inoue and Hatakeyama [32]

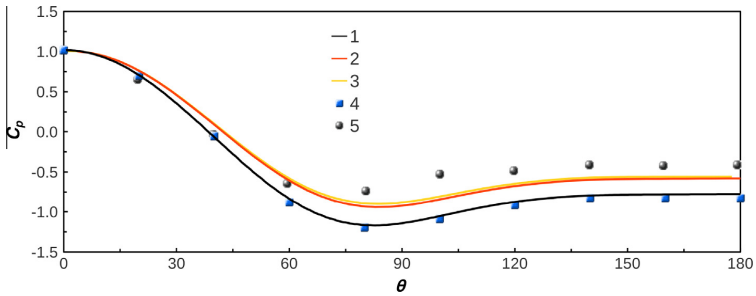

Fig. 6. Mean pressure coefficient distribution over the cylinder's surface for the laminar flow over a circular cylinder at Re = 140: 1–3 – present numerical results (for details, see the caption for Fig. 4); 4 – DNS by Inoue and Hatakeyama [32]; 5 – Experiment by Grove et al. [36].

and with the data obtained by Müller [33]. The amplitudes of the lift and drag coefficients are $C_l' = 0.48—0.53$ and $C_d' = 0.023—0.026$. These non-dimensional force amplitudes are in a good agreement with the values by Inoue and Hatakeyama [32], who report $C_l' = 0.52$ and $C_d' = 0.026$, respectively, for the inlet free stream Mach number M = 0.2. Müller [33] using a high-order finite difference method (HOFDM), got $C_l' = 0.5203$ and $C_d' = 0.02614$, respectively. The calculated recirculation zone length L_r/D = 1.08–1.14 are close to the value obtained by Franke et al. [34] (L_r/D = 1.14).

The computed mean separation angle θ_{sep} = 114° was in a well agreement with the θ_{sep} = 112° obtained by Franke et al. [34]. The detailed analysis of the existed experimental data for the θ_{sep} in the range of 10 < Re < 200 were carried out by Wu et al. [35] who obtained a linear empirical equation for the θ_{sep}–Re relationship

$$\theta_{sep} = 101.5 + 155.2\mathrm{Re}^{-0.5}. \quad (1)$$

Thus, for Re = 140 the experimental mean separation angle was determined to θ_{sep} = 114.6°.

The Strouhal number was computed to St = 0.18–0.184. Inoue and Hatakeyama [32] found the value of St = 0.183 in their DNS. Müller [33] predicted the value of St ≈ 0.1831 in the similar conditions. Williamson [1] discussed in details the Strouhal–Reynolds number relationship for the laminar shedding regime (47 < Re < 200). Williamson [1] demonstrated the single St–Re function with an agreement to the 1% level of St–Re relationship for laminar parallel shedding using different techniques, such as a wind tunnel facility and a water facility known as a towing tank. The generalized St–Re curve proposed by Williamson [1] has the following equation:

$$\mathrm{St} = A/\mathrm{Re} + B + C \cdot \mathrm{Re}, \quad (2)$$

where $A = -3.3265$, $B = 0.1816$, $C = 1.6 \times 10^{-4}$, which leads to the experimental Strouhal number, St = 0.18.

Williamson [1] provided the plot of the mean base suction coefficient over wide range of Reynolds numbers, as well. For Re = 140, the experimental value of $-C_{p,b}$ = 0.84 can be determined and correlates well with the numerically predicted values of $-C_{p,b}$ = 0.842–1.060. The distribution of the time-averaged pressure coefficient over the cylinder's surface is presented in Fig. 6. The numerical results obtained for the compressible flow (1) matched well with the DNS data by Inoue and Hatakeyama [32]. Data from incompressible flow calculations obtained at different grids (2–3) are very close to each other on the one hand, and on the other hand – close to the experimental results by Grove et al. [36]. The gap between the distributions of mean pressure coefficient (1–3) can be explained by the difference in the implementation of NS equations solution algorithms in compressible and incompressible formulations. The DNS as well as the current compressible simulations were carried out for the Mach number M = 0.2. Experimentally measured values by Grove et al. [36] are close to the results obtained with the incompressible flow assumption. Thus, we can expect that the last one was obtained in ambient conditions with the weak compressibility (M < 0.1). It should be noticed that there is some underprediction of integral parameters and fluctuations values in the force coefficients, predicted by AF (Table 3). The main reason for such lower values may be treated as a result of excessive numerical scheme dissipation when the dynamic mesh adaptation algorithm is applied.

4.2. Turbulent flow over a circular cylinder at Re = 3900

The turbulent flow over a circular cylinder at Re = 3900 is probably the more documented one in the literature and can be viewed as a generic benchmark for the sub-critical regime [6]. Available experimental data for this particular test case cover practically most integral (such as forces, wake dynamics, separation angle and recirculation bubble) and local (velocity, vorticity and Reynolds stresses) features of the flow allowing to assess a numerical

Table 3
Integral characteristics for the laminar unsteady flow over a circular cylinder at Re = 140.

Contributors	Method	M	C_d	C_d'	C_l'	St	$-C_{p,b}$	L_r/D	θ_{sep} (°)
Williamson [1]	HWA, PIV					0.180	0.84		
Müller [33]	HOFDM	0.2	1.340	0.026	0.520	0.183			
Inoue and Hatakeyama [32]	DNS	0.2		0.026	0.520	0.183			
Franke et al. [34]	URANS		1.31		0.65	0.194		1.14	112
Isaev et al. [31]	URANS		1.270	0.011	0.400	0.172			
Present									
U1	URANS		1.360	0.026	0.533	0.184	0.842	1.05	115
S1	URANS		1.342	0.024	0.518	0.184	0.860	1.08	114
S2	URANS	0.2	1.340	0.023	0.480	0.180	1.060	1.14	114

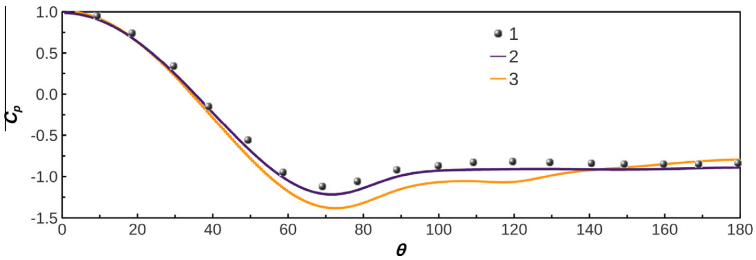

Fig. 7. Mean pressure coefficient distribution on the cylinder's surface at Re = 3900: $\theta = 0°$ is the stagnation point, 1 – experiment by Norberg [4], 2, 3 – present results (OF and AF, respectively).

method qualitatively and quantitatively. In spite of some experimental difficulties (the presence of the recirculation zone and high instantaneous flow angles), there are several hot-wire anemometry (HWA) and particle image velocimetry (PIV) measurements available in the near wake of the circular cylinder. The pioneer work was done by Ong and Wallace [5], who managed to accurately measure velocity and vorticity vectors in the near wake outside the recirculation bubble and proposed turbulence statistics and power spectra of the stream-wise and normal velocity components at several locations. To avoid the restrictions associated with the presence of back flow, the techniques of particle image (PIV) or laser Doppler (LDV) velocimetry are more appropriate [6]. One of the first PIV works for the flow over a circular cylinder at Re = 3900 was the study of Lourence and Shih [2], who performed time resolved measurements in the recirculation region. Statistical quantities were assessed even though this PIV experiment was not designed for this purpose. Nevertheless, these results are often used as reference for validation of numerical simulations in the literature (e.g., [37–39], etc.). Dong et al. [40] investigated the near wake with PIV and direct numerical simulation (DNS) at Re = 3900/4000 and 10000. The main emphasis was drawn on an investigation of the shear-layer instability using DNS data, but a PIV/DNS comparison of mean and turbulent isocontours PIV/DNS maps was discussed also. Recently, the flow over a circular cylinder was studied by Parnaudeau et al. [6] in the near wake at Re = 3900 both numerically (LES) and experimentally with PIV and HWA methods.

The present results were obtained using O-type mesh (S2 from the previous subsection) with the compressible flow assumption using both OF and AF. Two supplementary O-type grids with the spatial resolution 200 × 200 and 400 × 400 were built to confirm the grid convergence.

The distribution of the mean pressure coefficient on the cylinder's surface is plotted in Fig. 7. The calculated data by OF was in a good agreement with the measured values provided by Norberg [4]. However there are some deviations between the experimental and AF data. The detailed analysis of the flow-field in the near wake calculated by AF revealed the existence of two small counter-rotating vortices (beside the main recirculation bubble) attached to the backward side of the cylinder. This finding means that several separation angles (beside the primary θ_{sep}) existed in the AF solution. Breuer [39] got the same results in LES study, using the HYBRID (a combination of the upwind and the central differencing approximations) and HLPA (hybrid linear/parabolic approximation) schemes. From the experimental point of view, the existence of the small vortices at the backward side of the cylinder was confirmed by Son and Hanratty [41]. In Fig. 8 the mean vorticity magnitude (which was non-dimensionalized with the factor $2\sqrt{\mathrm{Re}}$, according to Ma et al. [42]) is plotted along with experimental data. The agreement between the numerical and experimental results was fairy well starting from the stagnation point ($\theta_{sep} = 0°$) til the prime separation angle ($\theta_{sep} \approx 90°$). As known from measurements [2], the separation should take place at $\theta_{sep} = 86°$. This finding was confirmed by Son and Hanratty [41], however it is worth to notice that their experiment was conducted for Re = 5000. The calculated $\theta_{sep} = 88.8°$ by OF and $\theta_{sep} = 89°$ by AF were slight higher the experimental one. At the backward side of the cylinder the OF solution was quite similar to the experimental data [41], however it is did not represent secondary vorticity structures besides the main recirculation zone. The length of the secondary separation zone predicted by AF was $\theta \approx 18°$ while the measured value by Son and Hanratty [41] was $\theta \approx 35°$.

The computed mean drag coefficient $C_d = 0.98–1.07$ and the back-pressure coefficient $-C_{p,b} = 0.99–1.16$ were not much too high (≈10%) compared with experimental measurements of Norberg [4], who measured $C_d = 0.98$ and $-C_{p,b} = 0.90$ respectively. The computed values of the Strouhal number of the vortex shedding frequency St = 0.215–0.216 were found to be within the experimental range of St = 0.20–0.22 (Table 4).

Fig. 9 compares mean stream-wise velocity $\langle u \rangle / U_\infty$ in the wake centerline with the experiments of Lourenco and Shih [2], Parnaudeau et al. [6] and Ong and Wallace [5]. The mean stream-wise

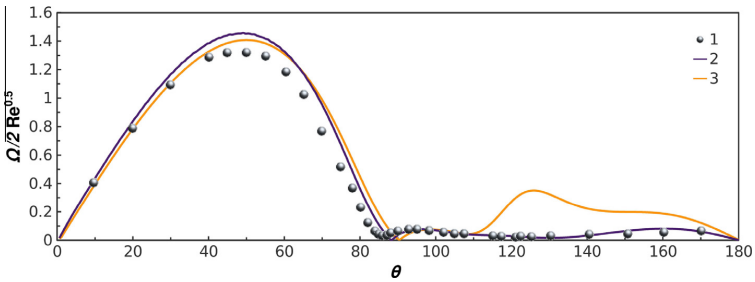

Fig. 8. Mean vorticity magnitude distribution on the cylinder surface at Re = 3900: $\theta = 0°$ is the stagnation point, 1 – experiment of Son and Hanratty [41]; 2, 3 – present results (OF and AF, respectively).

Table 4
Overview of the experimental works and present URANS results of the circular cylinder flow at Re = 3900.

Contributors	Method	M	C_d	St	$-C_{p,b}$	L_r/D	$-\langle u_{min}\rangle/U_\infty$	θ_{sep} (°)
Cardell [3]	HWA			0.215		1.33	0.25	
Lourenco and Shih [2]	PIV		0.99	0.22		1.19	0.24	86
Norberg [4]	HWA		0.98		0.90			
Ong and Wallace [5]	HWA			0.21				
Ma et al., Case II [42]	DNS		0.84	0.22		1.59		
Dong et al. [40]	PIV			0.20		1.36–1.47	0.252	
Dong et al. [40]	DNS			0.20		1.41–1.59	0.291	
Parnaudeau et al. [6]	PIV			0.21		1.51	0.34	
Present								
S2	URANS-LSKE	0.2	1.07	0.22	1.16	1.10	0.19	89
S2	URANS-RKE		0.96	0.19	0.97	1.11	0.20	90
S2	URANS-RKE	0.2	0.98	0.20	0.99	1.03	0.20	89

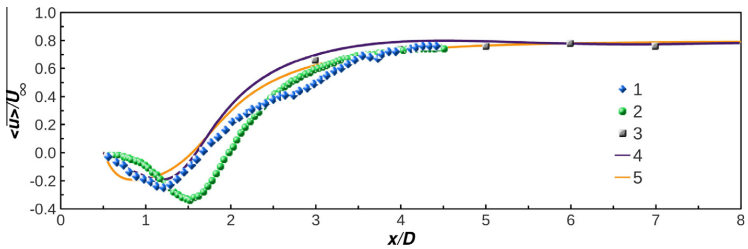

Fig. 9. Mean stream-wise velocity in the wake centerline for the flow over a circular cylinder at Re = 3900 (Experiment: 1 – Lourenco and Shih [2], 2 – Parnaudeau et al. [6], 3 – Ong and Wallace [5]; 4, 5 – present results (OF and AF, respectively)).

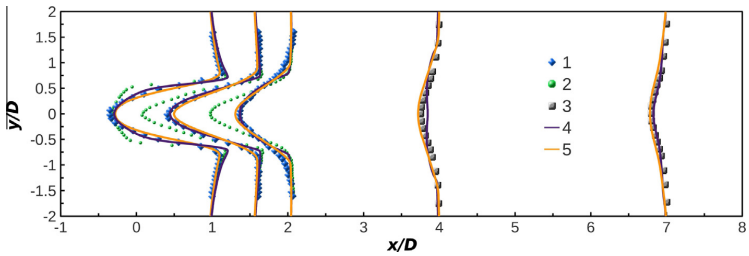

Fig. 10. Mean stream-wise velocity $\langle u\rangle/U_\infty$ at the different locations (x/D = 1.06, 1.54, 2.02, 4.00, 7.00) in the wake of a circular cylinder at Re = 3900. For details, see the caption for Fig. 9.

velocity is zero at the base of the cylinder due to no-slip condition. It reaches a negative minimum $\langle u_{min}\rangle$ in the recirculation zone and converges asymptotically toward U_∞. The present results predicted $\langle u_{min}\rangle/U_\infty = -0.19$ to 0.2, which are in reasonable agreement with the experimental data by Cardell [3], Lourenco and Shih [2] and Dong et al. [40] who reported $\langle u_{min}\rangle/U_\infty = -0.24$ to 0.251. The calculated recirculation zone length L_r/D = 1.03–1.1 are close to the experimental value of Lourence and Shih [2] (L_r/D = 1.19) and DNS (L_r/D = 1.12), performed by Ma et al. [42]. Thus, the present results are closer to the PIV data by Lourenco and Shih [2] and the HWA data by Ong and Wallace [5].

Fig. 10 shows velocity profiles of $\langle u\rangle/U_\infty$. A strong velocity deficit occurs in the region of the recirculation bubble. The mean velocity profiles shows a U-shape close to the cylinder which involves towards a V-shape further downstream. One can observe some non-significant discrepancies between the present results for OF and AF, but in general our calculations agrees well with the experiments by Lourenco and Shih [2] and Ong and Wallace [5].

In Fig. 11 the Reynolds normal stresses $\langle u'u'\rangle/U_\infty^2$ are shown. At x/D = 1.06, the $\langle u'u'\rangle$-profile presents two strong peaks mainly due to the transitional state of the shear layers, which show a flapping behavior due to primary vortex formation [6]. The position of these two peaks agrees with the experiment of Lourenco and Shih [2]. At x/D > 1.06, the two peaks of the shear layers are overlapped by two larger peaks due to primary vortex formation. Overall, the good agreement is observed between the current calculations both for OF and AF and the experimental data of Lourenco and Shih [2] and Ong and Wallace [5]. However, it should be noticed that $\langle u'u'\rangle$-profiles by AF is slightly overshoot the ones by OF, as well as the experimental data.

Table 4 summaries the main integral flow parameters from the experimental and DNS data and the present results.

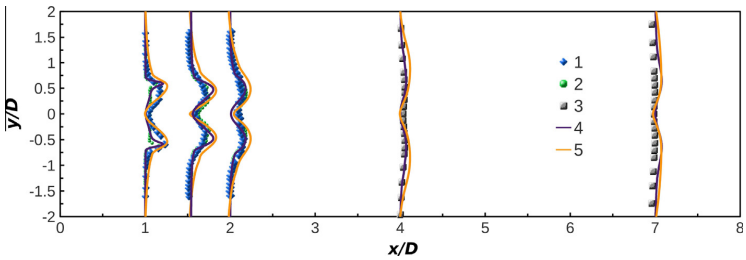

Fig. 11. Variation of the mean stream-wise velocity $\langle u'u' \rangle / U_\infty^2$ at the different locations (x/D = 1.06, 1.54, 2.02, 4.00, 7.00) in the wake of a circular cylinder at Re = 3900. For details, see the caption for Fig. 9.

4.3. Turbulent flow over a triangular rig in a channel – Fujii lab test

LDV measurements by Fujii et al. [8,7] were carried out in an open circuit, forced flow type of wind tunnel at ambient conditions ($P_\infty \approx 100$ kPa, $T_\infty = 280$ K, Re = 17500 and M ≈ 0.03). A sketch is presented in Fig. 12a. An equilateral ($D = 0.025$ m) triangular rod was placed inside the channel passage of 0.05 m-square cross-section.

The two-dimensional computational domain (Fig. 12b) was designed to replicate lab test conditions. The channel length and height were set to $L = 0.305$ m and $H = 0.05$ m, respectively. The bluff-body was located at $x = 0.117$ m from the channel inlet. Two additional buffer domains with length 0.05 m and height 0.1 m were attached to the channel. Note, that this problem was calculated by OF only. Two finite-element baseline grids with different cell types were used (the detailed description is provided in [27]):

- Unstructured triangular mesh (Fig. 12c). Viscous BLs were attached to the obstacle with the following parameters: the first row size 5×10^{-5} m, the growth factor 1.25 and the number of rows 7. The same (except the growth factor) viscous BL was also applied for the channel walls. Each edge of the bluff-body was divided into 80 equal intervals. The computational domain was meshed with the size of 0.001 m, which guarantees smooth triangular element distribution from the inlet and outlet to the triangular rod. All these features provided good near-the-wall mesh resolution and allowed to apply the low-Reynolds-number $k - \epsilon$ turbulence model.
- Baseline unstructured quadrilateral mesh (Fig. 12d) was designed in the same manner (UQ1).
- To check solution mesh independence, two additional grids were built, both with the quad cells (UQ0 and UQ2). The type of the attached viscous BLs was the same as in the baseline quad mesh and domain was meshing with sizes of 0.0015 m and 0.0005 m, respectively.

Time-averaged measured and numerically predicted streamlines are presented in Fig. 13. The results of the CFD analysis provide a more extended length of the reversed zone, $L_r/D = 2.67$ compared to the measured one, $L_r/D = 2.2$. Time-averaged pressure coefficient distribution downstream the bluff-body inside the recirculation bubble is shown in Fig. 14. Numerical results demonstrate quite similar behavior with the experimental data. Minimum values were also in a good agreement between numerical ($C_{p,min} = -2.7$) and measured ($C_{p,min} = -2.73$) data.

The normalized turbulence kinetic energy in the wake is provided in Fig. 15. Overall, the good qualitative and quantitative agreement for the K between lab test and numerical modeling data was achieved.

The time history of the instantaneous transverse velocity are presented in Fig. 16. As expected, periodic sinusoidal type signals

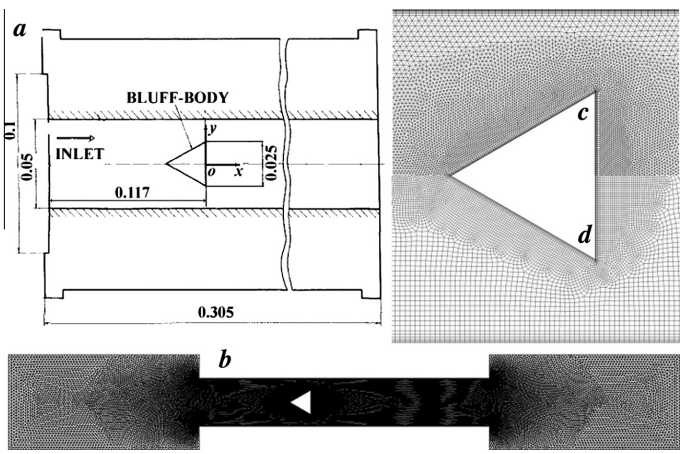

Fig. 12. A general view of the experimental test rig (a) taken from [7], the computational domain (b) and the fragments of the designed unstructured viscous grids (c and d) at the vicinity of the bluff-body.

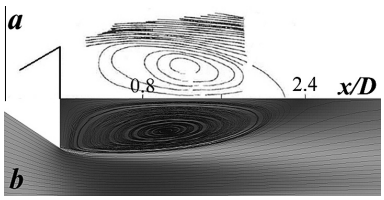

Fig. 13. Time-averaged streamlines for the flow past a triangular rod in a channel at Re = 17500: a – experiment by Fujii et al. [7,8], b – present results (UQ1).

that were obtained clearly illustrate self-regular vortex shedding behavior of the wake. The averaged calculated Strouhal number was, St = 0.44, with the corresponding main frequency, f = 177 Hz. This is in a quite good agreement with the experimental values, where a pronounced frequency, f = 160 Hz, and the corresponding Strouhal number St = 0.4, was detected.

Table 5 summaries the integral flow features for this problem.

4.4. Turbulent flow over a triangular rig in a channel – Volvo test rig

Fig. 17a shows a schematic drawing of the test section. The test set-up consisted of a straight channel with a rectangular cross-section, divided into an inlet section length 0.5 m and a channel passage section length L = 1 m and 0.12 m × 0.24 m cross-section. The inlet section was used for flow straightening and turbulence control. The air entering the inlet section was distributed over the cross-section by a critical plate that, at the same time, isolated the channel acoustically from the air supply system. The channel passage section ended in a circular duct with a large diameter. The triangular bluff-body (with base diameter, D = 0.04 m) was mounted with its reference position 0.681 m upstream of the channel exit.

The cold flow measurements were conducted in the ambient conditions (T_∞ = 288 K, P_∞ = 100 kPa, Re = 45000, and M = 0.05). Honeycombs and screens controlled the approximate inlet turbulence level of 3–4%. A two-component LDA system was used for the stream-wise and transverse velocity components and its

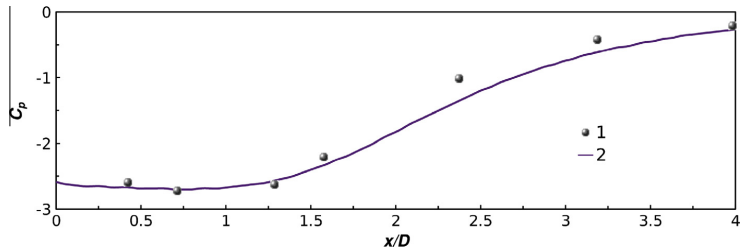

Fig. 14. Mean pressure coefficient in the wake centerline for the flow over a triangular rod in a channel at Re = 17500: 1 – experiment by Fujii et al. [7,8], 2 – present results (UQ1).

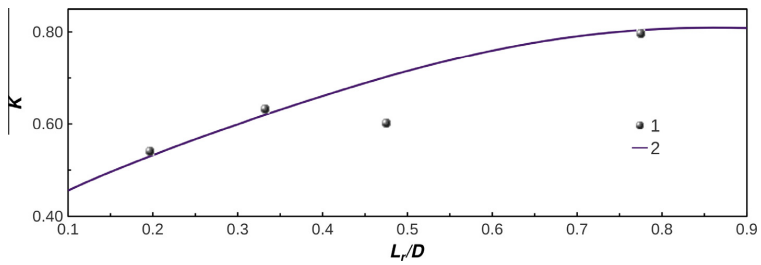

Fig. 15. Normalized turbulence kinetic energy in the wake centerline for the flow over a triangular rod in a channel at Re = 17500: 1 – experiment by Fujii et al. [7,8], 2 – present numerical data (UQ1).

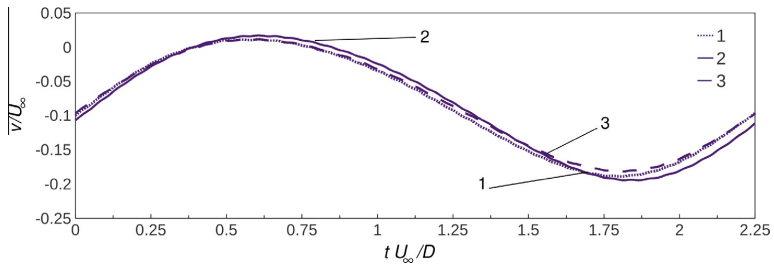

Fig. 16. Time history of the instantaneous transverse velocity at the designed grids UQ0–UQ2 (1–3, respectively). The reference point was located at the same position as in the lab test of Fujii et al. [7,8] with the coordinates: x/D = 1.2, y/D = 0.6.

Table 5
Integral parameters for Fujii lab test simulations.

Contributors	Method	M	$-C_{p,min}$	L_r/D	St
Fujii et al. [8,7]	LDV		2.73	2.2	0.40
Present					
UQ1	URANS-LSKE		2.7	2.67	0.45
UQ1	URANS-LSKE	0.03	2.65	2.87	0.45

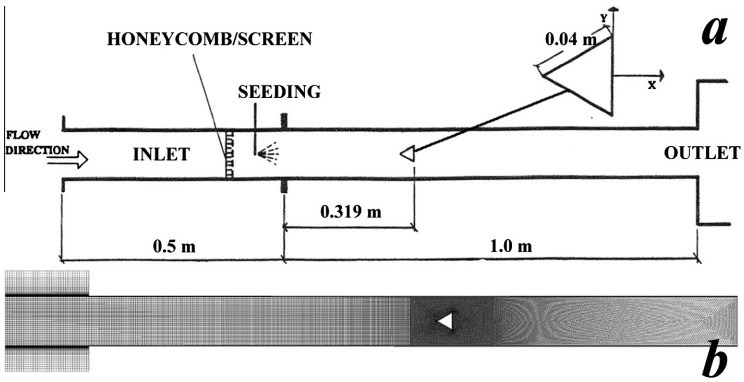

Fig. 17. The sketch of the Volvo test rig (a) taken from Ref. [9] and the general view of the computational domain (b).

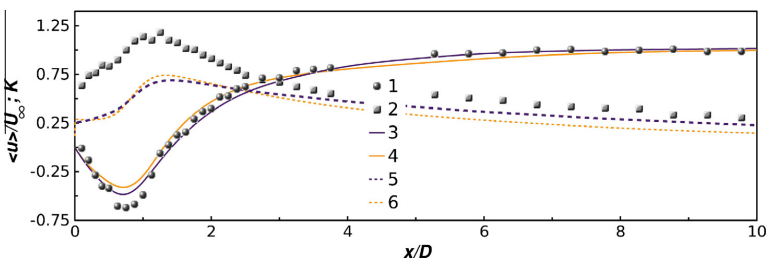

Fig. 18. Mean stream-wise velocity (1,3,4) and normalized turbulence kinetic energy (2,5,6) in the wake centerline for the flow over a triangular rod in a channel at $Re = 45000$: 1, 2 – experiment by Sjunnesson et al. [9]; 3, 5 – present results, OF; 4,6 – present results, AF.

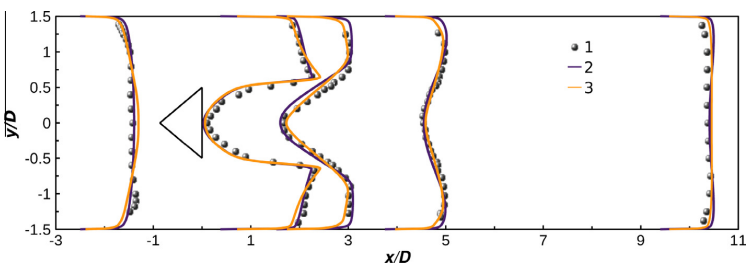

Fig. 19. Mean stream-wise velocity $\langle u\rangle/U_\infty$ at the different locations ($x/D = -2.5$, 0.375, 1.525, 3.75, 9.4) in the channel flow with a triangular rod at Re = 45000: 1 – experiment by Sjunnesson et al. [9]; 2, 3 – present results (OF and AF, respectively).

fluctuations measurements. Further detailed description of the LDA system, experimental procedure and sampling technique can be found in [9].

The computational grids were built in the same spirit as for the previous test problem. Four unstructured grids were designed (with a detailed description provided in [27]): quadrilateral, partially triangular UT1 (Fig. 17b) and two supplementary partially triangular grids (UT0, UT2) to check grid convergence. The results presented in this section were obtained using UT1 for both OF and AF.

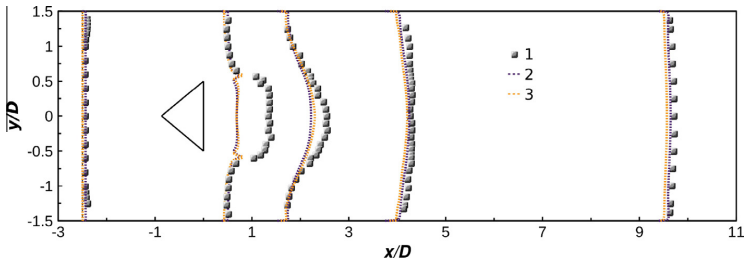

Fig. 20. Normalized turbulence kinetic energy K at the different locations ($x/D = -2.5, 0.375, 1.525, 3.75, 9.4$) in the channel flow with a triangular rod at Re = 45000: 1 – experiment by Sjunnesson et al. [9]; 2, 3 – present results (OF and AF, respectively).

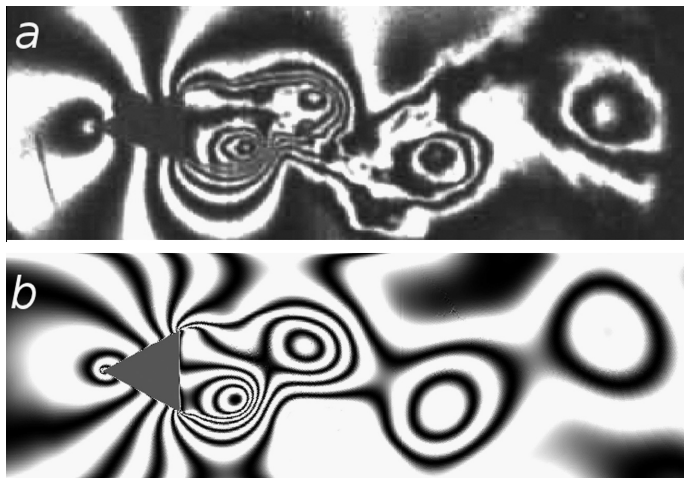

Fig. 21. Flow visualization of the vortex shedding behind a triangular rod: a – the experimental interferogram taken from Nakagawa [46]; b – numerical interferogram (OF).

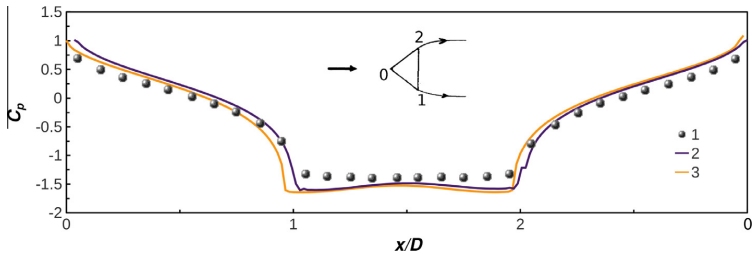

Fig. 22. Mean surface pressure coefficient distribution on the sides of a triangular rod: 1 – experiment by Tatsuno et al. [48], 2, 3 – present results (OF and AF, respectively).

Figs. 18–23 represent some results. As was reported by Sjunnesson et al. [9], the experimental profile of stream-wise velocity component was slightly skewed due to small misalignment in the flange between the inlet section and the channel passage. However, fully symmetrical inlet velocity profile was implicitly formed during flow development in the numerical simulations. In both cases one could observe the outer regions of BLs at the channel walls, which corresponded very well with the '1/7 power law profile' typical for fully developed turbulent channel flows.

Fig. 18 shows the measured and predicted mean stream-wise velocity $\langle u \rangle / U_\infty$ and normalized turbulence kinetic energy K along the central-line behind the obstacle. It should be noticed a ≈18% undershoot compared to the experimental data for the $\langle u_{min} \rangle / U_\infty$ in the recirculation zone independently of the grid type and numerical methods. But, overall, there is a good match between numerical and experimentally measured data. For example, the same level of undershoot was observed by Hasse et al. [43] for URANS (with $k - \omega$ SST) data. Present numerical results showed good prediction for the recirculation lengths: calculated $L_r/D = 1.36$ (OF) and $L_r/D = 1.32$ (AF) in comparison with the measured [9] value of $L_r/D = 1.33$ and with the numerically predicted value of $L_r/D = 1.3$ by Durbin [44] and Johansson et al. [45]. The recirculation zone

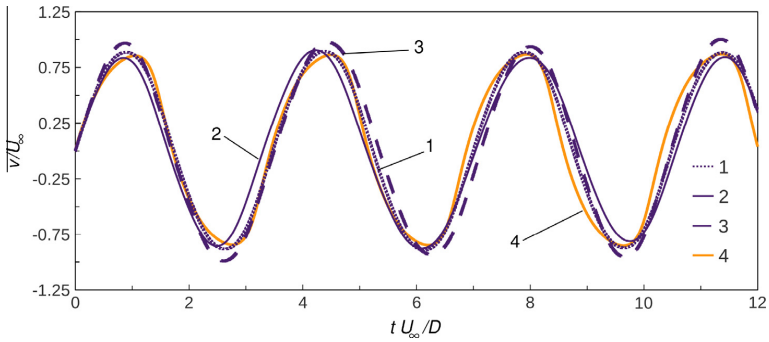

Fig. 23. Time history of the instantaneous transverse velocity: 1–3 – OF (UT0-UT2), respectively; 4 – AF (UT1). The reference point was located at the same position as in the lab test of Sjunnesson et al. [9] with the following coordinates: $x/D = 1$, $y/D = 0$.

lengths obtained by Hasse et al. [43] for URANS-SST and detached eddy simulation (DES) were only 0.94 and 1.18, respectively. In Fig. 18 the comparison between measured and numerically predicted normalized turbulence kinetic energy in the wake is shown as well. One can observe the same trend between experimentally measured values and the data, obtained by numerical modeling, since the latter significantly underpredict the level of fluctuations inside the recirculation zone. This indicates that the vortex shedding was much stronger in the physical experiment.

Figs. 19 and 20 show the mean stream-wise velocity and normalized turbulence kinetic energy at several locations in the channel. Overall, there are minimal discrepancies between the numerical data predicted by OF and AF, as well as the experimental data by Sjunnesson et al. [9]. At the same time, as was mentioned already, a strong underprediction of numerically predicted turbulence kinetic energy was observed inside the recirculation zone. Meanwhile, the same level of turbulence kinetic energy was contained both in the downstream of the bluff-body and in the upstream part of channel, after the separation bubble was vanished.

A numerically predicted frequency of von Kármán vortex shedding matched quite well to experimental data: $f = 117$ Hz (OF) and $f = 118$ Hz (AF) vs. $f = 105$ Hz in experimental data, and St = 0.28 vs. St = 0.25, respectively, which are differences of about 10%. These results correspond well also with those obtained by Hasse et al. [43]: $f = 122$ Hz and $f = 117$ Hz peak frequencies for URANS and DES, respectively.

Fig. 21 shows the experimental [46] and numerical interferograms of the flow. The visualization of the instantaneous density field was done using numerical interferogram technique according to Hadjadj and Kudryavtsev [47]. In spite of the slight different flow conditions between the experiment by Nakagawa [46] (M = 0.377 and $\mathrm{Re} = 1.73 \times 10^5$) and the present calculations, the agreement between them was fairly well. The shear layers separated from the upper and lower trailing edges delineate the boundary of the vortex formation region behind the triangular cylinder. The main vortices are generated alternately at the upper and lower trailing edges, and subsequently shed downstream. It is worthy to note that no secondary vortices are generated around a triangular rod.

Although the accuracy of the pressure loss measurements was not too high, as it was mentioned in [9], it is still of interest in many engineering applications. The experimental value for the normalized pressure drop was measured (between axial states $x/D = -5$ and $x/D = 10$) to $\Delta P = 0.6$ while the numerically predicted value was $\Delta P \approx 0.7$ (both for OF and AF), which correspond quite well between each other. Despite the fact that many researchers have used this test for validation, nobody has not compared pressure distribution at the surface of a prism yet. Here, the experiment of Tatsuno et al. [48] was adopted (Fig. 22). One should notice satisfied agreement between the present numerical and experimental results although the measurements were carried out in the slight different conditions ($\mathrm{Re} = 9 \times 10^4$).

Table 6
Integral parameters for Volvo lab test simulations.

Contributors	Method	M	L_r/D	St	ΔP
Sjunnesson et al. [9]	LDA		1.33	0.250	0.6
Johansson et al. [45]	URANS-SKE		1.30	0.270	
Durbin [44]	URANS-KEV2		1.30	0.285	
Strelets [49]	URANS-SA		0.90		
Hasse et al. [43]	URANS-SST		0.94	0.296	
Present					
UT1	URANS-LSKE		1.57	0.28	0.7
UT1	URANS-LSKE	0.05	1.36	0.28	0.7
UT1	URANS-RKE	0.05	1.3	0.28	0.7

Finally, Fig. 23 shows the time history of the transverse velocity measured at the same probe location using OF and AF. The variation between the curves are quite small (about ±5% both for the frequencies and amplitudes). Table 6 summaries the main integral flow features available in the literature for this problem and the present results.

4.5. Discussion

Several well referenced turbulent separated bluff-body problems were analyzed numerically with the conventional URANS approach based on two state-of-the art CFD technologies (OpenFOAM and ANSYS FLUENT).

The influence of 'discretized' errors on the solutions were validated and confirmed by the independence from grids topology and applied numerical schemes and factors (CFD codes). For all present results carried out with OF and AF, the same computational grids were used for the each test problem. Preliminary results [27] showed that the influence of the grids topology could be considered as non-significant (the difference between results were less than 5%). To check the mesh independence the grid convergence study was performed for the most principal flow parameter such as the recirculation zone bubble behind a bluff-body. As was discussed, the test cases were calculated using the compressible formulation. Since a limited number of the problem-related articles were found in the literature, and all cited numerical analysis were carried out with incompressible flow assumption, we can regard that these data can be considered as the first one where

a compressible URANS approach has been applied for the selected test cases.

The influence of the 'temporal discretization' errors was not analyzed in the present study. Usually the spatial discretization error effect is larger than the error arising from time integration [15]. It may be shown that for fully developed turbulent flows the implicit schemes appear less efficient compared to explicit methods [15]. However, the main advantage of the adopted implicit BDF2 scheme is a larger stability region compared to the explicit methods, which is important in case of combustion applications. Moreover, in case of fully developed turbulent flows existed small time and space scales are simply advected by the most energetic eddies [15]. This argument yields an accuracy time-scale similar to the CFL criterion. Thus in all present calculations the stability condition CFL < 1 was employed which had to guarantee that actual time-step was close to accuracy time step.

To check solutions sensitivity to the compressible effects several additional runs were conducted within the incompressible URANS approach. Preliminary results [27] indicated first of all, that there were not significant deviations for the selected test cases between the compressible and incompressible runs for the main integral flow features except the recirculation zone length. The reverse zone length could be varied significantly in a range of ±25% for all selected benchmarks, that can be observed from Tables 3–6. The minimum deviation (≈5%) is observed for the laminar flow over a circular cylinder at Re = 140.

One of the possible explanations can be the following. From the isentropic theory the local and total densities can be related

$$\rho_o/\rho = \left(1 + \frac{\phi - 1}{2}\mathrm{M}^2\right)^{\frac{1}{\phi - 1}}. \tag{3}$$

It may be shown that for the subsonic flows (M < 1): $\rho/\rho_0 = 1 - \mathrm{M}^2/2$. The deviation in a solution using the incompressible assumption strongly depends from M, e.g., the Mach number should not exceed 0.14 to achieve 1% error. However, the present results indicated that the maximum local Mach number values were 0.3–0.4. These high Mach number areas were located just behind a bluff-body and delineated from a vortex formation region by separated sheared layers. Thus, a recirculation zone region was corrected by the compressibility effect.

To assess local compressibility effects we compared the local mean stream-wise velocity (Fig. 24) and normalized turbulence kinetic energy (Fig. 25) for the compressible and incompressible flows over a triangular rod in a channel at Re = 45000 (Volvo test case). One can observe some expected deviations between solutions in the reverse zone area for the mean stream-wise velocity due to the difference in the predictions of the recirculation bubble. The normalized turbulence kinetic energy had the same trends however the incompressible solution under-shoot the compressible one, which in its turn under-shoot the experimental one. This is interesting finding since the inlet values of the turbulence intensity were the same as in the experiment for both numerical cases.

Two different implementations of the $k - \epsilon$ turbulence model were used to check the 'modeling' error influence. As it was shown both versions of this turbulence model were capable to predict the flow physics reasonably well. It is worth to notice, that no wall functions were used in any of simulations. The difference between the principal flow characteristics obtained with RKE and SHKE models was quite acceptable and did not exceed 10%. The only one issue was identified concerning the formation of the small vortices at the backward side of the cylinder's surface besides the primary recirculation bubble for the flow over a circular cylinder at Re = 3900. However, as was mentioned by Breuer [39], the structure and the length of the recirculation bubbles behind the cylinder were strongly influenced by the numerical scheme. In our case the OF was not able to predict the secondary vortices contrary to the AF.

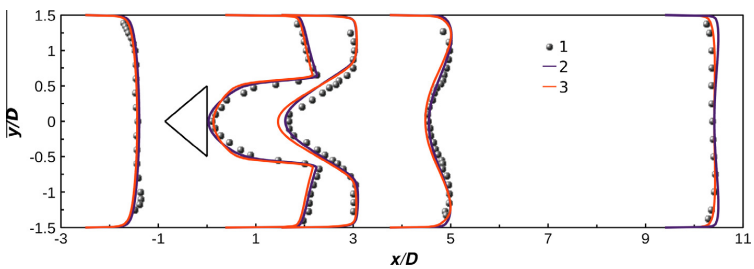

Fig. 24. Mean stream-wise velocity $\langle u \rangle / U_\infty$ at the different locations ($x/D = -2.5$, 0.375, 1.525, 3.75, 9.4) in the channel flow with a triangular rod at Re = 45000: 1 – experiment by Sjunnesson et al. [9]; 2, 3 – present compressible and incompressible results (OF, UT1), respectively.

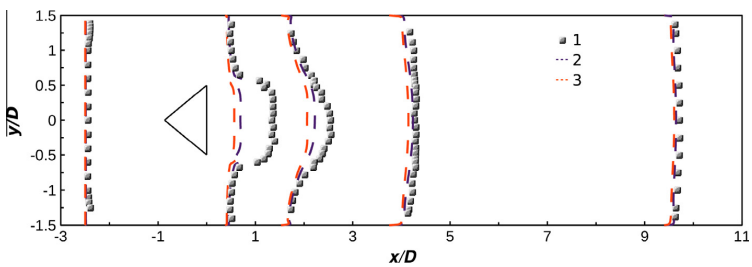

Fig. 25. Normalized turbulence kinetic energy K at the different locations ($x/D = -2.5$, 0.375, 1.525, 3.75, 9.4) in the channel flow with a triangular rod at Re = 45000: 1 – experiment by Sjunnesson et al. [9]; 2, 3 – present compressible and incompressible results (OF, UT1), respectively.

5. Concluding remarks

The objective of the present work was an extensive investigation on the numerical aspects influencing the quality of compressible URANS solutions, implemented in the OpenFOAM toolbox. With this purpose several well-referenced turbulent massively separated bluff-body benchmarks were selected and analyzed numerically. The commercial code ANSYS FLUENT was used to provide detailed face-to-face results analysis with OpenFOAM. Comparison of the numerical estimates using the OpenFOAM and ANSYS FLUENT technologies and the most frequently applied in engineering semi-empirical differential models of turbulence, has shown that they are close and are practically independent of the grid used. The parallel performance of OpenFOAM was analyzed up to 1024 cores and shown the modest parallel efficiency of ≈40%. In general, the URANS results agreed fairly well with the experimental data and other numerical solutions. All these indicated on the adequacy and accuracy of the established numerical method based on the OpenFOAM and its readiness for further combustion application development.

Acknowledgment

This work was conducted as a part of the CenBio Center for environmentally-friendly energy. We are very appreciated to the Norwegian Meta center for Computational Science (NOTUR) for providing the uninterrupted HPC computational resources and the useful technical support.

References

[1] Williamson C. Vortex dynamics in the cylinder wake. Ann Rev Fluid Mech 1996;28:477–539.
[2] Lourenco L, Shih C. Characteristics of the plane turbulent near wake of a circular cylinder, a particle image velocimetry study. Tech. rep., Published in [37]; 1993.
[3] Cardell G. Flow past a circular cylinder with permeable splitter plate. Tech. rep., Data taken from Mittal [38]; 1993.
[4] Norberg C. Experimental investigation of the flow around a circular cylinder: influence of aspect ratio. J Fluid Mech 1994;258:287–316.
[5] Ong L, Wallace J. The velocity field of the turbulent very near wake of a circular cylinder. Exp Fluids 1996;20:441–53.
[6] Parnaudeau P, Carlier J, Heitz D, Lamballais E. Experimental and numerical studies of the flow over a circular cylinder at Reynolds number 3900. Phys Fluids 2008;20(8):085101.
[7] Fujii S, Gomi M, Eguchi K. Cold flow tests of a bluff body flame stabilizer. ASME J 1978;100:323–32.
[8] Fujii S, Eguchi K. A comparison of cold and reacting flows around a bluff body flame stabilizer. ASME J 1981;103:328–34.
[9] Sjunnesson A, Nelsson C, Erland M. LDA measurements of velocities and turbulence in a bluff body stabilized flame. Tech. rep., Volvo Flygmotor AB, Trollhättan, Sweden; 1991.
[10] Weller H, Tabor G, Jasak H, Fureby C. A tensorial approach to computational continuum mechanics using object-oriented techniques. J Comput Phys 1998;12(6):620–31.
[11] ANSYS FLUENT R12. Theory guide. Tech. rep., Ansys Inc.; 2009.
[12] Chorin A. Numerical solution of Navier–Stokes equations. J Math Comput 1968;22:745–62.
[13] Launder B, Sharma B. Application of the energy-dissipation model of turbulence to the calculation of flow near a spinning disc. J Lett Heat Mass Transfer 1974;1:131–8.
[14] Shih T-H, Liou W, Shabbir A, Yang Z, Zhu J. A new $k-\epsilon$ eddy-viscosity model for high Reynolds number turbulent flows – model development and validation. J Comput Fluids 1995;24(3):227–38.
[15] Geurts B. Elements of direct and large-eddy simulation. R.T.Edwards; 2004.
[16] Issa R. Solution of the implicitly discretized fluid flow equations by operator splitting. J Comput Phys 1986;62:40–65.
[17] Jasak H, Weller H, Gosman A. High resolution NVD differencing scheme for arbitrarily unstructured meshes. Int J Numer Methods Fluids 1999;31:431–49.
[18] Hestens M, Steifel E. Methods of conjugate gradients for solving systems of algebraic equations. J Res Nat Bur Stand 1952;29:409–36.
[19] Jacobs D. Preconditioned conjugate gradient methods for solving systems of algebraic equations. Tech. rep., Central Electricity Research Laboratories, Leatherhead, Surrey, England; 1980.
[20] Cotton M, Kirwin P. A variant of the low-Reynolds-number two-equation turbulence model applied to variable property mixed convection flows. Int J Heat Fluid Flow 1995;16(6):486–92.
[21] Hutchinson B, Raithby G. A multigrid method based on the additive correction strategy. J Numer Heat Transfer 1986;9:511–37.
[22] Rhie C, Chow W. Numerical study of the turbulent flow past an airfoil with trailing edge separation. AIAA J 1983;21(11):1525–32.
[23] Wolfshtein M. The velocity and temperature distribution of one-dimensional flow with turbulence augmentation and pressure gradient. Int J Heat Mass Transfer 1969;12:301–18.
[24] Chen H, Patel V. Near-wall turbulence models for complex flows including separation. AIAA J 1988;26(6):641–8.
[25] Jongen T. Simulation and modeling of turbulent incompressible flows. Ph.D. thesis, EPT Lausanne, Lausanne, Switzerland; 1992.
[26] Poinsot T, Lele S. Boundary conditions for direct simulations of compressible viscous flows. J Comput Phys 1992;101:104–29.
[27] Lysenko D, Ertesvåg I, Rian K. Turbulent bluff body flows modeling using OpenFOAM technology. In: Skallerud B, Andersson HI, editors. Computational mechanics, Trondheim; 2011. p. 189–208.
[28] Wilkinson B, Allen M. Parallel programming: techniques and applications using networked workstations and parallel computers. 2-nd ed. Prentice Hall; 2004.
[29] <http://www.notur.no/hardware/stallo/>.
[30] <http://www.ansys.com/Support/Platform+Support/Benchmarks+Overview>.
[31] Isaev S, Baranov PA, Kudryavtsev NA, Lysenko DA, Usachev AE. Comparative analysis of the calculation data on an unsteady flow around a circular cylinder obtained using the VP2/3 and FLUENT packages and the Spalart-Allmaras and Menter turbulence models. J Eng Phys Thermophys 2005;78(6):1199–213.
[32] Inoue O, Hatakeyama N. Sound generation by a two-dimensional circular in a uniform flow. J Fluid Mech 2002;471:285–314.
[33] Müller B. High order numerical simulation of aeolian tones. J Comput Fluids 2008;37:450–62.
[34] Franke R, Rodi W, Schönung B. Numerical calculation of laminar vortex shedding flow past cylinders. J Wind Eng Ind Aerodyn 1990;35:237–57.
[35] Wu M-H, Wen C-Y, Yen R-H, Weng M-C, Wang A-B. Experimental and numerical study of the separation angle for flow around a circular cylinder at low Reynolds number. J Fluid Mech 2004;515:233–60.
[36] Grove A, Shair F, Petersen E, Acrivoss A. An experimental investigation of the steady separated flow past a circular cylinder. J Fluid Mech 1964;19:60–80.
[37] Beaudan P, Moin P. Numerical experiments on the flow past a circular cylinder at sub-critical Reynolds number. Tech. rep., Technical report TF-62, CTR Annual Research Briefs, NASA Ames/Stanford University; 1994.
[38] Mittal R. Progress on les of flow past a circular cylinder. in: Annual research briefs. Tech. rep., Center of Turbulence Research, Stanford University; 1996.
[39] Breuer M. Large eddy simulation of the sub-critical flow past a circular cylinder: numerical and modeling aspects. Int J Numer Methods Fluids 1998;28:1281–302.
[40] Dong S, Karniadakis G, Ekmekci A, Rockwell D. A combined direct numerical simulation particle image velocimetry study of the turbulent air wake. J Fluid Mech 2006;569:185–207.
[41] Son J, Hanratty T. Velocity gradients at the wall for flow around a cylinder at Reynolds numbers from 5×10^3 to 10^5. J Fluid Mech 1969;35(2):353–68.
[42] Ma X, Karamanos G-S, Karniadakis G. Dynamics and low-dimensionality of a turbulent near wake. J Fluid Mech 2000;410:29–65.
[43] Hasse C, Sohm V, Wetzel M, Durst B. Hybrid URANS/LES turbulence simulation of vortex shedding behind a triangular flameholder. J Flow Turbul Combust 2009;83:1–20.
[44] Durbin P. Separated flow computations with the $k-\epsilon-v^2$ model. AIAA J 1995;33:659–64.
[45] Johansson S, Davidson L, Olsson E. Numerical simulation of vortex shedding past triangular cylinders at high Reynolds number using a $k-\epsilon$ turbulence model. Int J Numer Methods Fluids 1993;16:859–78.
[46] Nakagawa T. Vortex shedding mechanism from a triangular prism in a subsonic flow. J Fluid Dyn Res 1988;5:69–81.
[47] Hadjadj A, Kudryavtsev A. Computation and flow visualization in high-speed aerodynamics. J Turbul 2005;6(16):33–81.
[48] Tatsuno M, Takayama T, Amamoto H, Ishi-i K. On the stable posture of a triangular or a square cylinder about its central axis in a uniform flow. J Fluid Dyn Res 1990;6:201–7.
[49] Strelets M. Detached eddy simulation of massively separated flows. In: AIAA aerospace sciences meeting and exhibit, January 8–11; 2001/Reno, NV; 2001.
[50] Jones W, Launder B. The prediction of laminarization with a two-equation model of turbulence. Int J Heat Mass Transfer 1972;15:301–14.

5.2 Paper B

Noname manuscript No.
(will be inserted by the editor)

Numerical simulation of non-premixed turbulent combustion using the Eddy Dissipation Concept

Dmitry A. Lysenko · Ivar S. Ertesvåg · Kjell Erik Rian

Received: date / Accepted: date

Abstract Numerical simulations of the Sandia flame CHNa and the Sydney bluff-body stabilized flame HM1E are reported and the results are compared to available experimental data. The numerical method is based on compressible URANS/LES formulations which were implemented recently in the OpenFOAM toolbox. In this study, the calculations are carried out using the conventional compressible URANS approach and a standard k-ϵ turbulence model. The Eddy Dissipation Concept with a detailed chemistry approach is used for the turbulence-chemistry interaction. The syngas (CO/H_2) chemistry diluted by 30% nitrogen in the Sandia flame CHNa and CH_4/H_2 combustion in the Sydney flame HM1E are described by the full GRI-3.0 mechanism. A robust implicit Runge-Kutta method (RADAU5) is used for integrating stiff ordinary differential equations to calculate the reaction rates. The radiation is treated by the P1-approximation model. In general, there is good agreement between present simulations and measurements for both flames, which indicates that the proposed numerical method is suitable for this type of combustion, provides acceptable accuracy and is ready for further combustion application development.

Keywords Sandia Flame CHNa · Sydney Flame HM1E · Compressible Reynolds-Averaged Simulations · RADAU5 · Eddy Dissipation Concept · OpenFOAM

Dmitry A. Lysenko · Ivar S. Ertesvåg
Department of Energy and Process Engineering, Norwegian University of Science and Technology, Kolbjørn Hejes vei 1B, NO–7491, Trondheim, Norway
Tel.: +47-73-593755
Fax: +47-73-593580
E-mail: dmitry.lysenko@ntnu.no

Kjell Erik Rian
Computational Industry Technologies AS, NO–7462, Trondheim, Norway

1 Introduction

The long-term goal of the present work is to develop a large-eddy simulation (LES) model for high Reynolds number flows of practical interest with further adaptation for turbulent combustion modeling. The core numerical method is based on the OpenFOAM toolbox which was originally developed as a high-end C++ classes library (Field Operation and Manipulation) for a broad range of fluid dynamics applications. Today, the OpenFOAM toolbox is very popular in industrial engineering as well as in academic research (for example, there are at least two annual international conferences dedicated to the library development and evaluation). Previously, methodical investigations for several turbulent bluff-body flows have been carried out with the goal of verification, validation and understanding of the capabilities of the numerical method using the conventional approach for solution of the unsteady compressible Reynolds-averaged Navier-Stokes equations (URANS) [32]. These results were analyzed in detail and agreed fairly well with experimental data.

Recently, Lilleberg et al.[30] carried out several turbulent combustion calculations of well-known detailed flame experiments such as the Sandia Flames D, E [2] and a piloted lean-premixed jet burner (PPJB) [10], [11]. Lilleberg and his co-workers [30] used a classical approach for the solution of the steady, compressible Reynolds-averaged Navier-Stokes (RANS) equations, where the turbulence was treated via a standard k-ϵ model [28] and several ways of coupling chemical kinetics with the Eddy Dissipation Concept (hereafter EDC) [15] were adopted. As was expected, the detailed chemistry approach showed the best agreement with the measured data for all cases.

In the present study, the solver originally developed by Lilleberg et al.[30] was updated to the unsteady, compressible Reynolds-averaged Navier-Stokes (URANS) equations. The turbulence-chemistry interaction was treated according to the Eddy Dissipation Concept with the detailed chemistry approach. The validation was extended with two benchmark flames: the Sandia flame CHNa [3] and the Sydney bluff-body flame HM1E [9]. The Sandia flame CHNa has the advantage of a simple geometry, which enables modelers to focus on the role of the turbulence and chemical kinetic models in the simulations, and minimizes other factors related to so-called 'discretization errors' [36]. Thus, it was possible to investigate the influence of chemical kinetics, turbulence-chemistry interaction and radiation heat transfer for this flame. Bluff-body stabilized flames are still a challenging case for turbulent combustion modeling due to the complexity of the turbulent flow and finite-rate chemistry, which results in high dimensionality and requires integration of stiff differential equations of chemical kinetics [31].

The paper is divided into six main parts. The first and the second parts of the paper describe the mathematical and numerical modeling, respectively. Then, a general description of the test cases is given. Finally, computational results are presented, analyzed and discussed, and conclusions are drawn.

2 Mathematical modeling

2.1 Governing equations

The Favre-averaged (i.e. mass-density-weighted) equations of mass, momentum and energy for the turbulent compressible flows are:

$$\frac{\partial \bar{\rho}}{\partial t} + \frac{\partial}{\partial x_j}\left(\bar{\rho}\tilde{u}_j\right) = 0 \tag{1}$$

$$\frac{\partial}{\partial t}\left(\bar{\rho}\tilde{u}_i\right) + \frac{\partial}{\partial x_j}\left(\bar{\rho}\tilde{u}_i\tilde{u}_j\right) = -\frac{\partial \bar{p}}{\partial x_i} + \frac{\partial}{\partial x_j}\left(\bar{\tau}_{ij} - \bar{\rho}\widetilde{u_i'' u_j''}\right) \tag{2}$$

$$\frac{\partial}{\partial t}\left(\bar{\rho}\tilde{h}\right) + \frac{\partial}{\partial x_j}\left(\bar{\rho}\tilde{h}\tilde{u}_j\right) = \frac{\partial}{\partial x_j}\left(\bar{\rho}\alpha\frac{\partial \tilde{h}}{\partial x_j} - \bar{\rho}\widetilde{u_j'' h''}\right) - \frac{\partial}{\partial x_j}\left(\bar{q}_r\right) + \bar{S}_{hc} \tag{3}$$

Here, the overbar denotes Reynolds averaging, while the tilde denotes Favre averaging: ρ denotes the density, u is the velocity, p is the pressure, $h = \sum_s Y_s \int C_{p,s}\, dT$ is the enthalpy, T is the temperature, Y_s is the species mass fraction, $C_{p,s}$ is the heat capacity for species s in the mixture, α is the thermal diffusivity, q_r represents the radiative heat loss and S_{hc} represents the source term due to combustion.

Here, $C_{p,s}$ is calculated as a function of temperature from a set of coefficients taken from NIST-JANAF thermochemical tables [5]. The thermal diffusivity is modeled as

$$\bar{\rho}\alpha = \mu\frac{C_v}{C_{pBar}}\left(1.32 + 1.77\frac{R}{C_v}\right), \tag{4}$$

where μ is the molecular viscosity (calculated according to the Sutherland law), R is the gas constant, C_v represents heat capacity at constant volume and

$$C_{pBar} = \frac{\partial T \partial h + C_p}{\left(\partial T\right)^2 + 1}. \tag{5}$$

Here, $\partial T = \tilde{T} - T_{ref}$, $\partial h = \tilde{h}\left(T\right) - \tilde{h}\left(T_{ref}\right)$ and C_p is the mixture heat capacity at constant pressure.

$\bar{S}_{hc}$ is modeled according to

$$\bar{S}_{hc} = -\sum_{s=1}^{N}\frac{\bar{\omega}_s}{M_s}h_{f,s}^{\theta}, \tag{6}$$

where $h_{f,s}^{\theta}$ is the species formation enthalpy, M_s is the species molecular weight and ω_s is the species reaction rate.

The turbulence flux $\widetilde{u_j'' h''}$ is derived according to the gradient hypothesis

$$-\bar{\rho}\widetilde{u_j'' h''} \approx \frac{\mu_t}{\mathrm{Pr}_t}\frac{\partial \tilde{h}}{\partial x_j} \tag{7}$$

where μ_t is the turbulence viscosity and Pr_t is a turbulence Prandtl number (here $\mathrm{Pr}_t = 0.7$).

For a mixture of N_s species (where $s = 1 \dots N_s$), a transport equation for the mean mass fraction of an individual species Y_s can be defined according to

$$\frac{\partial}{\partial t}\left(\bar{\rho}\tilde{Y}_s\right) + \frac{\partial}{\partial x_j}\left(\bar{\rho}\tilde{Y}_s\tilde{u}_j\right) = \frac{\partial}{\partial x_j}\left(\left(\bar{\rho}D_{m,s} + \frac{\mu_t}{\mathrm{Sc}_t}\right)\frac{\partial \tilde{Y}_s}{\partial x_j}\right) + \bar{\omega}_s,\ s = 1, \dots, N_s \tag{8}$$

where $D_{m,s}$ is the mass diffusion coefficient for species s in a mixture, Sc_t is the turbulence Schmidt number ($\mathrm{Sc}_t = \mu_t/\rho \mathrm{D}_t$, where D_t is a turbulence diffusivity). Here, Fick's law is introduced and the diffusion coefficient was set equal for all species, $D_{m,s} = D_m = 2.88 \times 10^{-5}$ m^2/s. The turbulence Schmidt number was set to 0.7. Finally, the temperature is related to the density and the pressure by the ideal gas law.

The stress tensor for a Newtonian fluid is expressed as

$$\bar{\tau}_{ij} = \mu\left(\frac{\partial \tilde{u}_i}{\partial x_j} + \frac{\partial \tilde{u}_j}{\partial x_i}\right) - \frac{2}{3}\mu\delta_{ij}\frac{\partial \tilde{u}_k}{\partial x_k}. \tag{9}$$

The Reynolds stresses are modeled according to

$$\bar{\rho}\widetilde{u_i'' u_j''} = -\mu_t\left(\frac{\partial \tilde{u}_i}{\partial x_j} + \frac{\partial \tilde{u}_j}{\partial x_i} - \frac{2}{3}\delta_{ij}\frac{\partial \tilde{u}_k}{\partial x_k}\right) + \frac{2}{3}\bar{\rho}\tilde{k}\delta_{ij} \tag{10}$$

The standard k-ϵ model [28] is based on the turbulence kinetic energy ($\tilde{k}$) and its dissipation rate ($\tilde{\epsilon}$). The turbulence viscosity is defined here as $\mu_t = C_\mu \bar{\rho}\tilde{k}^2/\tilde{\epsilon}$.

The modeled transport equations are:

$$\frac{\partial}{\partial t}\left(\bar{\rho}\tilde{k}\right) + \frac{\partial}{\partial x_j}\left(\bar{\rho}\tilde{k}\tilde{u}_j\right) = \frac{\partial}{\partial x_j}\left(\left(\mu + \frac{\mu_t}{\sigma_k}\right)\frac{\partial \tilde{k}}{\partial x_j}\right) + G - \bar{\rho}\tilde{\epsilon} \tag{11}$$

$$\frac{\partial}{\partial t}\left(\bar{\rho}\tilde{\epsilon}\right) + \frac{\partial}{\partial x_j}\left(\bar{\rho}\tilde{\epsilon}\tilde{u}_j\right) = \frac{\partial}{\partial x_j}\left(\left(\mu + \frac{\mu_t}{\sigma_\epsilon}\right)\frac{\partial \tilde{\epsilon}}{\partial x_j}\right) + C_{\epsilon 1}\frac{\tilde{\epsilon}}{\tilde{k}}G - C_{\epsilon 2}\bar{\rho}\frac{\tilde{\epsilon}^2}{\tilde{k}} \tag{12}$$

where μ is the molecular viscosity, and the rate of turbulence kinetic energy production G is given as

$$G = -\bar{\rho}\widetilde{u_i'' u_j''}\frac{\partial \tilde{u}_i}{\partial x_j} \tag{13}$$

The standard values [28] are used for the model constants C_μ,$C_{\epsilon 1}$, $C_{\epsilon 2}$, σ_k and σ_ϵ.

2.2 EDC for turbulent combustion

The Eddy Dissipation Concept for turbulent combustion [34],[15] is based on the energy cascade model [48]. The EDC assumes that molecular mixing and chemical reactions occur in the fine structures of the turbulent flow where the smallest dissipative eddies are present. The characteristic length L^* and velocity u^* scales of the fine structures are of the same order of magnitude as the Kolmogorov scales and can be expressed as

$$L^* = \frac{2}{3}\left(\frac{3C_{D2}^3}{C_{D1}^2}\right)^{1/4}\left(\frac{\nu^3}{\tilde{\epsilon}}\right)^{1/4} \tag{14}$$

$$u^* = \left(\frac{C_{D2}}{3C_{D1}^2}\right)^{1/4}(\nu\tilde{\epsilon})^{1/4} \tag{15}$$

where $C_{D1} = 0.134$ and $C_{D2} = 0.5$ [15]. The RANS-based EDC assumes that the full cascade takes place at each numerical cell, and the connection between the fine structure and the larger eddies is achieved through the cascade. Thus, characteristics of the large eddies such as the velocity u' are evaluated using the turbulence model (in the present case, the standard $k-\epsilon$ model).

In the model expressed below, different superscripts refer to states inside the fine structures (*), the surroundings ($\circ$) and the mean values of the computational cell ($\sim$).

The ratio between the mass in the fine structures and the total mass is postulated as

$$\gamma^* = \left(\frac{u^*}{u'}\right)^2 = \left(\frac{3C_{D2}}{4C_{D1}^2}\right)^{1/2}\left(\frac{\nu\tilde{\epsilon}}{\tilde{k}^2}\right)^{1/2} \tag{16}$$

The mass exchange between the fine structures and the surroundings, divided by the mass of the fine structures, is defined as

$$\dot{m}^* = 2\frac{u^*}{L^*} = \left(\frac{3}{C_{D2}}\right)^{1/2}\left(\frac{\tilde{\epsilon}}{\nu}\right)^{1/2} \tag{17}$$

The mass exchange between the fine structures and the surroundings, divided by the total mass, is calculated according to

$$\dot{m} = \gamma^*\dot{m}^* \tag{18}$$

The mass-averaged mean reaction rate for the s specie is given as

$$-\bar{\omega}_s = \frac{\bar{\rho}\dot{m}\zeta}{1-\gamma^*\zeta}\left(\tilde{Y}_s - Y_s^*\right),\ s = 1,\ldots,N_s \tag{19}$$

and the relationship between the mass-averaged mean state, fine-structure state and surrounding state is expressed as

$$\tilde{\Psi} = \gamma^*\zeta\Psi^* + (1-\gamma^*\zeta)\Psi^\circ \tag{20}$$

Here, ζ is the reacting fraction of the fine structures, which can depend on the probability of co-existence of the reactants, the degree of heating and reaction limitations. In the present study, $\zeta = 1$, as suggested by Gran and Magnussen [17]. The mean mass fraction $\widetilde{Y}_s$ for species s is calculated from solving the species mass transport equation for each individual species. The fine-structure mass fraction Y_s^* is computed through the detailed chemistry approach.

2.3 EDC detailed chemistry approach

The finite-rate chemical kinetics are taken into account by treating the fine structures as constant pressure and adiabatic homogeneous reactors. Thus, the fine structures mass fractions values Y_s^* can be calculated by solving a system of ordinary differential equations (ODE) describing a Perfectly Stirred Reactor (PSR) [17],

$$\frac{dY_s^*}{dt} = \frac{\omega_s^*}{\rho^*} + \frac{1}{\tau^*}\left(Y_s^\circ - Y_s^*\right),\ s = 1, \ldots, N_s \tag{21}$$

The reaction rate ω_s^* is evaluated from a chemical kinetics mechanism. Y_s° is the mass fraction of the inflow stream to the reactor. In the present study, it is assumed adiabatic and isobaric PSRs. Further, it is assumed that the PSRs are at steady state [17], meaning that the steady-state solution of Eq.21 is achieved by integrating it in time to steady state.

It is worth noticing that the residence or mixing time scale τ^* is evaluated using the molecular viscosity and the dissipation rate

$$\tau^* = \frac{1}{\dot{m}^*} \tag{22}$$

The chemical kinetic mechanism GRI-3.0 [4] is used for modeling of both test cases. This mechanism has been specially designed for combustion of natural gas with air and contains 325 elementary reactions and 53 species.

Another kinetic model, consisting of 34 elementary reactions and 14 species [14], is also used for syngas combustion (Sandia Flame CHNa). This mechanism has been developed specially for the applications of syngas combustion by Frassoldati, Faravelli and Ranzi [14] and was validated against a set of experimental measurements (including plug flow reactor, PSR, shock tubes and ignition delay times, laminar flame speed, and ignition in a counter-flow flame). We assigned the acronym FFR to this mechanism, which is formed by the first letters of the developer's last names [14] in the spirit of Marzouk and Huckaby [36].

2.4 The mixture fraction probability density function model

In the present study the mixture fraction, f is defined as [53]

$$f = \frac{Z_i - Z_{i,ox}}{Z_{i,fuel} - Z_{i,ox}}, \tag{23}$$

where Z_i is the elemental mass fraction for element i. The subscripts ox and fuel denote the value at the oxidizer and fuel stream inlets, respectively. Using the standard assumptions of the equal diffusion coefficients for all species, and assuming that the considered flow is turbulent, (where turbulent convection overwhelms molecular diffusion), f is the elemental mass fraction. The Favre-mean transport equation for $\tilde{f}$ and its variance $\widetilde{f''^2}$ [26] are

$$\frac{\partial}{\partial t}\left(\bar{\rho}\tilde{f}\right)+\frac{\partial}{\partial x_j}\left(\bar{\rho}\tilde{u}_j\tilde{f}\right)=\frac{\partial}{\partial x_j}\left(\frac{\mu_t}{\mathrm{Sc}_t}\frac{\partial\tilde{f}}{\partial x_j}\right), \tag{24}$$

$$\frac{\partial}{\partial t}\left(\bar{\rho}\widetilde{f''^2}\right)+\frac{\partial}{\partial x_j}\left(\bar{\rho}\tilde{u}_j\widetilde{f''^2}\right)=\frac{\partial}{\partial x_j}\left(\frac{\mu_t}{\mathrm{Sc}_t}\frac{\partial\widetilde{f''^2}}{\partial x_j}\right)+C_g\mu_t\left(\frac{\partial\tilde{f}}{\partial x_j}\right)^2-C_d\bar{\rho}\frac{\tilde{k}}{\tilde{\epsilon}}\widetilde{f''^2}, \tag{25}$$

where $f^{''}=f-\tilde{f}$, $\mathrm{Sc}_t=0.85$, $C_g=2.86$ and $C_d=2$.

In the present study a chemical equilibrium assumption is used, where reactions rates are sufficiently fast for the mixture to be in a state of chemical equilibrium. With this assumption the equilibrium state of density, temperature and composition can be obtained by minimizing the free energy [53].

The instantaneous values of mass fractions, density, temperature and enthalpy depend on the instantaneous mixture fraction:

$$\phi_i=\phi_i\left(f,h\right). \tag{26}$$

For the turbulence-chemistry interaction the assumed-shape probability density function (PDF) is used. Density weighted scalars are calculated as

$$\widetilde{\phi_i}=\int_0^1\tilde{p}\left(f\right)\phi_i\,df. \tag{27}$$

In the present study, the PDF's are specified by tilde as Favre-probability-density functions. The β-function is used to model $\tilde{p}\left(f\right)$.

The non-adiabatic extension for this model is based on the assumption that the enthalpy fluctuations are independent on the enthalpy level:

$$\widetilde{\phi_i}=\int_0^1\tilde{p}\left(f,\tilde{h}\right)\phi_i\,df, \tag{28}$$

and

$$p\left(f,\tilde{h}\right)=\tilde{p}\left(f\right)\delta\left(h-\tilde{h}\right), \tag{29}$$

where δ is the Delta function. Further, Eqs. 28-29 require solution of the model transport equation for the total enthalpy [21]

$$\frac{\partial}{\partial t}\left(\bar{\rho}\tilde{h}\right)+\frac{\partial}{\partial x_j}\left(\bar{\rho}\tilde{u}_j\tilde{h}\right)=\frac{\partial}{\partial x_j}\left(\frac{k_t}{C_p}\frac{\partial\tilde{h}}{\partial x_j}\right)-\frac{\partial}{\partial x_j}\left(\bar{q}_r\right), \tag{30}$$

where k_t is the turbulence thermal conductivity and C_p is the specific heat capacity. $\tilde{h}$ is defined in the following way:

$$\tilde{h} = \sum_{s=1}^{N} \tilde{Y_s} \widetilde{h_s}, \tag{31}$$

where $\tilde{Y_s}$ is the mass fraction of the species s and

$$\widetilde{h_s} = h_s^0 \left(T_{ref}\right) + \int_{T_{ref}}^{\tilde{T}} C_{p,s}\, dT \tag{32}$$

and $h_s^0 \left(T_{ref}\right)$ is the formation enthalpy of the species s at the reference temperature T_{ref}.

2.5 The steady laminar flamelet (SLF) model

The laminar flamelet model represents the turbulent flame as an ensemble of thin, laminar, locally one-dimensional flamelet structures embedded within the turbulent flow field [42]. In this case the chemical time and length scales need not be resolved and the flame could be described by the mixture fraction and the strain rate (or the scalar dissipation, χ).

The instantaneous scalar dissipation is defined as

$$\chi = 2D_f \left| \frac{\partial f}{\partial x_j} \right|^2, \tag{33}$$

where D_f is a diffusion coefficient $\rho D_f = \alpha / Cp$.

It is assumed that the mixture fraction f to be given in the flow field as a function of space and time. The surface of stoichiometric mixture can be determined from [42]

$$f(x, y, z, t) = f_{st}. \tag{34}$$

The concept of a laminar diffusion flamelets in a turbulent diffusion flame has been introduced by Williams [56]. Combustion takes place in a thin layer in the vicinity of this surface if the local mixture fraction gradient is sufficiently high. This thin layer and the surrounding inert mixing region is called a laminar diffusion flamelet [42].

The flamelet equations for the species mass fractions and temperature can be derived by application of a universal coordinate transformation and subsequent asymptotic approximation (where the scalars T and Y_s are expressed as functions of the the mixture fraction f) [42]

$$\rho \frac{\partial Y_s}{\partial t} = \frac{1}{2} \rho \chi \frac{\partial^2 Y_s}{\partial f^2} + \omega_s, \tag{35}$$

$$\rho \frac{\partial T}{\partial t} = \frac{1}{2} \rho \chi \frac{\partial^2 T}{\partial f^2} + \frac{1}{C_p} \frac{\partial p}{\partial t} - \sum_{s=1}^{N} h_s \omega_s. \tag{36}$$

Eqs. 35 – 36 rely on the Shvab-Zeldovich formulation of the species mass fraction and energy equations, which involves the approximation of unity Lewis numbers for all species [43].

The flamelet strain rate α_S can be related to χ if f is not small as [42]

$$\chi = \frac{\alpha_S}{\pi} \exp\left(-2\left(\mathrm{erfc}^{-1}\left(2f\right)\right)^2\right), \tag{37}$$

where erfc^{-1} represents the inverse complementary error function.

Flamelets are generated at scalar dissipation values as

$$\chi_i = \begin{cases} 10\chi_{i-1} & \text{for } \chi_{i-1} < 1\ \mathrm{s}^{-1} \\ \chi_{i-1} + \Delta\chi & \text{for } \chi_{i-1} \geq 1\ \mathrm{s}^{-1} \end{cases}, \tag{38}$$

where i ranges from 1 to the specified number of flamelets, χ_0 is the initial scalar dissipation, and $\Delta\chi$ is the scalar dissipation step. Here, $i = 1 \ldots 25$, $\chi_0 = 0.01\ \mathrm{s}^{-1}$ and $\Delta\chi = 5\ \mathrm{s}^{-1}$. The finite-rate chemistry effects are taken into account by treatment of the FFR and the GRI3.0 mechanisms for the Sandia flame CHNa and the Sydney Flame HM1E, respectively.

The Favre-average of a scalar ϕ can be defined from the PDF of f and χ as

$$\tilde{\phi} = \int\int \phi p\left(f,\chi\right) df\ d\chi, \tag{39}$$

where ϕ represents species mass fraction and temperature.

Using Bayes' theorem the joint PDF of f and χ can be written [42]

$$\tilde{p}\left(f,\chi\right) = \widetilde{p_f}\left(f\right)\widetilde{p_\chi}\left(\chi|f\right), \tag{40}$$

where $\widetilde{p_f}\left(f\right)$ is the marginal distribution

$$\widetilde{p_f}\left(f\right) = \int_0^\infty \widetilde{p_{f_\chi}}\left(f,\chi\right) d\chi \tag{41}$$

and $\widetilde{p_\chi}\left(\chi|f\right)$ is the conditioned PDF of χ for a fixed value of f. Here, the PDF's are specified by tilde as Favre-probability-density functions. Furthermore, f and χ are assumed to be statistically independent [1], [42] so the joint PDF $\tilde{p}\left(f,\chi\right)$ can be simplified as

$$\tilde{p}\left(f,\chi\right) = \widetilde{p_f}\left(f\right)\widetilde{p_\chi}\left(\chi\right), \tag{42}$$

where

$$\widetilde{p_\chi}\left(\chi\right) = \int_0^1 \widetilde{p_{f_\chi}}\left(f,\chi\right) d\chi \tag{43}$$

is the marginal distribution.

Eqs. 24-25 are solved to specify p_f which is supposed to have the β-PDF shape. The PDF of χ is the Delta function assuming that fluctuations are neglected.

The mean scalar dissipation, $\tilde{\chi}$, is modeled as [1], [42]

$$\tilde{\chi} = C_{\chi} \frac{\tilde{\epsilon} \widetilde{f''^2}}{\tilde{k}}, \tag{44}$$

where C_{χ} is a constant ($C_{\chi} = 2$), which may be expected to be valid in the fully turbulent part of shear flows.

For non-adiabatic steady state flamelets it is assumed that heat sources have a negligible effect on the species mass fractions. Then, temperature is calculated from Eq. 31.

2.6 Modeling radiation

The radiation is modeled by the P1-approximation, which is the simplest form of the more generalized P-N method (or spherical harmonics) [6] assuming that a flame is optically thin. The radiative heat loss $\bar{q}_r$ is calculated as

$$-\frac{\partial}{\partial x_j} \bar{q}_r = \alpha_c G - 4 e_c \sigma T^4, \tag{45}$$

where α_c is the absorption coefficient $\left(\mathrm{m}^{-1}\right)$, e_c is the emission coefficient $\left(\mathrm{m}^{-1}\right)$ and σ is the Stefan-Boltzmann constant. The incident radiation G is modeled according to

$$\frac{\partial}{\partial x_j} \left(\Gamma \frac{\partial}{\partial x_j} G \right) - \alpha_c G + 4 e_c \sigma T^4 = 0, \tag{46}$$

$$\Gamma = \frac{1}{3 \left(\alpha_c + \sigma_s \right)}, \tag{47}$$

where σ_s is the scattering coefficient $\left(\sigma_s = 1 \ \mathrm{m}^{-1}\right)$. The absorption coefficient and the emission coefficient are calculated using a weighted-sum-of-gray-gases model (WSGGM) [22] as a function of local concentrations of CO_2 and H_2O, path-length and pressure. The emissivity weighting factors for CO_2 and H_2O are taken from Smith et al. [52].

3 Brief description of the numerical methodology

A main purpose of this work was to validate the Eddy Dissipation Concept implemented in the OpenFOAM (hereafter OF) toolbox [55]. However, to investigate the influence of the turbulence-combustion interaction modeling, the assumed β-PDF approach and the steady laminar flamelet model (SLF hereafter) were tested as well, using the ANSYS FLUENT (hereafter AF) technology [1].

The standard k-ϵ model [28] with wall functions (hereafter SKE) was used to close the Navier-Stokes equations. The k-ω Shear Stress Transport (hereafter SST) turbulence model [38],[39] was applied for the Sydney flame HM1E

to advance modeling of this separated bluff-body flow. However, critical remark should be done here due to different implementations of the k-ω SST model in OF and AF. The high-Reynolds-number formulation of the k-ω SST [39] is implemented in OF assuming that the wall functions are specified for ω. In this case one should not expect superior results in predictions over the standard k-ϵ model (see Section 5.3). Both, the low-Reynolds-number and the high-Reynolds number formulations are available in AF through the enhanced wall treatment [1]. In the present study, the low-Reynolds-number SST model was assumed for the AF runs.

It is worth noticing that the same grids were used for both solvers.

3.1 OpenFOAM

The new solver was implemented by modification of the build-in OpenFOAM [55] application rhoPisoFoam for the compressible URANS modeling based on the finite-volume (FVM) method [16] and the PISO (pressure implicit with splitting of operators) algorithm [24]. The preconditioned (bi-) conjugate gradient method [19] with an incomplete-Cholesky preconditioner (ICCG) by Jacobs [25] was used for solving the system of linear algebraic equations with a local accuracy of 10^{-9} for all dependent variables at each time step. The numerical method had a second-order accuracy in space and time. The linear-upwind interpolation scheme (the 'second-order upwind' scheme [54]), was applied for all convective terms approximations. A second-order central differences approximation was used to calculate the diffusion terms. A second-order implicit Euler method (BDF-2 [16]) was used for the time integration together with a dynamic adjustable time stepping technique to guarantee a local Courant number less than 0.4.

The calculation of the mean species reaction rate $\bar{\omega}_s$ requires the integration of Eq.21 for each computational cell in the domain. For this purpose, the robust RADAU5 algorithm [18] was used. The RADAU5 algorithm is designed for the solving stiff ODE systems and applies a 5th-order accurate implicit Runge-Kutta method based on the Radau quadrature formula. The relative tolerance, absolute tolerance and maximum number of iterations to meet the target accuracy were set to 5×10^{-5}, 1×10^{-5} and 10^7, respectively.

3.2 ANSYS FLUENT

Using the factorized FVM [1] the URANS equations were solved with a second-order accuracy in space and time. The velocity and pressure fields were matched with a centered computational template based on the SIMPLEC algorithm [58] and Rhie and Chou filtering [49]. The convective terms were represented according to the Leonard quadratic upwind scheme (QUICK) [29], [54]. The linear system of equations was solved with the Gauss–Seidel iterations or the

incomplete lower upper (ILU) decomposition smoothers, which were accelerated by an algebraic multi-grid (AMG) technique, based on the additive-correction strategy [23]. A second-order implicit dual-step method was used for time integration with a constant time step of 10^{-5} s.

4 Description of test cases

4.1 Sandia Flame CHNa

The turbulent non-premixed syngas 40%CO/30%H_2/30%N_2 (by volume) flame investigated experimentally by Sandia National Laboratories (scalar measurements) and the Swiss Federal Institute of Technology (LDA measurements) [3] was examined. The burner tube had an inner diameter $D = 4.58 \times 10^{-3}$ m and an outer diameter of 6.34×10^{-3} m. The tube had a thickness of only 0.88×10^{-3} m. However, this was sufficient for flame stabilization via a small recirculation zone. The fuel jet Reynolds number was $\mathrm{Re}_j = U_j D/\nu_j = 16.7 \times 10^3$, where $U_j = 76$ m/s was the fuel jet velocity and $\nu_j = 2.083 \times 10^{-5}$ m^2/s was the kinematic viscosity. The jet temperature was 292 K. The co-flow stream had a velocity of 0.7 m/s, a temperature of 290 K and a 1.2% mole fraction of water vapor. Experimental data include axial and radial profiles of mean and root-mean-square (rms) values of temperatures and major species mass fractions as well as velocities and Reynolds stresses.

Some details of the grid and computational domain are shown in Fig. 1. The axial and radial dimensions of the computational domain after the burner exit were set to 0.6 m ($131 \times D$) and 0.2 m ($43.627 \times D$), respectively. The number of computational cells along the axial direction was 230 and the number of cells in the radial direction was 100. The length of the pre-inlet fuel pipe was 0.05 m ($10.917 \times D$) and contained 90 cells. The grid expansion factors were 1.09 and 1.14 in the axial and radial directions (from the burner tube), respectively. There were 10 cells along the inner radius of the fuel jet and 4 cells along the burner tube wall with uniform distribution in the radial direction.

Several studies of the CHNa flame are available in the literature. Cuoci et al. [8] have modeled numerically the CHNa and CHNb flames using RANS with several different turbulence-chemistry interaction approaches, such as the Eddy Dissipation Concept [33],[15] and the steady laminar flamelets model [12]. They reported that the EDC (coupled with the FFR kinetic mechanism) provided the best results.

In contrast to Cuoci et al. [8], Marzouk and Huckaby [36] have studied the CHNa flame using the URANS approach and adopted the Chalmers' partially stirred reactor model (PASR) [50] for the turbulence-chemistry interaction and investigated eight chemical kinetic mechanisms (including the FFR model). However, Marzouk and Huckaby obtained the most accurate predictions with a simple 3-step/5-species kinetic model.

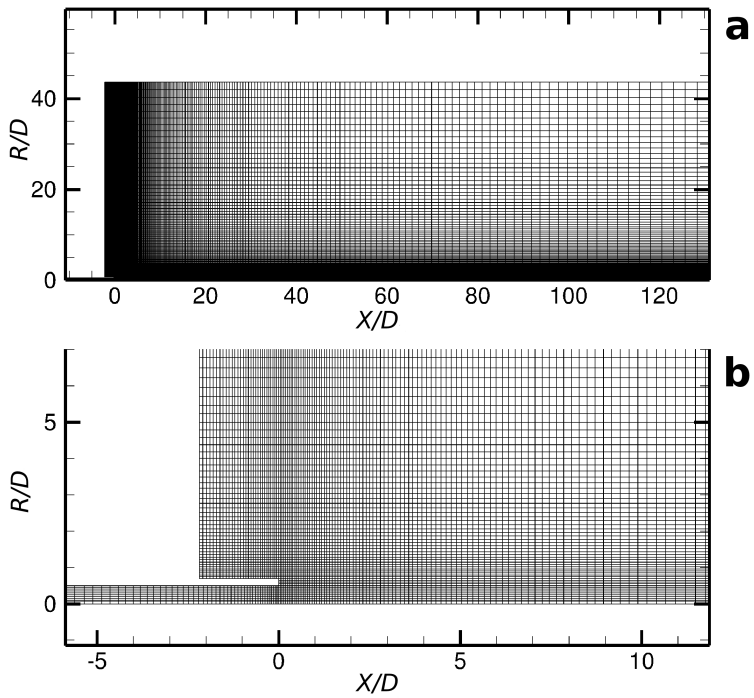

Fig. 1 A general view of the computational domain (a) and details of the grid near the inlet (b) for the Sandia CHNa flame. X and R are the domain coordinates in the axial and radial direction, respectively

4.2 Sydney Bluff-Body Flame HM1E

The Sydney bluff-body Flame HM1E configuration consisted of a rotationally symmetric bluff-body nozzle (with the diameter $D_B = 0.05$ m and the radius $R_B = D_B/2$) which was placed in a square duct of 0.13 m width. Gas was fed through a centered pipe (diameter of 3.6×10^{-3} m) at a bulk jet velocity of $U_j = 108$ m/s at ambient conditions with the jet Reynolds number, $\mathrm{Re}_j = 15.8 \times 10^3$. The fuel in this flame was a mixture of hydrogen (H_2) and natural gas in the volume ratio 1 : 1. The secondary air stream between the duct and the burner nozzle was fixed at 35 m/s. All velocities and velocity fluctuations were measured by Laser Doppler Velocimetry (LDV), and scalar measurements were carried out using the Raman/Rayleigh/LIF techniques [9].

Some details of the grid and computational domain are shown in Fig. 2. The axial and radial dimensions of the computational domain after the bluff-body were set to 0.5 m ($20 \times D_B$) and 0.15 m ($6 \times D_B$), respectively. The number of cells along the axial direction was 170, and the number of cells in the radial direction was 120. The grid expansion factors were 1.1 and 1.12 in the axial and radial directions (from the bluff-body), respectively. The length of the

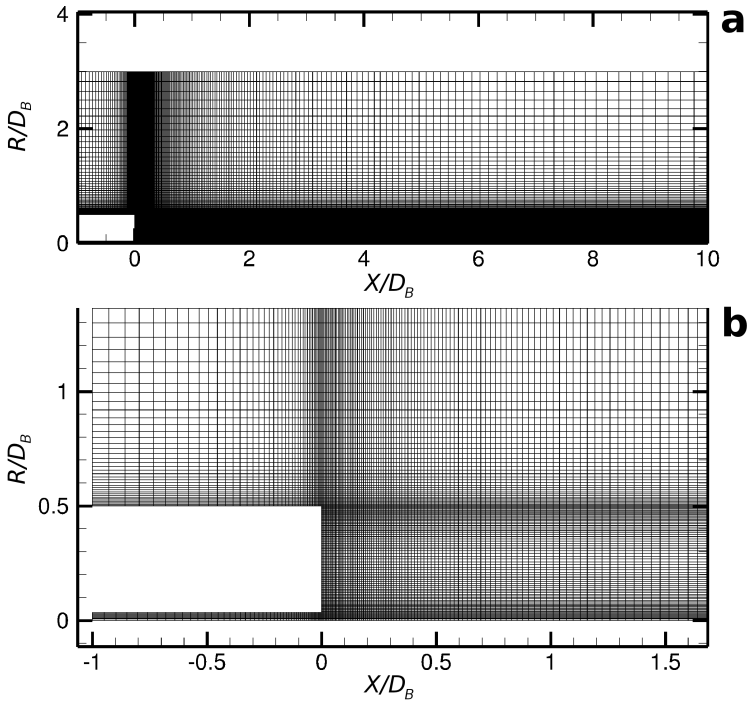

Fig. 2 General view of the computational domain (a) and details of the grid near the inlet (b) for the Sydney bluff-body HM1E flame. X and R are the domain coordinates in the axial and radial direction, respectively

pre-inlets for the fuel pipe and co-flow was 0.05 m ($2 \times D_B$) and contained 50 cells. The number of computational cells (in the radial direction) located in the jet, bluff-body and co-flow was 8, 60 and 52, respectively. The inner radius of the fuel jet had a uniform distribution of cells in the radial direction, while the bluff-body had bi-exponentiation distribution of nodes from the mid to the fuel jet and co-flow.

Several researchers have performed simulations of the Sydney bluff-body flames with different turbulence and combustion models. Liu et al. [31] provides a comprehensive overview of previous work. However, it is worth noticing that there is a lack of published data related to the use of the EDC coupled with the detailed chemistry approach.

4.3 Boundary conditions

All problems were solved assuming symmetry about the centerline. For all cases, a computational domain was designed as a sector of 5° with imposed periodic boundary conditions and included pre-inlet pipes for the fuel-jet in

order to obtain fully-developed turbulent velocity profiles. Uniform velocity profiles were specified for jets and co-flows streams. All radial and circumferential velocity components were set to be zero. The inflow temperatures were set based on the experimental settings. A zero gradient pressure boundary was applied for all inflow boundaries, while the exit pressure was specified to 10^5 Pa at the outlet. A non-slipping condition for velocity was applied to the walls. The temperature at the walls was fixed (iso-thermal) and set according to the experimental data. Wall-functions were applied for $\tilde{k}$, $\tilde{\epsilon}$ and $\tilde{\omega}$ (for OF). The enhanced wall treatment was used for ω for AF. The inlet values for $\tilde{k}$ and $\tilde{\epsilon}$ ($\tilde{\omega}$) were calculated for a turbulence intensity taken as 5%, and the turbulence length scale estimated as 7% of the inlet diameters. The fuel jet, pilot and co-flow compositions were specified in terms of the species mass fractions calculated from the experimental data. Zero-gradient diffusion boundary conditions was applied for species at the walls. Marshak's boundary conditions, based on solutions of Legendre polynomials of odd order [35], were adopted for radiative heat flux calculations.

4.4 Grid dependence study

The present EDC-based results (calculated by OF) were obtained using two sets of grids for each of the flames: a low-resolution grid and a high resolution grid. The high-resolution grids were created by simple refinement of the low-resolution grids by a factor of 2×2 in the axial and radial directions. The details of the high-resolution grids are provided in the Sections 4.1 and 4.2. In general, the differences between the two sets of grids were insignificant for the mean velocities, temperature and main species such as O_2, N_2, CO_2, H_2O and H_2. However, for the intermediate species such as CO, OH and NO, high-resolution grids provide more accurate results. Therefore, the EDC-based and the PDF-based results discussed below were obtained using the high-resolution grids. Further grid refinement was not carried out due to resource limitations.

5 Results

5.1 Present predictions

All simulated cases are listed in Table 1 (where the following abbreviations are used: F – flame CHNa or HM1E, C – code OF or AF, TM – turbulence model, TCM – turbulence-chemistry interaction model, CH – chemistry mechanism and R – radiation model).

For a quantitative validation of the present simulations the averages have been obtained from the computational results by sampling over four flow-through times, where the flow-through time is defined as the ratio between the axial length of the computational domain to the jet bulk velocity. Hereafter, the time-averaging operator is denoted by $\langle\rangle$. The tilde mark denoting Favre-averaging is omitted for the simplicity.

Table 1 Run matrix

Run	C	F	TM	TCM	CH	R
EDC-FFR	OF	CHNa	SKE	EDC	FFR	P1
EDC-GRI3	OF	CHNa	SKE	EDC	GRI3.0	P1
EDC-GRI3-noRad	OF	CHNa	SKE	EDC	GRI3.0	–
β-PDF	AF	CHNa	SKE	β-PDF	–	P1
β-PDF-$C_{\epsilon 1} = 1.52$	AF	CHNa	SKE ($C_{\epsilon 1} = 1.52$)	β-PDF	–	P1
β-PDF-$C_{\epsilon 1} = 1.60$	AF	CHNa	SKE ($C_{\epsilon 1} = 1.60$)	β-PDF	–	P1
SLF-FFR-$C_{\epsilon 1} = 1.52$	AF	CHNa	SKE ($C_{\epsilon 1} = 1.52$)	SLF	FFR	P1
EDC-GRI3-SKE	OF	HM1E	SKE	EDC	GRI3.0	P1
EDC-GRI3-SST	OF	HM1E	SST	EDC	GRI3.0	P1
SLF-GRI3-SST	AF	HM1E	SST	SLF	GRI3.0	P1
SLF-GRI3-SST-$\mathrm{Sc}_t = 0.4$	AF	HM1E	SST	SLF ($\mathrm{Sc}_t = 0.4$)	GRI3.0	P1

5.2 Sandia Flame CHNa

Fig. 3a qualitatively compares the mean axial velocities and the mean temperature along the central axis obtained by OF with the EDC model (run EDC-FFR) with the results by Marzouk and Huckaby [36], who used the Chalmers' PASR model [7], [50] with the FFR mechanism. Both results were carried out using OF. However, remark is necessary, since Marzouk and Huckaby [36] applied the standard k-ϵ model with the modified constant $C_{\epsilon 1} = 1.6$. On the one hand, one can clearly see that the predictions with the modified constant $C_{\epsilon 1} = 1.6$ led to the more accurate behavior of the jet penetration. On the other hand, the axial distribution of the flame temperature was significantly over-estimated, especially in the post-flame zone.

The same observation was found by Cuici et al. [8] in their results obtained by the steady laminar flamelet model [44] coupled with SKE and $C_{\epsilon 1} = 1.6$. Further, several additional runs were performed to investigate the effect of the constant $C_{\epsilon 1}$ using AF with the β-PDF approach. Fig. 3b shows the predicted mean axial velocities and the mean temperature along the central axis using SKE with $C_{\epsilon 1} = 1.44$, $C_{\epsilon 1} = 1.52$ and $C_{\epsilon 1} = 1.6$, respectively. It could be observed that the higher values of $C_{\epsilon 1}$ compared to the baseline value of 1.44 led to a more accurate prediction of the mean axial velocity distributions. The present results showed that while the location of the peak temperature is shifted downstream with an increased value of $C_{\epsilon 1}$, the post-flame zone became over-estimated. Thus, the compromise value $C_{\epsilon 1} = 1.52$ may probably be the best choice for the prediction of the Sandia flame CHNa using AF with the assumed β-PDF approach.

Fig. 4 compares the profiles of the mean temperature and species mass fractions with the experimental data along the central axis for the several runs. In general, the match between numerical and measured results was satisfactory. One can observe some discrepancies for the peak temperatures between the measured and calculated results. A comparison of the predicted flame temperatures is also displayed in Fig. 5. The maximum peak temperature ($\langle T_p \rangle = 2276$ K) was obtained by the EDC run with the GRI3.0 chemistry where no radiation heat transfer was considered. The minimum measured peak

temperature was obtained in the experiments ($\langle T_p \rangle = 1919$ K). The closest to the experimental values $\langle T_p \rangle = 1978$ K and $\langle T_p \rangle = 1971$ K were predicted by the β-PDF approach and the SLF model, respectively. The other two runs with the EDC, the P-1 radiation and the FFR and the GRI3.0 chemistry revealed approximately the same peak values $\langle T_p \rangle = 2160$ K and $\langle T_p \rangle = 2146$ K, respectively.

Another interesting observation following from Figs. 4 and 5 was the different location of peak temperatures predicted by the applied combustion models. The location of $\langle T_p \rangle$ obtained by the assumed β-PDF approach was slightly shifted upstream ($\approx 6X/D$) compared to the experimental data, while the EDC-based models predicted the location of $\langle T_p \rangle$ correctly. The SLF model with the corrected constant $C_{\epsilon 1} = 1.52$ predicted the peak temperature location quite well.

It is evident as well, that any model overestimation of the flame temperature affect the prediction of the species. The EDC-based models over-estimated the peak temperature by approximately 250 K, hence releasing more thermal energy and producing too high $\langle Y_{H2O} \rangle$ and $\langle Y_{CO2} \rangle$. However, all other species such as $\langle Y_{N2} \rangle$, $\langle Y_{O2} \rangle$, $\langle Y_{H2} \rangle$ and $\langle Y_{CO} \rangle$ matched well the experimental results. It it worth noticing that only the EDC with the FFR scheme was able to reproduce correctly the behavior of $\langle Y_{OH} \rangle$.

An over-prediction of flame temperature may have several reasons. According to Hewson and Kerstein [20], neglecting the radiative heat losses and under-predicting the dissipation rate could be responsible for temperature over-predictions ($59 - 241$ K). Cuoci et al. [8] reported that thermal radiation affects the peak temperature only by about $30 - 40$ K. However, the present results indicated a more significant impact of the thermal radiation on the solution (about 130 K).

Furthermore, Cuoci et al. [8] investigated in detail the effect of the grid density and the applied numerical schemes and concluded that the peak temperature was nearly insensitive to these factors. Cuoci et al. [8] suggested that the most important factor was the turbulence model used. Indeed, different turbulence models affect the jet penetration and the scalar dissipation rate and turbulent mixing.

Furthermore, it is interesting to compare the predicted mean axial velocities with the experimental data (Fig. 6). It is observed that the present results under-estimated to some extent the jet velocity down-stream the central axis. The divergence between predictions by SLM and EDC was not significant. The discrepancies between the SLM model and the measured data could possibly be explained by the compressibility effects. Hewson and Kerstein [20] carried out a detailed investigation of such phenomena and suggested that the dilatation of the flow was a possible explanation for these discrepancies. According to Hewson and Kerstein [20] dilatation pushes the fluid downstream leading to higher mixture fractions on the axis and affecting the dissipation rate. Subsequently, increased dissipation rates cause more rapid mixing and a greater rate of decay of the axis mixture fraction. The radial profiles of the mean axial velocities at the axial distances $X/D = 20$ and $X/D = 40$ further mimicked

the behavior of the axial distributions. At $X/D = 20$ the predicted jet spreading matched well the measured data when using OF with the EDC approach and AF with the SLM model. Based on the comparison of the predicted and measured radial profiles of the mean axial velocity at $X/D = 40$ downstream the nozzle exit, it was evident that the both OF with the EDC and AF with the SLM model significantly over-estimated the decay of the jet by $\sim 15\%$.

A detailed comparison of the radial profiles of the mean temperature and the mean composition at the axial distances $X/D = 20$ and $X/D = 40$ is presented in Figs. 7 and 8, respectively. In general, the agreement between the predicted and the measured data was reasonable. The existing discrepancies may be explained by the behavior of the predicted velocity field, e.g. jet penetration and spreading/diffusion.

Fig. 9 shows scatter plots of the temperature as a function of mixture fraction by the experiment and the SLM model at the axial distances $X/D = 20$ and $X/D = 40$. The experimental conditional mean of the temperature is shown in Fig. 9 as well. Overall, the agreement between calculations and the experiment was good. One can observe that the maximum temperature at both locations was slightly over-predicted. The match between the predicted and conditional mean temperatures was good up to $\langle f \rangle = 0.6$ and $\langle f \rangle = 0.26$ at $X/D = 20$ and $X/D = 40$, respectively.

In general, the predicted results by OF with the EDC-based approach and AF with the SLM model (and corrected $C_{\epsilon 1}$ constant) matched well the experimental data. On the one hand, the deviations related with the EDC-based approach could be explained as the consequence of using a not corrected k-ϵ model. On the other hand, the effect of dilatation could be considered as the most important for the SLM model (and the β-PDF approach).

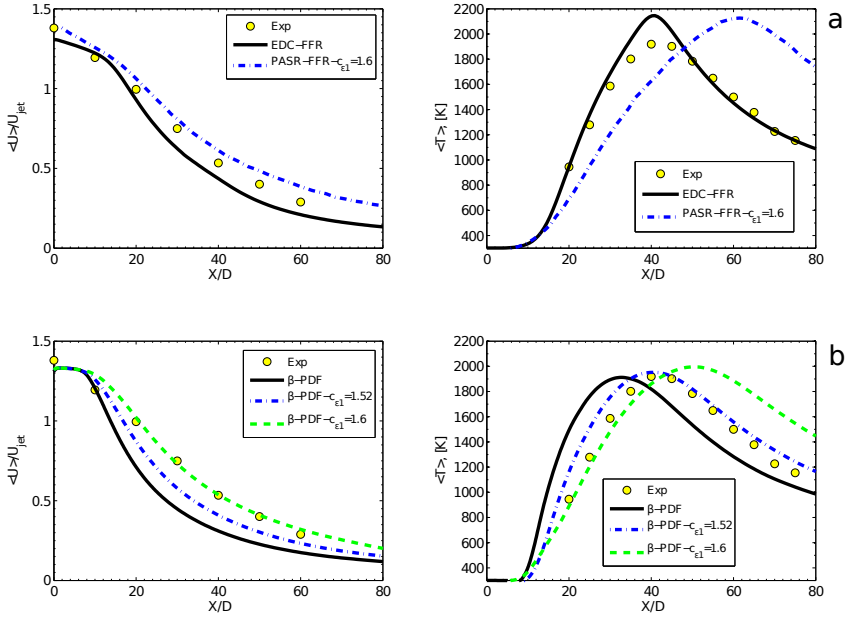

Fig. 3 Comparison of the predictions by the EDC-FFR and the PASR-FFR (extracted from [36]) models of the Sandia Flame CHNa (a). Effect of the $C_{\epsilon 1}$ constant in the standard k-ϵ model on the Sandia flame CHNa predictions using the assumed β-PDF approach (b)

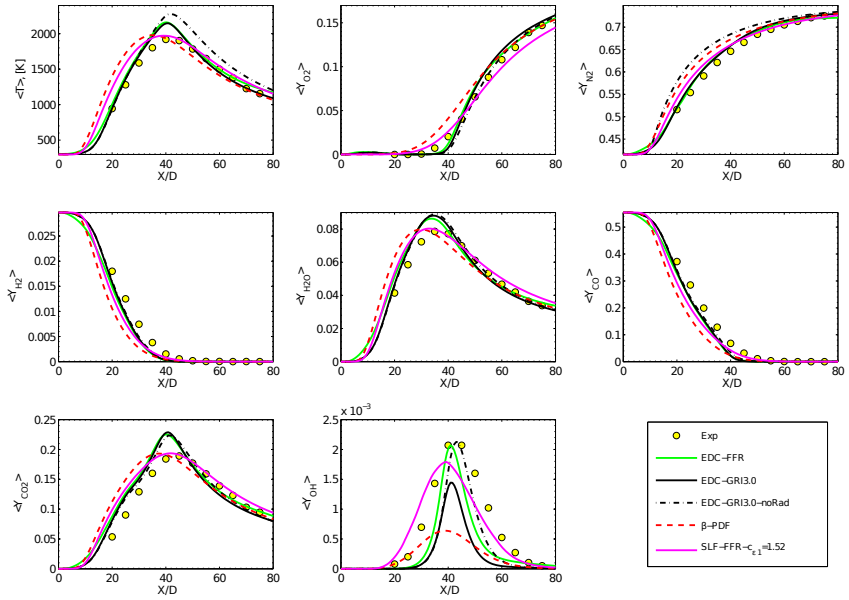

Fig. 4 Mean temperature and mean composition profiles along the axis for the Sandia flame CHNa

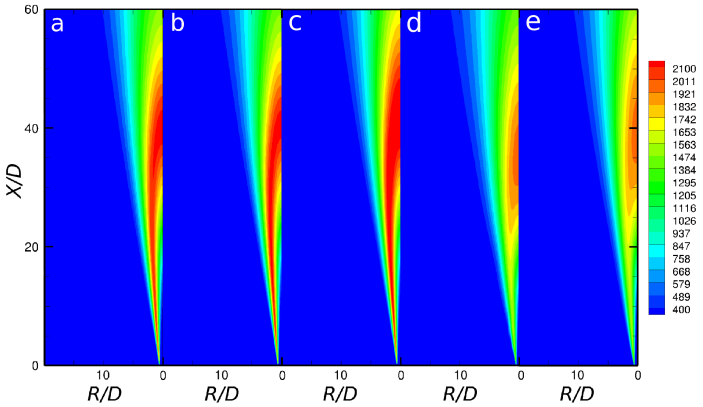

Fig. 5 Iso-contours of mean temperature for the Sandia flame CHNa: EDC-FFR (a), EDC-GRI3 (b), EDC-GRI3-noRad (c), β-PDF (d) and SLF-FFR-$C_{\epsilon 1} = 1.52$ (e)

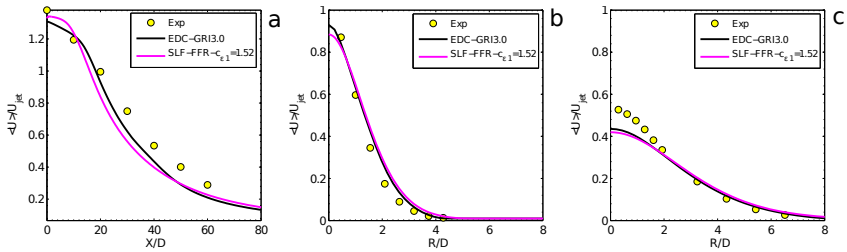

Fig. 6 Mean axial velocity along the axis (a) and at axial positions $X/D = 20$ (b) and $X/D = 40$ (c) for the Sandia flame CHNa

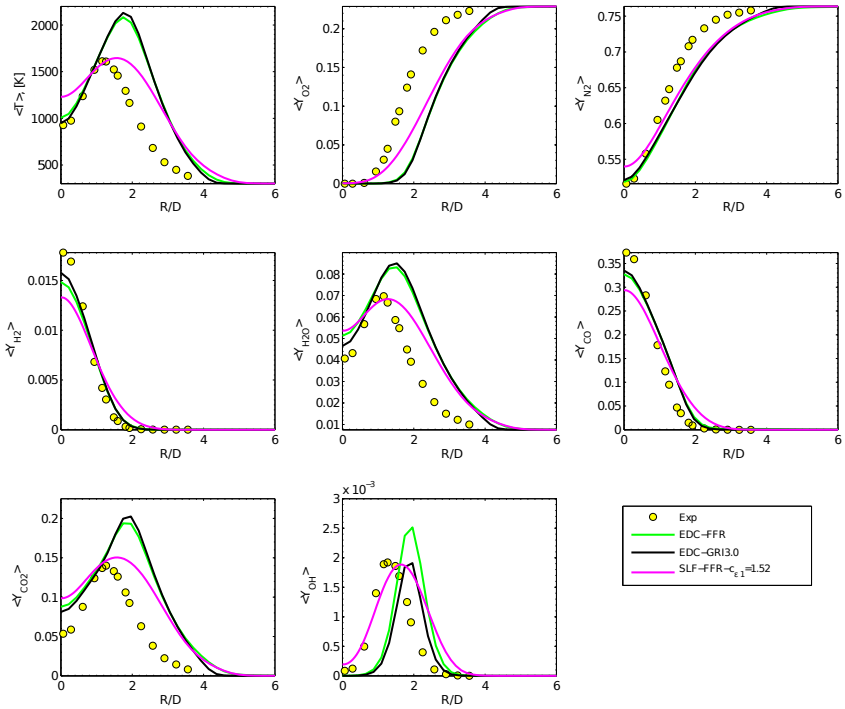

Fig. 7 Mean temperature and mean composition radial profiles at $X/D = 20$ for the Sandia flame CHNa

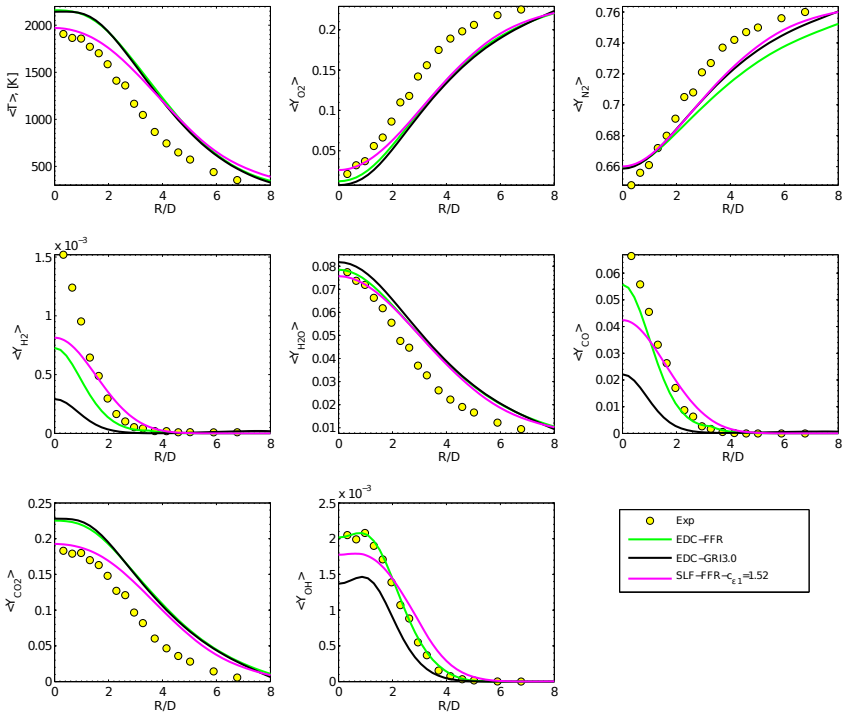

Fig. 8 Mean temperature and mean composition radial profiles at $X/D = 40$ for the Sandia flame CHNa

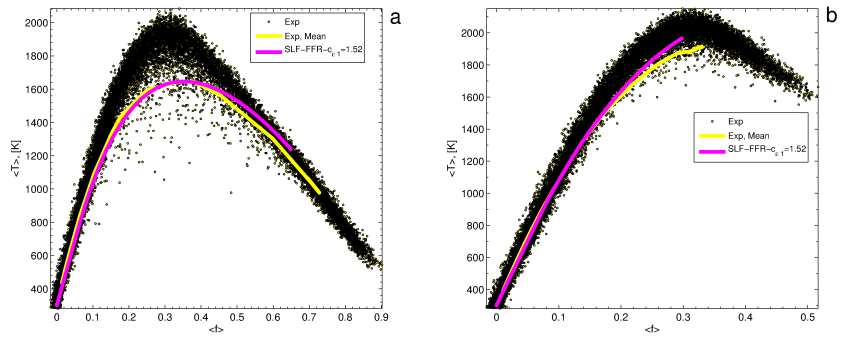

Fig. 9 Scatterplots of temperature against mixture fraction for the Sandia flame CHNa at $X/D = 20$ (a) and $X/D = 40(b)$

5.3 Sydney bluff-body flame HM1E

Predicted radial profiles of the mean velocities for the Sydney flame HM1E were compared to experimental data in Fig. 10. Overall, the agreement between the present data and the measurements was good at upstream locations within the recirculation zone. Both the shape and the peak values of the radial profiles of the mean axial $\langle U \rangle$ and radial $\langle V \rangle$ velocities were well captured in this region. The jet penetration depth, the spreading and the positions of the two shear layers were predicted quite well. It is interesting to note that the axial velocities predicted by OF with the SKE and SST turbulence models decayed too quickly at the symmetry axis compared to the experimental data. This was in agreement with the predictions by Yan et al. [57] and Liu et al. [31]. In spite of that the magnitudes of mean radial velocities were significantly smaller than the magnitudes of the mean axial velocities (approximately by one order of magnitude), the agreement between them was reasonable.

As expected the deviations between OF runs with SKE and SST for the velocity field within recirculation zone were minimum. The manner of implementation of the SST model in OF (via wall functions) was the main reason here. In general, the agreement between the measured data and AF with the low-Reynolds-number SST model was more accurate compared to the OF runs.

The predicted streamline pattern is shown in Fig. 11. The flame was stabilized by the recirculation zone behind the bluff-body which traps hot gases. By definition, the recirculation length ($\langle L_r \rangle$) corresponds to the distance between the base of the bluff-body and the sign change of the centerline mean axial velocity. The calculated recirculation zone length was in a range of $1.19-1.22D_B$ which was consistent with the predictions by Yan et al. [57]. Precise experimental data for $\langle L_r \rangle$ were not available, however its value could be bounded between $X/D = 1.4$ and $X/D = 1.8$. Hence, $\langle L_r \rangle$ was under-predicted in the present calculations.

Iso-contours of mean temperature and $\langle Y_{OH} \rangle$ inside the recirculation zone are displayed in Fig. 12. Figs. 13 and 14 compare time-averaged scalar fields at two axial locations inside the recirculation zone. A comparison of the predicted and measured mean temperature and other species outside the recirculation zone is displayed in Fig. 15.

In general, temperature profiles predicted by OF with the EDC-based approach matched the experimental data well. The peak in the predicted temperature profiles in the shear layer between the co-flow and the hot combustion products at $X/D_B = 0.6$ may be explained by the artificial boundary condition for the temperature set at the bluff-body walls. The fixed constant temperature was applied at the outer surface of the bluff-body ($T = 953$ K), which appears to lead to an inaccurate estimate of the heat transfer and consequently an over-prediction (approximately 200 K) of the temperature in the shear layer. Another feature that can contribute was the unburned fuel recirculated by the outer reversed zone which can partly burn when mixed with the fresh air, leading to some temperature increase. Figs. 13-14 show that there was more H_2 and CO than in the experiment at the locations of the negative axial ve-

locity. Other possible reasons such as insufficient boundary layer and shear layer resolutions and the simple treatment of radiation heat transfer should be considered as well.

Further downstream a good match between calculated by OF with the EDC-based approach and measured data for the temperature was observed. The radial profiles of $\langle Y_{O2} \rangle$, $\langle Y_{N2} \rangle$, $\langle Y_{H2} \rangle$, $\langle Y_{CO2} \rangle$ and $\langle Y_{H2O} \rangle$ matched the experimental data well. The profiles of $\langle Y_{CO} \rangle$ were slightly over-predicted. These discrepancies could be explained by the temperature behavior in the shear layer. Prediction of OH in any combustion simulation is particularly challenging due to the strong nonlinearity of the species evolution [47]. The agreement for $\langle Y_{OH} \rangle$ was very satisfactory which could indicate that the combustion process was represented correctly. The reaction took place in the mixing shear layer between the co-flow stream and the recirculation zone. The profiles of $\langle Y_{NO} \rangle$ was over-predicted significantly showing only the correct trends. The production of NO is highly dependent on temperature. Thus, one of the possible reasons for such discrepancies may be the incorrect treatment of radiation which can have a dramatic effect on the predicted NO levels [13].

The match between the predicted results by AF with the SLF model was less accurate. The SLF model failed to capture peak temperature at $X/D_B = 0.9$. At $X/D_B = 1.3$ the SLF model failed to represent the experimental profile. However, these results were consistent with the published data by Yan et al. [57] who used the SLF model as well. The radial profiles of $\langle Y_{O2} \rangle$, $\langle Y_{N2} \rangle$, $\langle Y_{H2} \rangle$, $\langle Y_{CO2} \rangle$ and $\langle Y_{H2O} \rangle$ had the similar trend to those of mean temperature. OH and NO were not well reproduced by AF with the SLF model as well.

Fig. 16 displays profiles of conditional mean for temperature, which probably could provide a more quantitative test than scatter plots [40]. The temperature profiles matched well at $X/D_B = 0.6$ location. Further downstream the calculated profiles of temperature failed to reproduce the peak values and in general are significantly lower than the experimental data. The calculated mixture fraction reached too lean values as well.

In the recirculation zone, with strong radial gradients of mean velocity and mean mixture fraction, it was observed a lack of turbulent diffusion. This finding was contrast the fact that the velocity field within the recirculation region was predicted quite accurately. Thus, there was some 'degree of freedom' of playing with the PDF turbulence Schmidt number (here, $\mathrm{Sc}_t = 0.85$) to improve the results [41]. With this goal, another run with AF and the SLM model was conducted where the PDF Schmidt number was set to $\mathrm{Sc}_t = 0.4$. The predicted results revealed a minimum impact on the flow field, except the small deviations in the distributions of the radial velocity (Fig. 10) and as a consequence on the streamline pattern (Fig. 11). Meanwhile, the predicted mean composition was improved significantly within the recirculation zone. However, the peak temperature at $X/D_B = 0.9$ was not captured well. Moreover, the large deviations were observed between the predicted and the experimental temperatures at the central axis at $X/D_B = 0.9$ and $X/D_B = 1.3$. In general, OH was calculated more accurately compared to the case with $\mathrm{Sc}_t = 0.85$. The

profiles of NO were over-predicted as well and, in general, were less accurate than for the case with $\mathrm{Sc}_t = 0.85$.

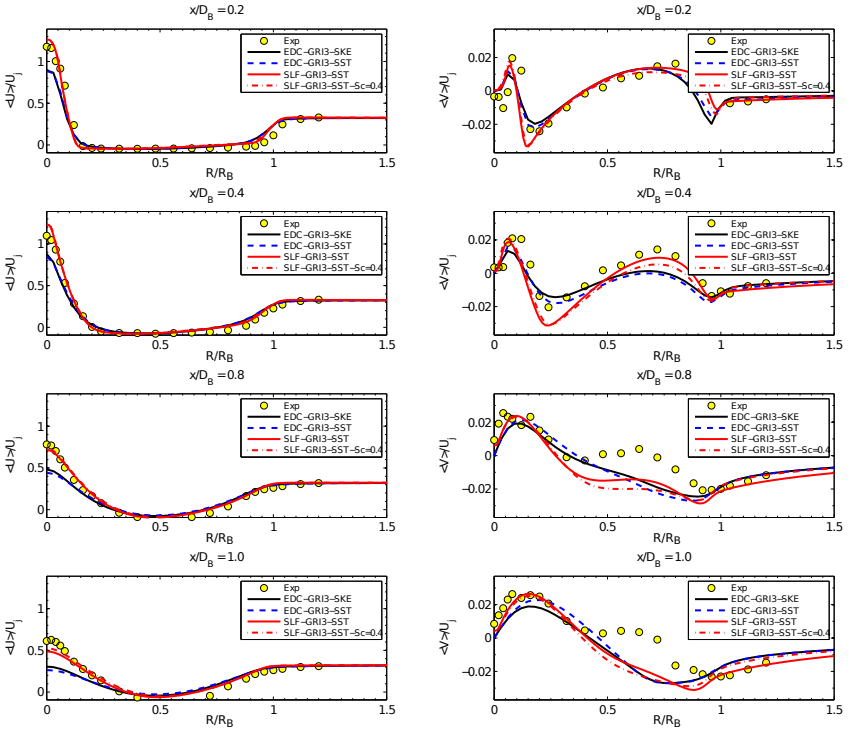

Fig. 10 Radial profiles of the mean axial and radial velocities at different axial positions for the Sydney flame HM1E

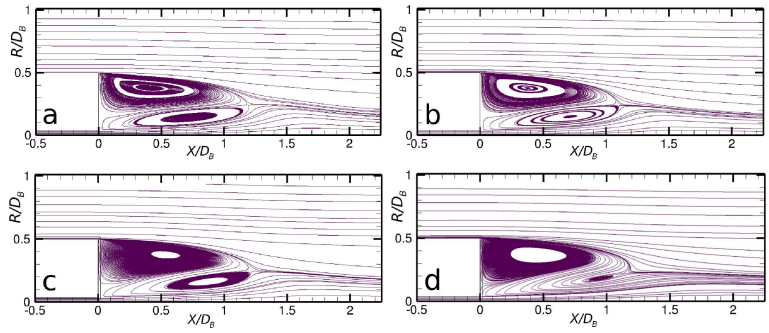

Fig. 11 Time-averaged streamlines for the Sydney flame HM1E: EDC-GRI3-SKE (a), EDC-GRI3-SST (b), SLF-GRI3-SST (c) and SLF-GRI3-SST-$Sc_t = 0.4$ (d)

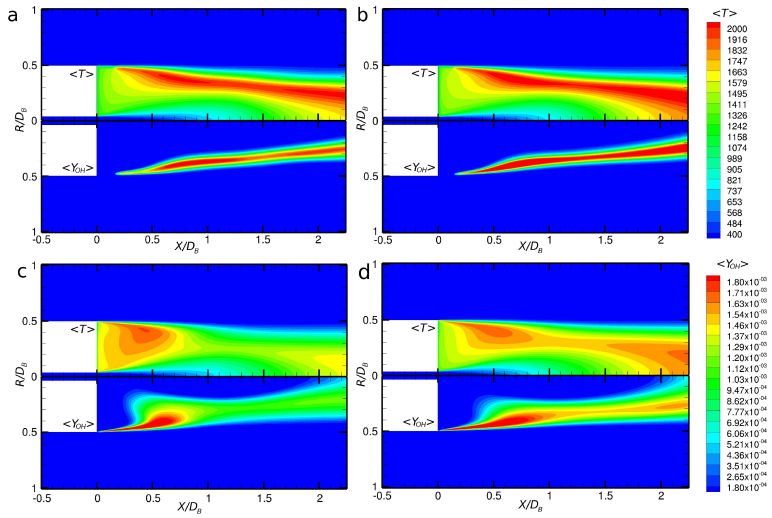

Fig. 12 Iso-contours of mean temperature and OH mass fractions for the Sydney flame HM1E: EDC-GRI3-SKE (a), EDC-GRI3-SST (b), SLF-GRI3-SST (c) and SLF-GRI3-SST-$Sc_t = 0.4$ (d)

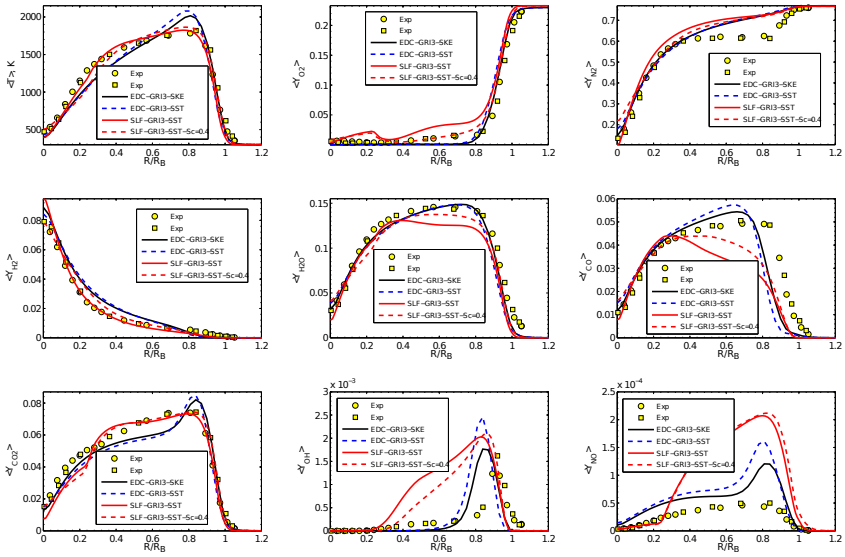

Fig. 13 Radial profiles of mean temperature and mean composition at $X/D_B = 0.6$ for the Sydney flame HM1E. Experiments [9] are for both sides of the symmetry axis

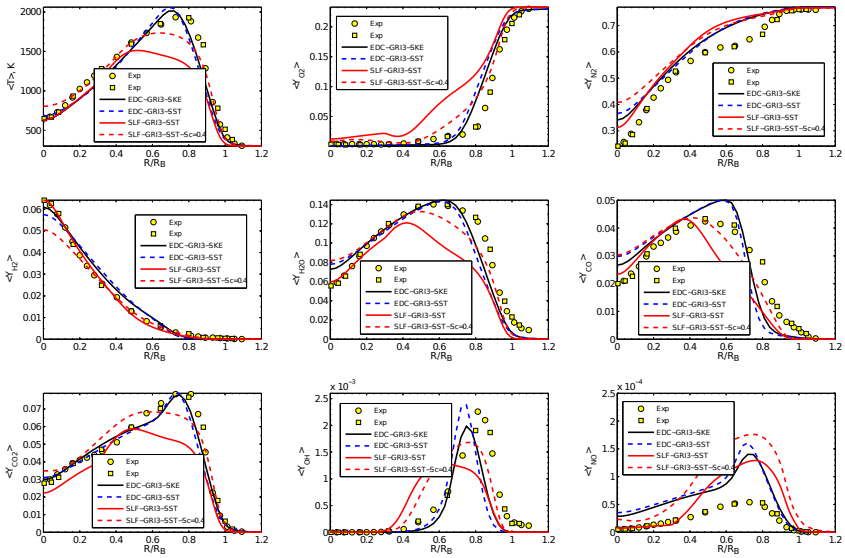

Fig. 14 Radial profiles of mean temperature and mean composition at $X/D_B = 0.9$ for the Sydney flame HM1E. Experiments [9] are for both sides of the symmetry axis

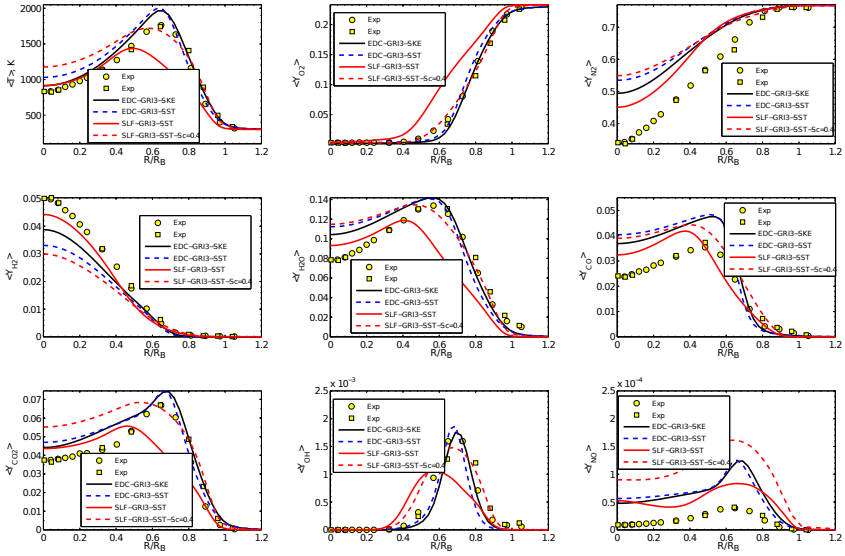

Fig. 15 Radial profiles of mean temperature and mean composition at $X/D_B = 1.3$ for the Sydney flame HM1E. Experiments [9] are for both sides of the symmetry axis

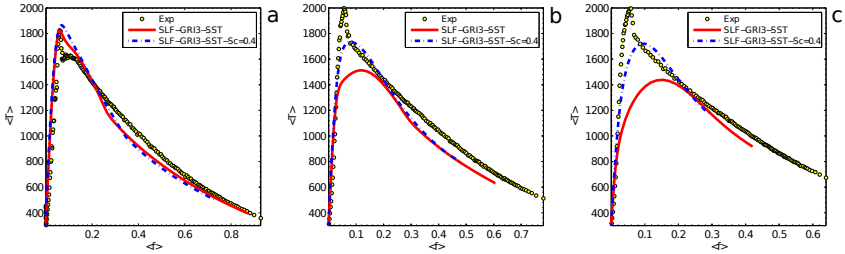

Fig. 16 Conditional temperature profiles for the Sydney flame HM1E at three axial locations $X/D_B = 0.6$ (a), $X/D_B = 0.9$ (b) and $X/D_B = 1.3$ (c)

6 Discussion

Numerical predictions of the Sandia Flame CHNa and the Sydney Flame HM1E have been carried out. In general, in spite of some discrepancies, good agreement was achieved for both flames in terms of velocity fields, temperature and the species concentrations.

The disagreement between experimental data and numerical results is determined by two groups of errors (apart from experimental errors): (1) 'model' errors due to inadequate assumptions made in selecting one sub-model or another (for turbulence, radiation and turbulence-chemistry interaction) and (2) 'discretization' errors caused by the inadequate resolution of the employed computational grids and computational methods. Whereas the errors of the first group are assumed to be 'systematic' under certain assumptions, e.g. for a fixed computational methodology, 'discretization' errors are controlled by the method of adaptation (increase in the resolution) of a computational grid.

6.1 Influence of modeling errors

From the 'model' error point of view the following critical remark should be done. Here, the turbulence-chemistry interaction was modeled using the EDC model with detailed chemistry, while the standard k-ϵ model and the P1-approximation model were used for the turbulence and radiation, respectively. Choosing appropriate models for turbulence, chemistry and radiation would play an important role for modeling of the turbulent reacting flows.

In the present study, the influence of the radiation heat transfer was investigated for the Sandia Flame CHNa using the EDC with the GRI3.0 chemistry. The predicted difference between peak temperatures was about 140 K. However, the results showed that discrepancies between major species were insignificant. Another aspect of radiation influence on temperature prediction is an accurate estimation of NO. The present calculations were not able to predict accurately the concentration of NO for both test cases. Thus, an application of alternative radiation sub-models could be of interest in future work.

The specially designed kinetic mechanism FFR [14] was applied to simulate syngas combustion of the Sandia Flame CHNa, which demonstrated satisfactory results compared to the experimental results. To check the influence of the chemical kinetics, the Sandia Flame CHNa was calculated using EDC with the full GRI3.0 mechanism [4], which revealed only minor differences for the major species and the temperature compared to the results with the FFR mechanism. This observation correlates well with the previous results by Lilleberg et al. [30] and Zahirović et al. [59]. The Sydney flame HM1E was predicted using only GRI3.0 scheme due to resource limitations. Moreover, it turned out that this flame was more computationally stiff (expensive) with respect to other chemistry, compared to the Sandia Flame CHNa.

The SLM model was applied to analyze the influence of turbulence-chemistry interaction sub-modeling. For the Sandia flame CHNa the agreement between the EDC-based approach, the SLF model and the measured data was reasonable. The results obtained by the PDF-based approaches revealed an upstream shift of the peak temperature and more rapid decay of the jet. Such discrepancies could possibly be explained by the incompressible flow nature of the PDF-based models with the related effect of the dilatation flow, which was investigated in detail by Hewson and Kerstein [20]. The EDC-based calculations showed the correct peak temperature location, but over-predicted the peak values approximately by 240 K and could be explained by the applied turbulence model.

For the Sydney flame HM1E, the EDC-based approach revealed more accurate results compared to the SLF model. It was found that such strong discrepancies between the measured data and the results by the SLF model are strongly related with the lack of the turbulence mixing due to the fixed PDF Schmidt number. Within, another run with the modified PDF Schmidt number $\mathrm{Sc}_t = 0.4$ was performed which indicated that the influence on the flow field was minor, while the composition was changed significantly but still not sufficient to match the experimental temperature at $X/D_B = 0.9$ and $X/D_B = 1.3$ well.

In the present study transport properties were simplified while using AF with the PDF-based approaches by neglecting the Dufour and Soret effect by introducing a single diffusion coefficient (i.e. the assumption of unity Lewis number) which may lead to considerable errors [42]. Another remark related with the PDF-based models is the assumption of statistical independence between the mixture fraction and the scalar dissipation which remains questionable and probably could not be accurate in turbulent mixing layers [42].

With respect to the turbulence modeling the following observations were found. The EDC-based approach with the standard k-ϵ model provided satisfactory results for the Sandia flame CHNa anb the Sydney flame HM1E flame. The SLM model provided most accurate predictions of the Sandia flame CHNa when the constant $C_{\epsilon 1}$ was set to $C_{\epsilon 1} = 1.52$. A change of the model constant $C_{\epsilon 1}$ value is a common remedy to reduce spreading/diffusion and increase the predictive capabilities of the model (e.g. [30]). However, as it was discussed in Section 5.2, the conventional modified value of $C_{\epsilon 1} = 1.6$ significantly over-predicted the flame temperature in the post-flame zone [8], [36] for the Sandia flame CHNa. Here it was found that the alternative value of $C_{\epsilon 1} = 1.52$ may be a compromise choice to simulate the Sandia flame CHNa using the PDF-based models.

For the Sydney flame HM1E, the SLM model with the low-Reynolds-number k-ω SST turbulence model predicted the flow field quite accurately inside the recirculation region, meanwhile temperature and the composition were predicted unsatisfactory. Furthermore, the Sydney flame HM1E was calculated using OF with the EDC-based approach coupled with the standard k-ϵ and the k-ω SST turbulence models and it was found that the discrepancies between these two cases were minor.

Another important aspect of combustion modeling is the radiative heat transfer. In the present study it was treated in a simple way using the P-1 approximation [6], assuming that a flame is optically thin. Sometimes, the optically thin radiation sub-model could not accurately predict the radiant fraction [13]. Thus, it will be interesting in future work to investigate these flames with more sophisticated radiation sub-model (like a Discrete Ordinate model [46]). It is worth noticing that unphysical results were obtained using the Discrete Ordinate model for temperature at the center axis for axisymmetrical test problems in the present study. These results were confirmed for both OpenFOAM and ANSYS FLUENT. Thus, the full three-dimensional simulations are required in order to get accurate predictions with the Discrete Ordinate model.

Furthermore, the finite-rate chemical kinetics were taken into account by treating the fine structures as constant pressure and adiabatic homogeneous reactors calculated using the Perfectly Stirred Reactor model [17]. Here the effect of radiation losses in the PSRs was neglected and more accurate formulation should be formulated and investigated in future work.

6.2 Influence of discretization errors

From the 'discretization' error point of view, two sets of grids were used in the present study to check the mesh-error influence. It is worth noticing that in spite of the fact that the calculations were carried out in two dimensions, approximately $3-5$ weeks were required to get statistically-converged solutions on the high-resolution grids using one node (16 cores in parallel) on the 'Vilje' high-performance computing facility (www.notur.no). The main reason for this was the finite-rate chemistry. This showed that turbulent flow simulations with the detailed chemistry were resource expensive even for two-dimensional problems. The present EDC-based calculations did not reveal significant deviations between the solutions obtained on the low-resolution (not presented here) and the high-resolution grids (except for the intermediate species, such as OH and NO). Thus, due to resource limitations, the resolution of the applied grids was concluded to be sufficient for the scope of the present work.

The influence of the 'temporal discretization' errors was not analyzed in the present study. Usually the spatial discretization error effect is larger than the error arising from the time integration [16]. It could be shown that in case of fully developed turbulent flows, existing small time and space scales are simply advected by the most energetic eddies [16]. This argument yields an accuracy time-scale similar to the Courant–Friedrichs–Lewy (CFL) criterion. Thus, in all present calculations, the stability condition $\mathrm{CFL} < 0.4$ was employed, which guaranteed that the actual time step was close to the accuracy time step.

Another important parameter is the error tolerance for chemistry system integration. This parameter influences the accuracy of the species predictions and the total computational time for each time step (iteration) as well. In the present study the absolute tolerance was set to 10^{-5} and no sensitivity

study was carried out. However, for the further method development it will be required to assess the influence of this parameter on the flow predictions both in terms of accuracy and computational efficiency.

7 Concluding remarks

The Eddy Dissipation Concept with the detailed chemistry approach and the standard k-ϵ turbulence model (with the standard constants) were applied to simulate the Sandia flame CHNa and the Sydney flame HM1E. The finite-rate chemistry effects were described by the FFR and the GRI3.0 mechanisms. The robust implicit Runge-Kutta method (RADAU5) was used for integrating stiff ordinary-differential equations to compute the reaction rates. The radiation heat transfer was treated with the simple P-1 model. Statistically stationary results were obtained and compared in detail with the available experimental data. In general, there was good agreement between the present simulations and measurements for both flames. It is believed that one of the main reasons for the observed discrepancies between the EDC-based predictions and experimental data for the Sandia flame CHNa was the round-jet anomaly of the k-ϵ turbulence model. The Sydney flame HM1E was calculated with the k-ω SST turbulence model as well. However, the predicted results did not reveal any significant deviations between the standard k-ϵ and the SST model which could be explained by the SST model implementation in OpenFOAM.

The steady laminar flamelet model was applied to investigate the influence of the turbulence-chemistry interaction. For this purpose the commercial code ANSYS FLUENT was utilized. It worth noticing that the same grids were used and the quite similar numerical methods, boundary conditions and the sub-models for the turbulence and radiative heat transfer were chosen. The finite-rate chemistry effects were taken into account using the FFR and GRI3.0 mechanisms. It was found that the most accurate SLF-based predictions for the Sandia flame CHNa was obtained with the modified constant $C_{\epsilon 1} = 1.52$. The present results obtained with the SLF-based approach and the default value of the PDF turbulence Schmidt number $\mathrm{Sc}_t = 0.85$ were found to be less accurate than the EDC-based for the Sydney flame HM1E due to the lack of the turbulence mixing. The calculation with the modified Schmidt number $\mathrm{Sc}_t = 0.4$ showed some improvement in the prediction of the composition and temperature but was not sufficient to match the experimental data well.

Overall, the present results give a good indication on the adequacy and accuracy of the implemented solver in the OpenFOAM toolbox and its readiness for further combustion application development.

Acknowledgements This work was conducted as a part of the CenBio Center for environmentally-friendly energy. We are grateful to the Norwegian Meta center for Computational Science (NOTUR) for providing the uninterrupted HPC computational resources and useful technical support.

References

1. ANSYS FLUENT R12. Theory guide. Tech. rep., Ansys Inc.; 2009.
2. Barlow, R.S. and Frank, J.H., Effects of turbulence on species mass fractions in methane/air jet flames, Proc. Combust. Inst., 27, 1087–1095 (1998)
3. Barlow, R.S., Fiechtner, G.J., Carter, C.D., and Chen, J.-Y., Experiments on the scalar structure of turbulent CO/H2/N2 jet flames, Combust. Flame, 120, 549-569 (2000)
4. Bowman, C.T., Hanson, R.K., Davidson, D.F., Gardiner, W.C., Lissianski, V., Smith, G.P., Golden, D.M., Frenklach, M., Goldenberg, M.: GRI-Mech (2008). http://www.me.berkeley. edu/gri-mech/. Accessed February 2013
5. Chase, M., NIST-JANAF Thermochemical tables, 4th Ed., J. Phys. Chem. Ref. Data, Monographs and Supplements, 9 (1998)
6. Cheng, P., Dynamics of a radiating gas with application to flow over a wavy wall, AIAA J., 4, 238-245 (1966)
7. Chomiak, J., Karlsson, A., Flame liftoff in diesel sprays, In proceedings of 26th International Symposium on Combustion, pp. 2557-2564 (1996)
8. Cuoci, A., Frassoldati A., Ferraris, G. Buzzi, Faravelli, T., Ranzi, E., The ignition, combustion and flame structure of carbon monoxide/hydrogen mixtures. Note 2: Fluid dynamics and kinetic aspects of syngas combustion, Int. J. Hydrogen Energy, 32, 3486-3500 (2007)
9. Dally, B.B., Masri, A.R., Barlow, R.S. and Fiechtner, G.J., Instantaneous and mean compositional structure of bluff- body stabilised nonpremixed flames, Combust. Flame, 114, 119–148 (1998)
10. Dunn, M. J., Masri, A. R. and Bilger, R. W., A new piloted premixed jet burner to study strong finite-rate chemistry effects, Combust. Flame, 151, 46–60 (2007)
11. Dunn, M. J., Masri, A. R., Bilger, R. W., Barlow, R. S. and Wang, G. H., The compositional structure of highly turbulent piloted premixed flames issuing into a hot coflow, Proc. Combust. Inst., 32, 1779–1786 (2009)
12. Fox, R.O., Computational models for turbulent reacting flows. Cambridge University Press. Cambridge (2003)
13. Frank, J.H., Barlow, R.S., Lundquist, C., Radiation and nitric oxide formation in turbulent non-premixed jet flames, Proc. Comb. Inst, 28, 447–454 (2000)
14. Frassoldati, A., Faravelli, T., Ranzi, E., The ignition, combustion and flame structure of carbon monoxide/hydrogen mixtures. Note 1: Detailed kinetic modeling of syngas combustion also in presence of nitrogen compounds, Int. J. Hydrogen Energy, 32, 3471-3485 (2007)
15. Ertesvåg, I. S. and Magnussen, B. F., The eddy dissipation turbulence energy cascade model, Combust. Sci. Technol. 159, 213–235 (2000)
16. Geurts, B., Elements of direct and large-eddy simulation. R.T.Edwards. Philadelphia (2004)
17. Gran, I. R. and Magnussen, B. F., A numerical study of a bluff-body stabilized diffusion flame. Part 2. Influence of combustion modeling and finite-rate chemistry, Combust. Sci. Technol., 119, 191-217 (1996)
18. Hairer, E. and Wanner, G., Solving ordinary differential equations II: Stiff and differential-algebraic problems, 2nd ed. Springer Series in Computational Mathematics. Springer-Verlag (1996)
19. Hestens, M, Steifel, E., Methods of conjugate gradients for solving systems of algebraic equations, J. Res. Nat. Bur. Stand, 29, 409–436 (1952)
20. Hewson, J.C., Kerstein, A.R., Stochastic simulation of transport and chemical kinetics in turbulent CO/H2/N2 flames. Combust. Theory Model., 5, 669-897 (2001)
21. Hossain, M., Jones, J.C., Malalasekera, W., Modelling of a bluff-Body nonpremixed flame using a coupled radiation/flamelet combustion model, Flow Turbul. Combust., 67, 217–234 (2001)
22. Hottel, H. C, and Sarofim, A.F., Radiative Transfer. McGraw-Hill. New York (1967)
23. Hutchinson, B., Raithby, G., A multigrid method based on the additive correction strategy, J. Numer. Heat Transfer, 9, 511–37 (1986)
24. Issa, R., Solution of the implicitly discretized fluid flow equations by operator splitting, J. Comput. Phys., 62, 40–65 (1986)

25. Jacobs, D., Preconditioned conjugate gradient methods for solving systems of algebraic equations, Tech. rep., Central Electricity Research Laboratories, Leatherhead, Surrey, England (1980)
26. Jones, W.P., Whitelaw, J.H., Calculation methods for reacting turbulent flows: a review, Combust. Flame, 48, 1-26 (1982)
27. Launder B, Sharma B. Application of the energy-dissipation model of turbulence to the calculation of flow near a spinning disc. Lett. Heat Mass Transfer, 1, 131–138 (1974)
28. Launder, B. E. and Spalding, D. B., The numerical computation of turbulent flows, Comput. Method Appl. M., 3, 269–289 (1974)
29. Leonard, B.P., Mokhtari, S., ULTRA-SHARP Nonoscillatory convection schemes for high-speed steady multidimensional flow, NASA TM 1-2568 (ICOMP-90-12), NASA Lewis Research Center (1990)
30. Lilleberg, B., Christ D., Ertesvåg, I.S., Rian, K.E., Kneer, R., Numerical simulation with an extinction database for use with the Eddy Dissipation Concept for turbulent combustion, Flow Turbul. Combust., 91, 319-346 (2013)
31. Liu, K., Pope, S.B., Caughey, D.A., Calculations of bluff-body stabilized flames using a joint probability density function model with detailed chemistry, Combust. Flame, 141, 89–117 (2005)
32. Lysenko, D.A., Ertesvåg, I.S., Rian K.E., Modeling of turbulent separated flows using OpenFOAM, Comput. Fluids, 80, 408–422 (2013)
33. Magnussen, B.F., Hjertager, B.H., On mathematical modeling of turbulent combustion with special emphasis on soot formation and combustion, Proc. Combust. Inst. 16, 719–729 (1976)
34. Magnussen, B.F., Modeling of NOx and soot formation by the Eddy Dissipation Concept. Int.Flame Research Foundation, 1st topic Oriented Technical Meeting., 17-19 Oct., Amsterdam, Holland (1989)
35. Marshak, R.E. Note on the spherical harmonics method as applied to the Milne problem for a sphere, Phys. Rev., 71, 443-446 (1947)
36. Marzouk, O.A., Huckaby, E.D., A comparative study of eight finite-rate chemistry kinetics for CO/H_2 combustion, Eng. App. Comput. Fluid Mech., 4, 331-356 (2010)
37. McGuirk, J.J., Rodi, W., The calculation of three-dimensional turbulent free jets. In turbulent Shear Flows I: Selected papers from the First International Symposium on Turbulent Shear Flows, editors: Durst, F., Launder, B.E., Schmidt, F.W., and Whitelaw, J.H., Springer-Verlag, Germany, 71-83 (1979)
38. Menter, F.R., Two-equation eddy-viscosity turbulence models for engineering applications, AIAA J., 32, 1598-1605 (1994)
39. Menter, F., Esch, T., Elements of Industrial Heat Transfer Prediction, 16th Brazilian Congress of Mechanical Engineering (COBEM), 2001
40. Merci, B., Naud, B., Roekaerts, D., Impact of turbulent flow and mean mixture fraction results on mixing model behavior in transported scalar PDF simulations of turbulent non-premixed bluff body flames, Flow Turbul. Combust., 79, 41-53 (2007)
41. Merci, B., Naud, B., Roekaerts, D., Maas, U., Joint scalar versus joint velocity-scalar PDF simulations of bluff-body stabilized flames with REDIM, Flow Turbul. Combust., 82, 185-209 (2009)
42. Peters., N., Laminar diffusion flamelet models in non premixed combustion, Prog. Energy Combust. Sci., 10, 319-339 (1984)
43. Peters, N., Turbulent Combustion. Cambridge University Press. Cambridge (2000)
44. Pitsch, H., Peters, N., A consistent flamelet formulation for non-premixed combustion considering differential diffusion effects, Comb., Flame, 114, 26-40 (1998)
45. Pope, S.B., An explanation of the turbulent round-jef/plane-jet anomaly, AIAA J., 16, 279-281 (1978)
46. Raithby, G.D., Chui, E.H., A finite-volume method for predicting a radiant heat transfer in enclosures with participating media, J. Heat Transfer, 122, 415-423 (1990)
47. Raman, V., Pitsch, H., Fox, R.O., Hybrid large-eddy simulation/Lagrangian filtered-density-function approach for simulating turbulent combustion, J. Comb. Flame, 143, 56-78 (2005)
48. Richardson, L.F., Weather prediction by numerical process. Cambridge University Press. Cambridge (1922)

49. Rhie, C., Chow, W., Numerical study of the turbulent flow past an airfoil with trailing edge separation, AIAA J., 21, 1525–32 (1983)
50. Sabelnikov, V., Fureby, C., LES combustion modeling for high Re flames using a multi-phase analogy, Combust. Flame, 160, 83–96 (2013)
51. Shih T-H, Liou W, Shabbir A, Yang Z, Zhu J. A new k-ϵ eddy-viscosity model for high Reynolds number turbulent flows – model development and validation, Comput. Fluids, 24, 227–38 (1995)
52. Smith, T.F., Shen, Z.F. and Friedman, J.N. , Evaluation of coefficients for the weighted sum of gray gases model, J. Heat Trans-T., ASME, 104, 602–608 (1982)
53. Warnatz, J., Maas, U., Dibble R.W., Combustion, 4th ed. Springer. Berlin Heidelberg New York (2006)
54. Waterson, N.P., Deconinck, H., Design principles for bounded higher-order convection schemes – a unified approach, J Comput. Phys., 224, 182–207 (2007)
55. Weller, H.G., Tabor, G., Jasak H., Fureby, C., A tensorial approach to computational continuum mechanics using object-oriented techniques, J. Comp. Phys., 12, 620–631 (1998)
56. Williams, F.A., Turbulent mixing in non-reactive and reactive flows (S.N.B. Muurthy, ed.), p. 189, Plenum (1975)
57. Yan, J., Thiele, F., Buffat, M., A turbulence model sensitivity study for CH4/H2 bluff-body stabilized flames, Flow Turb. Combust., 73, 1–24 (2004)
58. Vandoormaal, J.P., Raithby, G.D., Enhancements of the SIMPLE method for predicting incompressible fluid flows, Numer. Heat Transfer, 7, 147–163 (1984)
59. Zahirović, S., Scharler, R., Kilpinen, P., Obernberger, I., Validation of flow simulation and gas combustion sub-models for the CFD-based prediction of NOx formation in biomass grate furnaces, Combust. Theory Model., 15, 61–87 (2011)

5.3 Paper C

Is not included due to copyright

5.4 Paper D

Is not included due to copyright

5.5 Paper E

Is not included due to copyright

5.6 Paper F

Noname manuscript No.
(will be inserted by the editor)

Numerical simulations of the Sandia Flame D using the Eddy Dissipation Concept

Dmitry A. Lysenko · Ivar S. Ertesvåg · Kjell Erik Rian

Received: date / Accepted: date

Abstract A turbulent piloted methane/air diffusion flame (Sandia Flame D) is calculated using both compressible Reynolds-averaged and large-eddy simulations (RAS and LES, respectively). The Eddy Dissipation Concept (EDC) is used for the turbulence-chemistry interaction, which assumes that molecular mixing and the subsequent combustion occur in the 'fine structures' (smaller dissipative eddies, which are close to the Kolmogorov length scales). Assuming the full turbulence energy cascade, the characteristic length and velocity scales of the 'fine structures' are evaluated using a standard k-ϵ turbulence model for RAS and a one-equation eddy-viscosity sub-grid scale model for LES. Finite-rate chemical kinetics are taken into account by treating the 'fine structures' as constant pressure and adiabatic homogeneous reactors (calculated as a system of ordinary-differential equations (ODEs)) described by a Perfectly Stirred Reactor (PSR) concept. A robust implicit Runge-Kutta method (RADAU5) is used for integrating stiff ODEs to evaluate reaction rates. The radiation heat transfer is treated by the P1-approximation. The assumed β-PDF approach is applied to assess the influence of modeling of the turbulence-chemistry interaction. Numerical results are compared with available experimental data. In general, there is good agreement between present simulations and measurements both for RAS and LES, which gives a good indication on the adequacy and accuracy of the method and its further application for turbulent combustion simulations.

Dmitry A. Lysenko · Ivar S. Ertesvåg
Department of Energy and Process Engineering, Norwegian University of Science and Technology, Kolbjørn Hejes vei 1B, NO–7491, Trondheim, Norway
Tel.: +47-73-593755
Fax: +47-73-593580
E-mail: dmitry.lysenko@ntnu.no

Kjell Erik Rian
Computational Industry Technologies AS, NO–7462, Trondheim, Norway

Keywords Reynolds-averaged simulations · Large-eddy simulation · Eddy Dissipation Concept · RADAU5 · Sandia Flame D · Perfectly Stirred Reactor · OpenFOAM

1 Introduction

The long-term goal of the present work is to develop a large-eddy simulation model for high Reynolds number flows of practical interest with further adaptation for turbulent combustion modeling. The core numerical method is based on the OpenFOAM toolbox [57] which was originally developed as a high-end C++ classes library (Field Operation and Manipulation) for a broad range of fluid dynamics applications, but quickly became very popular in industrial engineering as well as in academic research.

Previously, methodical investigations for several plane turbulent bluff-body flows have been carried out with the goal of validation, verification and understanding of the capabilities of the numerical method using the conventional approach for solution of the steady/unsteady compressible Reynolds-averaged Navier-Stokes equations (RANS/URANS), which sometimes referred to as "Reynolds-averaged simulations" (RAS). These results were analyzed in detail and agreed fairly well with experimental data [35].

Recently, Lilleberg et al.[33] carried out several turbulent combustion calculations of detailed flame experiments such as the Sandia Flames D,E [2] and a piloted lean lean-premixed jet burner [8], [9]. Lilleberg and his co-workers [33] used a classical approach for the solution of the steady, compressible Reynolds-averaged Navier-Stokes (RANS) equations, where the turbulence was treated via a standard k-ϵ model [31] and adopted several ways to couple chemical kinetics with the Eddy Dissipation Concept [40], [10], including fast chemistry, local extinction and detailed chemistry approaches. As was expected, the detailed chemistry approach showed the best agreement with the measured data for all cases.

Later, the validation of the method was extended for two benchmark flames: the Sandia Flame CHNa [3] and the Sydney Bluff-Body Flame HM1E [7]. Both flames were calculated using the standard k-ϵ model [31]. The turbulence-chemistry interaction was treated via EDC with the detailed chemistry [17] described by the full GRI-3.0 mechanism [4]. In general, there was good agreement between these simulations and measurements for both flames. It is believed that one of the main reasons for the observed discrepancies between the predictions and experimental data was the round-jet anomaly of the k-ϵ turbulence model. Overall, these preliminary results [38] (together with previously obtained results [32],[33]) give a good indication on the adequacy and accuracy of the implemented solver and its readiness for further combustion application development.

In the present study, the method was updated for the combustion LES. Earlier, the LES technique (with several sub-grid scales models) was validated against the flows over a circular cylinder at Reynolds numbers $\mathrm{Re} = 3.9 \times 10^3$

[36] and $\mathrm{Re} = 2 \times 10^4$ [37]. One of the possible extension of the EDC as a subgrid scale combustion model for LES was proposed by Panjwani [44]. Here, its further development is provided as well as the simulation results of the Sandia Flame D [2].

Thus, the aim of this work is further validation of the OpenFOAM capabilities for RAS/LES applications to the combustion flows of engineering interest. Another scope of this work is to provide high-quality documentation of the implemented method and its detailed validation.

The paper is divided into four main parts. The first and the second parts of the paper describe the mathematical and numerical modeling, respectively. Then, a general description of the test cases is given. Finally, computational results are presented, results are analyzed and discussed, and conclusions are drawn.

2 Mathematical modeling

One of the most commonly adopted approach in modeling of turbulent reacting flows in the context of RANS/URANS is the Eddy Dissipation Concept (EDC). Initially developed in the 1970s [39], EDC was formulated as a well-established turbulent combustion closure model in the 1990s - 2000s [40], [17], [10].

2.1 Reynolds-averaged simulations

In the present work we will not provide the details of the EDC in the context of Reynolds averaging simulations, see, for example, the work by Lilleberg et al. [33] for the comprehensive model description. It worth noticing only that in the present study the EDC was coupled with the detailed chemistry approach. For this purpose, the concept of the Perfect Stirred Reactor [17] was utilized with the chemical kinetic mechanism GRI-3.0 [4]. The turbulence was modeled using the standard k-ϵ model [31]. The radiation was treated by the P1-approximation [6].

2.2 Large-eddy simulations

Here, the extension of EDC in the context of the large-eddy simulation is provided.

2.3 Governing equations

In present LES, the relevant flow variables are filtered in the physical space (assuming weighted averaging in a given volume). The filterd variable $\bar{f}(x)$

denotes by overbar is defined as

$$\bar{f}\left(x\right)=\int_{V}G\left(x-x^{*}\right)f\left(x^{*}\right)dx^{*}, \tag{1}$$

where V is the volume of the LES filter and G is a filter kernel. In the present study a top-hat (or sometimes called 'box') filter [15], where the filter operations in each x_j direction are identical, is employed. The filter width Δ is defined as $\Delta=\left(\Delta_x\Delta_y\Delta_z\right)^{1/3}$ assuming the filter kernel as

$$G\left(x\right)=G(x_1,x_2,x_3)\begin{cases}1/\Delta & |x_i|<\Delta_i/2,\quad i=1,2,3\\ 0 & \text{otherwise}\end{cases} \tag{2}$$

where (x_1, x_2, x_3) are the spatial coordinates of the location x.

A mass-weighted, Favre filtering is introduced as:

$$\bar{\rho}\tilde{f}\left(x\right)=\int_{V}\rho G\left(x-x^{*}\right)f\left(x^{*}\right)dx^{*}. \tag{3}$$

The filtered Favre-averaged balance equations of mass, momentum, energy and species are:

$$\frac{\partial\bar{\rho}}{\partial t}+\frac{\partial\bar{\rho}\tilde{u}_j}{\partial x_j}=0 \tag{4}$$

$$\frac{\partial\bar{\rho}\tilde{u}_i}{\partial t}+\frac{\partial\bar{\rho}\tilde{u}_i\tilde{u}_j}{\partial x_j}=-\frac{\partial\bar{p}}{\partial x_i}+\frac{\partial\tilde{\tau}_{ij}}{\partial x_j}-\frac{\partial}{\partial x_j}\left(\bar{\rho}\left(\widetilde{u_iu_j}-\tilde{u}_i\tilde{u}_j\right)\right) \tag{5}$$

$$\frac{\partial\bar{\rho}\tilde{Y}_s}{\partial t}+\frac{\partial\bar{\rho}\tilde{Y}_s\tilde{u}_j}{\partial x_j}=\frac{\partial}{\partial x_j}\left(\bar{\rho}D_s\frac{\partial\tilde{Y}_s}{\partial x_j}\right)-\frac{\partial}{\partial x_j}\left(\bar{\rho}\left(\widetilde{u_jY_s}-\tilde{u}_j\tilde{Y}_s\right)\right)+\bar{\omega}_s \tag{6}$$

$$\frac{\partial\bar{\rho}\tilde{h}}{\partial t}+\frac{\partial\bar{\rho}\tilde{h}\tilde{u}_j}{\partial x_j}=\frac{\partial}{\partial x_j}\left(\overline{\xi_j^h}+\overline{u_i\tau_{ij}}\right)-\frac{\partial}{\partial x_j}\left(\bar{\rho}\left(\widetilde{u_jh}-\tilde{u}_j\tilde{h}\right)\right)+\frac{\partial\bar{p}}{\partial t}-\frac{\partial}{\partial x_j}\left(\bar{q}_r\right)+\bar{S}_{hc} \tag{7}$$

where $\bar{f}$ and $\tilde{f}$ denote Favre-filtered quantities instead of ensemble means. Here, ρ is the density, u is the velocity, p is the pressure, $h=\sum_s\tilde{Y}_s\int C_{p,s}\,d\tilde{T}$ represents the enthalpy, T is the temperature, Y_s is the species mass fraction, D_s is the mass diffusion coefficient for species s in a mixture ($D_s = D = 2.88\times10^{-5}$ m^2/s), ω_s is the species reaction rate, q_r is the radiative heat loss, S_{hc} represents the source term due to combustion and $\overline{\xi_j^h}$ is the filtered laminar diffusion flux.

$\bar{S}_{hc}$ is modeled according to

$$\bar{S}_{hc}=-\sum_{s=1}^{N}\frac{\bar{\omega}_s}{M_s}h_{f,s}^{\theta}\ , \tag{8}$$

where $h_{f,s}^{\theta}$ is the species formation enthalpy, M_s is the species molecular weight.

Here, $C_{p,s}$ is calculated as a function of temperature from a set of coefficients taken from NIST-JANAF thermochemical tables [5].

The subgrid flow physics is concealed in the subgrid stress tensor $\mathbf{B} = \bar{\rho}\left(\widetilde{u_i u_j} - \tilde{u}_i \tilde{u}_j\right)$ and flux vectors $\mathbf{b}_s = \bar{\rho}\left(\widetilde{u_j Y_s} - \tilde{u}_j \tilde{Y}_s\right)$ and $\mathbf{b}_h = \bar{\rho}\left(\widetilde{u_j h} - \tilde{u}_j \tilde{h}\right)$. The subgrid pressure fluctuations and dissipation terms are neglected. Moreover, the subgrid-scales incompressibility hypothesis [13] is used for derivation of the energy balance equation, assuming low Mach number limit.

It is assumed that the gas mixture behaves as a linear viscous (Newtonian) fluid, which assumes that $\bar{\rho}$, $\bar{p}$ and $\tilde{T}$ are linked by the equation of state $\bar{p} = \bar{\rho} R \tilde{T}$, where R the composition dependent gas constant.

The shear-stress tensor τ_{ij} is given by

$$\tilde{\tau}_{ij} = 2\mu \widetilde{\mathbf{S}}_{ij} - \frac{2}{3}\mu \delta_{ij} \widetilde{\mathbf{S}}_{kk} = 2\mu \widetilde{\mathbf{S}}_D, \tag{9}$$

where $\widetilde{\mathbf{S}}_{ij}$ the components of the viscous stress (rate-of-strain) tensor $\widetilde{\mathbf{S}}$ defined as,

$$\widetilde{\mathbf{S}}_{ij} = \frac{1}{2}\left(\frac{\partial \tilde{u}_i}{\partial x_j} + \frac{\partial \tilde{u}_j}{\partial x_i}\right), \tag{10}$$

and μ the viscosity, and

$$\widetilde{\mathbf{S}}_D = \frac{1}{2}\left(\frac{\partial \tilde{u}_i}{\partial x_j} + \frac{\partial \tilde{u}_j}{\partial x_i}\right) - \frac{1}{3}\delta_{ij}\frac{\partial \tilde{u}_i}{\partial x_j} \tag{11}$$

the deviatoric part of $\mathbf{S}$.

Explicit LES closures can typically be classified as functional or structural models [50], [13]. Functional models are designed based on the turbulence energy cascade from large- to small-scales considered for the fully-developed turbulent flows. The energy drain for the energy cascade is modeled using the hypothesis of a subgrid viscosity μ_B [11] resulting in

$$\mathbf{B} = \frac{2}{3}\bar{\rho}\delta_{ij}\tilde{k} - 2\mu_B \widetilde{\mathbf{S}}_D. \tag{12}$$

To close these models, the one equation eddy viscosity model [58] is utilized for which the subgrid viscosity is given by $\mu_B = c_k \bar{\rho}\sqrt{\tilde{k}}\Delta$, and the subgrid kinetic energy $\tilde{k}$ is estimated by solving a separated modeled transport equation of the form,

$$\frac{\partial \bar{\rho}\tilde{k}}{\partial t} + \frac{\partial \bar{\rho}\tilde{k}\tilde{u}_j}{\partial x_j} = \mathbf{F}_p + \mathbf{F}_d - \mathbf{F}_\epsilon, \tag{13}$$

$$\mathbf{F}_p = -\mathbf{B} \cdot \widetilde{\mathbf{S}}, \tag{14}$$

$$\mathbf{F}_d = \frac{\partial}{\partial x_j}\left((\mu_B + \mu)\frac{\partial \tilde{k}}{\partial x_j}\right), \tag{15}$$

$$\mathbf{F}_\epsilon = c_\epsilon\, \bar{\rho}\, \tilde{k}^{3/2}/\Delta, \tag{16}$$

where $\mathbf{F}_p$ is production, $\mathbf{F}_d$ diffusion and $\mathbf{F}_\epsilon$ dissipation terms, respectively, and c_k, c_ϵ are model coefficients. It is worth noticing that both models coefficients can be calculated dynamically using two levels of filtering and scale similarity. However, it was found that the dynamic procedure leads to the numerical instabilities for the combustion LES with the EDC, and static coefficients $c_k = 0.07$ and $c_\epsilon = 1.048$ [50] were used in the present study.

The subgrid fluxes are modeled according to a simple gradient diffusion approximation

$$\mathbf{b}_s = \frac{\mu_B}{\mathrm{Sc}_{t,s}} \left(\frac{\partial \tilde{Y}_s}{\partial x_j} \right), \tag{17}$$

$$\mathbf{b}_h = \frac{\mu_B}{\mathrm{Pr}_t} \left(\frac{\partial \tilde{h}}{\partial x_j} \right), \tag{18}$$

where $\mathrm{Sc}_{t,s}$ and Pr_t are turbulence Schmidt and Prandtl numbers, which were set to $\mathrm{Sc}_{t,s} = \mathrm{Pr}_t = 0.7$.

2.3.1 EDC for turbulent combustion

The Eddy Dissipation Concept is based on the energy cascade model and assumes that molecular mixing and chemical reactions occur on the smaller dissipative eddies, which are close to the Kolmogorov length scales and are termed 'fine structures'. The characteristic length L^* and velocity u^* scales of the fine structures are of the same order of magnitude as Kolmogorov scales and can be expressed as

$$L^* = \frac{2}{3} \left(\frac{3C_{D2}^3}{C_{D1}^2} \right)^{1/4} \left(\frac{\nu^3}{\tilde{\epsilon}} \right)^{1/4}, \tag{19}$$

$$u^* = \left(\frac{C_{D2}}{3C_{D1}^2} \right)^{1/4} (\nu \tilde{\epsilon})^{1/4}, \tag{20}$$

where $C_{D1} = 0.134$ and $C_{D2} = 0.5$ [10]. Here, we assume that the full cascade takes place at each numerical cell, and the connection between the fine structure and the larger eddies is achieved through the cascade. Thus, characteristics of the large eddies such as velocity u' can be evaluated using the turbulence model. The turbulence kinetic energy $\tilde{k}$ is found from the the solved transport equation (Eqn. 13). The dissipation of the subgrid kinetic energy $\tilde{\epsilon}_{sgs}$ is expressed as

$$\tilde{\epsilon}_{sgs} = c_\epsilon \, \overline{\rho} \, \tilde{k}^{3/2} / \Delta, \tag{21}$$

where the model constant $c_\epsilon = 1.048$.

In the model expressed below, different superscripts refer to states inside fine structures (*), surroundings ($\circ$) and filtered values of the computational cell ($\sim$).

The ratio between the mass in the fine structures and the total mass is postulated as

$$\gamma^* = \left(\frac{u^*}{u'}\right)^2 = \left(\frac{3C_{D2}}{4C_{D1}^2}\right)^{1/2} \left(\frac{\nu\tilde{\epsilon}}{\tilde{k}^2}\right)^{1/2} \tag{22}$$

The mass exchange between the fine structures and the surroundings, divided by the mass of the fine structures, is defined as

$$\dot{m}^* = 2\frac{u^*}{L^*} = \left(\frac{3}{C_{D2}}\right)^{1/2} \left(\frac{\tilde{\epsilon}}{\nu}\right)^{1/2} \tag{23}$$

The mass exchange between the fine structures and the surroundings, divided by the total mass, is calculated according to

$$\dot{m} = \gamma^* \dot{m}^* \tag{24}$$

The mass-averaged filtered reaction rate for the s-th specie is given as

$$-\bar{\omega}_s = \frac{\bar{\rho}\dot{m}\chi}{1-\gamma^*\chi}\left(\tilde{Y}_s - Y_s^*\right),\ s = 1, \ldots, N_s \tag{25}$$

and the relationship between the mass-averaged mean state, fine-structure state and surrounding state is expressed as

$$\tilde{\Psi} = \gamma^*\chi\Psi^* + (1-\gamma^*\chi)\Psi^\circ \tag{26}$$

Here, χ is the reacting fraction of the fine structures, which can depend on probability of co-existence of the reactants, degree of heating and a limiter to the reaction due to lack of reactants. In the present study, $\chi = 1$, as suggested by Gran and Magnussen [17]. The mass fraction $\tilde{Y}_s$ for species s is calculated from solving the species mass transport equation for each individual species. The fine-structure mass fraction Y_s^* is computed through the detailed chemistry approach.

2.3.2 The detailed chemistry approach

Finite-rate chemical kinetics are taken into account by treating the fine structures as constant pressure and adiabatic homogeneous reactors. Thus, the fine structures mass fractions values Y_s^* can be calculated by solving a system of ODEs describing a Perfectly Stirred Reactor (PSR) [17],

$$\frac{dY_s^*}{dt} = \frac{\omega_s^*}{\rho^*} + \frac{1}{\tau^*}\left(Y_s^\circ - Y_s^*\right),\ s = 1, \ldots, N_s \tag{27}$$

The reaction rate ω_s^* is evaluated from a chemical kinetics mechanism. Y_s° is the mass fraction of the inflow stream to the reactor. In the present study, it is assumed adiabatic and isobaric PSRs. Further, it is assumed that the PSRs are at steady state [17], meaning that the steady-state solution of Eq.27 is achieved by integrating it in time to steady state.

It is worth noticing that the residence or mixing time scale τ^* is evaluated using the molecular viscosity and the dissipation rate

$$\tau^* = \frac{1}{\dot{m}^*} \tag{28}$$

In the present study the chemistry was treated by the single step mechanism:

$$\mathrm{CH_4} + 2\mathrm{O_2} = \mathrm{CO_2} + 2\mathrm{H_2O} \tag{29}$$

with the following rate parameters: $A = 9.49 \times 10^{11}$ [m, kg, mol, s], $\beta = 0$, $T_a = 23650$ K, $n_{CH4} = 0.7$ and $n_{O2} = 0.8$. It worth noticing, that applying of more detailed kinetic schemes such as the GRI3.0 mechanism is still computationally expensive and was out of scope of the present work.

2.4 The mixture fraction probability density function model

In the present study the mixture fraction, f is defined as [55]

$$f = \frac{Z_i - Z_{i,ox}}{Z_{i,fuel} - Z_{i,ox}}, \tag{30}$$

where Z_i is the elemental mass fraction for element i. The subscripts ox and fuel denote the value at the oxidizer and fuel stream inlets, respectively. Using the standard assumptions of the equal diffusion coefficients for all species, and assuming that the considered flow is turbulent, (where turbulent convection overwhelms molecular diffusion), f is the elemental mass fraction. The Favre-mean transport equation for $\tilde{f}$ and its variance $\widetilde{f''^2}$ [29] are

$$\frac{\partial}{\partial t}\left(\bar{\rho}\tilde{f}\right) + \frac{\partial}{\partial x_j}\left(\bar{\rho}\tilde{u}_j\tilde{f}\right) = \frac{\partial}{\partial x_j}\left(\frac{\mu_t}{\mathrm{Sc}_t}\frac{\partial \tilde{f}}{\partial x_j}\right), \tag{31}$$

$$\frac{\partial}{\partial t}\left(\bar{\rho}\widetilde{f''^2}\right) + \frac{\partial}{\partial x_j}\left(\bar{\rho}\tilde{u}_j\widetilde{f''^2}\right) = \frac{\partial}{\partial x_j}\left(\frac{\mu_t}{\mathrm{Sc}_t}\frac{\partial \widetilde{f''^2}}{\partial x_j}\right) + C_g\mu_t\left(\frac{\partial \tilde{f}}{\partial x_j}\right)^2 - C_d\bar{\rho}\frac{\tilde{k}}{\tilde{\epsilon}}\widetilde{f''^2}, \tag{32}$$

where $f'' = f - \tilde{f}$, $\mathrm{Sc}_t = 0.85$, $C_g = 2.86$ and $C_d = 2$.

For the Reynolds-averaged calculations, $\tilde{k}$ and $\tilde{\epsilon}$ are retrieved from the transport equations of the standard k-ϵ model [31].

For the large-eddy simulation, $\widetilde{f''^2}$ is modeled according to

$$\widetilde{f''^2} = C_k L_s^2 \left|\frac{\partial \tilde{f}}{\partial x_j}\right|^2, \tag{33}$$

where L_s is the mixing length for sub-grid scales and C_v is constant. The mixing length scale is computed as

$$L_s = \frac{\tilde{k}^{3/2}}{\tilde{\epsilon}}, \tag{34}$$

where $\tilde{k}$ is retrieved from the transport Eq. 13 and $\tilde{\epsilon}$ is calculated according to Eq. 21. The constants C_k and Sc_t are computed by applying the dynamic procedure proposed by Germano [14]. It worth noticing that both constants c_k and c_ϵ from Eq. 13 for the assumed β-PDF approach are computed dynamically as well.

In the present study a chemical equilibrium assumption is used, where reactions rates are sufficiently fast for the mixture to be in a state of chemical equilibrium. With this assumption the equilibrium state of density, temperature and composition can be obtained by minimizing the free energy [55].

The instantaneous values of mass fractions, density, temperature and enthalpy depend on the instantaneous mixture fraction:

$$\phi_i = \phi_i \left(f, h \right). \tag{35}$$

For the turbulence-chemistry interaction the assumed-shape probability density function (PDF) is used. Density weighted scalars are calculated as

$$\widetilde{\phi_i} = \int_0^1 \tilde{p} \left(f \right) \phi_i \, df. \tag{36}$$

In the present study, the PDF's are specified by tilde as Favre-probability-density functions. The β-function is used to model $\tilde{p} \left(f \right)$.

The non-adiabatic extension for this model is based on the assumption that the enthalpy fluctuations are independent on the enthalpy level:

$$\widetilde{\phi_i} = \int_0^1 \tilde{p} \left(f, \tilde{h} \right) \phi_i \, df, \tag{37}$$

and

$$p \left(f, \tilde{h} \right) = \tilde{p} \left(f \right) \delta \left(h - \tilde{h} \right), \tag{38}$$

where δ is the Delta function. Further, Eqs. 37-38 require solution of the model transport equation for the total enthalpy [22]

$$\frac{\partial}{\partial t} \left(\bar{\rho} \tilde{h} \right) + \frac{\partial}{\partial x_j} \left(\bar{\rho} \tilde{u}_j \tilde{h} \right) = \frac{\partial}{\partial x_j} \left(\frac{k_t}{C_p} \frac{\partial \tilde{h}}{\partial x_j} \right) - \frac{\partial}{\partial x_j} \left(\bar{q}_r \right), \tag{39}$$

where k_t is the turbulence thermal conductivity and C_p is the specific heat capacity. $\tilde{h}$ is defined in the following way:

$$\tilde{h} = \sum_{s=1}^{N} \tilde{Y_s} \widetilde{h_s}, \tag{40}$$

where $\tilde{Y_s}$ is the mass fraction of the species s and

$$\widetilde{h_s} = h_s^0 \left(T_{ref} \right) + \int_{T_{ref}}^{\tilde{T}} C_{p,s} \, dT \tag{41}$$

and $h_s^0 \left(T_{ref} \right)$ is the formation enthalpy of the species s at the reference temperature T_{ref}.

2.5 Modeling radiation

The radiation is modeled by the P1-approximation, which is the simplest form of the more generalized P-N method (or spherical harmonics) [6] assuming that a flame is optically thin. The radiative heat loss $\bar{q}_r$ is calculated as

$$-\frac{\partial}{\partial x_j}\bar{q}_r = \alpha_c G - 4e_c\sigma T^4, \tag{42}$$

where α_c is the absorption coefficient (m^{-1}), e_c is the emission coefficient (m^{-1}) and σ is the Stefan-Boltzmann constant. The incident radiation G is modeled according to

$$\frac{\partial}{\partial x_j}\left(\Gamma\frac{\partial}{\partial x_j}G\right) - \alpha_c G + 4e_c\sigma T^4 = 0, \tag{43}$$

$$\Gamma = \frac{1}{3\left(\alpha_c + \sigma_s\right)}, \tag{44}$$

where σ_s is the scattering coefficient ($\sigma_s = 1\ \mathrm{m}^{-1}$), respectively. The absorption coefficient and the emission coefficient are calculated using a weighted-sum-of-gray-gases model (WSGGM) [23] as a function of local concentrations of CO_2 and H_2O, path-length and pressure. The emissivity weighting factors for CO_2 and H_2O are taken from Smith et al. [53].

3 Brief description of the numerical methodology

The main emphasis of this work was put on the problem of validation of the Eddy Dissipation Concept implemented in the OpenFOAM (hereafter OF) toolbox [57]. However, to investigate the influence of the turbulence-combustion interaction modeling, the assumed β-PDF approach was tested as well using the ANSYS FLUENT (hereafter AF) technology [1]. It worth noticing, that the same grids were used for both solvers. The standard k-ϵ model [31] (SKE hereafter) with wall functions and the one-equation eddy-viscosity SGS model [58] (TKE hereafter) were used for the closure problem for URANS and LES, respectively. The radiative heat transfer was treated using the P-1 approximation.

3.1 OpenFOAM

The OpenFOAM code [57] was used for the EDC-based simulations. The solver was developed based on the finite-volume (FVM) method [15] and the the PISO (pressure implicit with splitting of operators) algorithm [54] for the pressure-velocity coupling, implemented according to Rhie and Chow type interpolation for the cell-centered data storage structure [25]. The preconditioned (bi-) conjugate gradient method [20] with incomplete-Cholesky preconditioner (ICCG) by Jacobs [26] was used for solving linear systems with a local

accuracy of 10^{-7} for all dependent variables at each time step for RAS, while a smooth solver (with a Gauss-Seidel smoother) was used for LES.

The numerical method had second-order accuracy in space and time. The linear-upwind interpolation scheme (the 'second-order upwind' scheme [56]) and linear (second-order central differences, CDS-2) interpolation were applied for convective terms approximation and other spatial derivatives, respectively, for RAS calculations.

For the large-eddy simulations, the Gamma scheme by Jasak et al. [27] was applied for the momentum equation convective-term approximations, which is a bounded form of CDS-2. The blending was controlled by a parameter, γ, which was set to $\gamma = 0.15$. As is common practice for reacting LES [45], [30], a total variation diminishing (TVD) scheme [19] was used for the scalars to avoid unphysical overshoots and second law violations.

A second-order implicit Euler method (BDF-2 [15]) was used for time integration together with the dynamic adjustable time stepping technique to guarantee a local Courant number less than 0.4 both for RAS and LES.

The calculation of the species reaction rate $\bar{\omega}_s$ requires the integration of Eq.27 for each computational cell in the domain. For this purpose, the robust RADAUS5 algorithm [18] was used. The RADAUS5 algorithm is designed for the solving stiff ODE systems and applies a 5th order accurate implicit Runge-Kutta method based on the Radau quadrature formula. The relative tolerance, absolute tolerance and maximum number of iterations to meet the target accuracy were set to 5×10^{-5}, 10^{-5} and 10^{7}, respectively.

3.2 ANSYS FLUENT

Using the factorized FVM [15], the RANS equations were solved with a second-order accuracy in space and time. The velocity and pressure fields were matched with a centered computational template based on the SIMPLEC [54] algorithm within the spirit of Rhie and Chou [49]. The convective terms were represented according to the Leonard quadratic upwind scheme (QUICK) [56] for RAS, while the bounded CDS-2 and second-order upwind schemes were used for LES for the momentum and other scalars, respectively. The linear system of equations was solved with Gauss–Seidel smoother, which was accelerated by an algebraic multi-grid (AMG) technique, based on the additive-correction strategy [24]. LES was carried out using implicit dual-stepping technique with the fixed time step of 10^{-5}s.

3.3 High performance computing

OpenFOAM is the massive parallel open source C++ classes library based on message-passing interface (MPI). The most of the present calculations were carried out using Vilje HPC facility (www.notur.no). RAS calculations were carried out using 32 cores in parallel, while LES simulations were performed

using 80 cores. In general, it was required approximately 2 weeks for RAS and $3-4$ weeks for LES to achieve statistically converged solutions.

4 Test case description

4.1 Experimental setup

The Flame D from the Sandia/TNF workshop is a piloted methane-air diffusion flame [2]. The central main jet consisted of a methane-air mixture (with 25% by volume of CH_4) corresponding to an equivalence ratio of 3.174. This is above the upper flammability limit of methane so combustion is still controlled by mixing. It was surrounded by a pilot flame and a slow coflow of air outside. The bulk velocities of the main jet, pilot and coflow were $U_\infty = 49.6$ m/s, $U_p = 11.4$ m/s and $U_c = 0.9$ m/s, respectively. The main jet nozzle had an inner diameter (d) of 7.2×10^{-3} m, which resulted in a jet Reynolds number, $\mathrm{Re}_j = U_\infty d/\nu = 2.24 \times 10^4$, where ν is the main jet kinematic viscosity, $\nu = 1.58 \times 10^{-5}\mathrm{m}^2/\mathrm{s}$. Flame D exhibited local extinction to a limited degree [2]. The pilot flame was burning a mixture of C_2H_2, H_2, air, CO_2, and N_2 with an enthalpy and equilibrium composition that is equivalent to a mixture of methane and air at an equivalence ratio of $\phi = 0.77$. The pilot annulus inner and outer diameters were 7.7×10^{-3} m and 18.2×10^{-3} m, respectively. The experimental data was documented in detail by Barlow and Frank [2].

4.2 RAS grids and boundary conditions

Some details of the RAS computational domain are shown in Fig. 1. The axial and radial dimensions of the computational domain after the burner exit were set to $76.5 \times d$ and $20.83 \times d$, respectively. The EDC-based simulations were carried out for two grids. The coarse grid had 110 and 40 cells along the axial and radial directions, respectively. The jet pipe was resolved with 4 cells, and the pilot was resolved with 5 cells, in the radial direction. The length of the pre-inlet fuel and pilot pipes were approximately $15 \times d$. The second mesh was designed just by a subsequent grid refinement by factor 2 in both radial and axial direction. Details of the fine grid are presented in Fig. 1.

In general, the differences between EDC-based results obtained on these grids were insignificant for the mean velocities, temperature and main species such as O_2, N_2, CO_2, H_2O and H_2. However, for the intermediate species such as CO, OH and NO, high-resolution grid provides more accurate results. Therefore, all present EDC-based and β-PDF-based results discussed below were obtained using the high-resolution grid (termed hereafter RAS-A2). Further grid refinement was not carried out due to resource limitations.

The problem was solved assuming symmetry about the centerline. The computational domain was designed as a sector of 5^o with imposed periodic boundary conditions and included pre-inlet pipes for the fuel-jet and pilot in

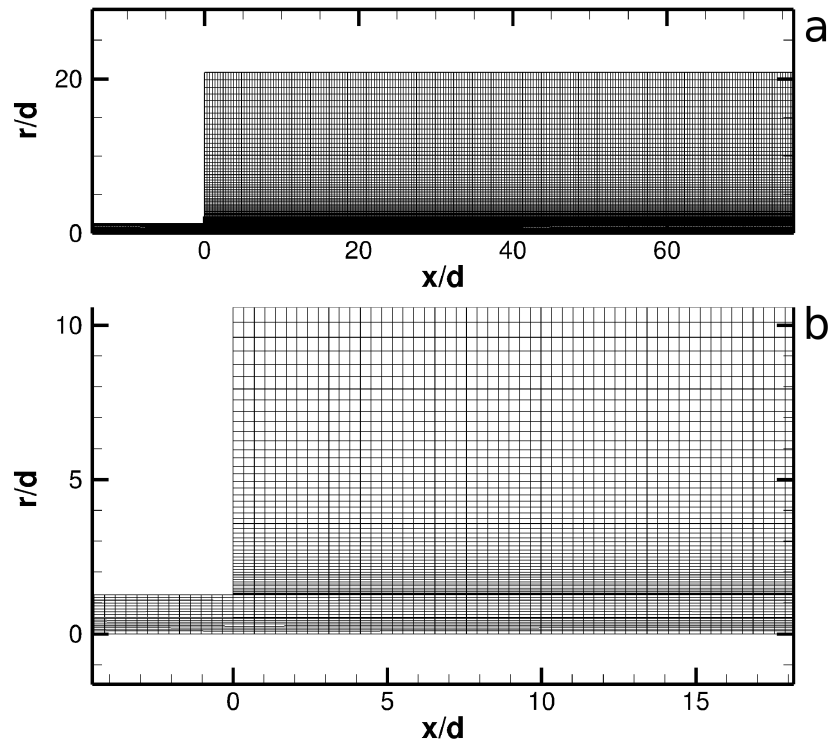

Fig. 1 General view of the computational domain (a) and details of the grid near the inlet (b) for the Sandia Flame D. x and r are the domain coordinates in axial and radial direction

order to obtain fully-developed turbulent velocity profiles. Uniform velocity profiles were specified for the jet, pilot and co-flow. All radial and circumferential velocity components were set to be zero. The inflow temperatures were set based on the experimental settings. The exit pressure was specified to 10^5 Pa at the outlet, and zero-gradient pressure was imposed at the inlet boundaries. A non-slipping condition for velocity was applied for all walls. Wall-functions were set for k and ϵ. The temperature at the walls was calculated according to the zero gradient boundary condition. The fuel jet, pilot and co-flow compositions were specified in terms of the species mass fractions calculated from the experimental data. Marshak's boundary conditions [41], based on solutions of Legendre polynomials of odd order, were adopted for radiative heat flux calculations.

4.3 LES grids and boundary conditions

Two grids (termed hereafter LES-A1 and LES-A2) were used in this study for LES. The axial and radial dimensions of the computational domain for the A1 grid (Fig. 2) were set to $139 \times d$ and $20.83 \times d$, respectively. The resolution of the A1 grid was $240 \times 60 \times 90$ in the axial, radial and circumferential directions with the grid clustering applied to the jet and pilot with the purpose to resolve the strong gradients that arise near the inlet. Both, the jet pipe and the pilot were resolved with 18 cells in the radial direction. LES-A1 mesh was designed without any pre-inlets.

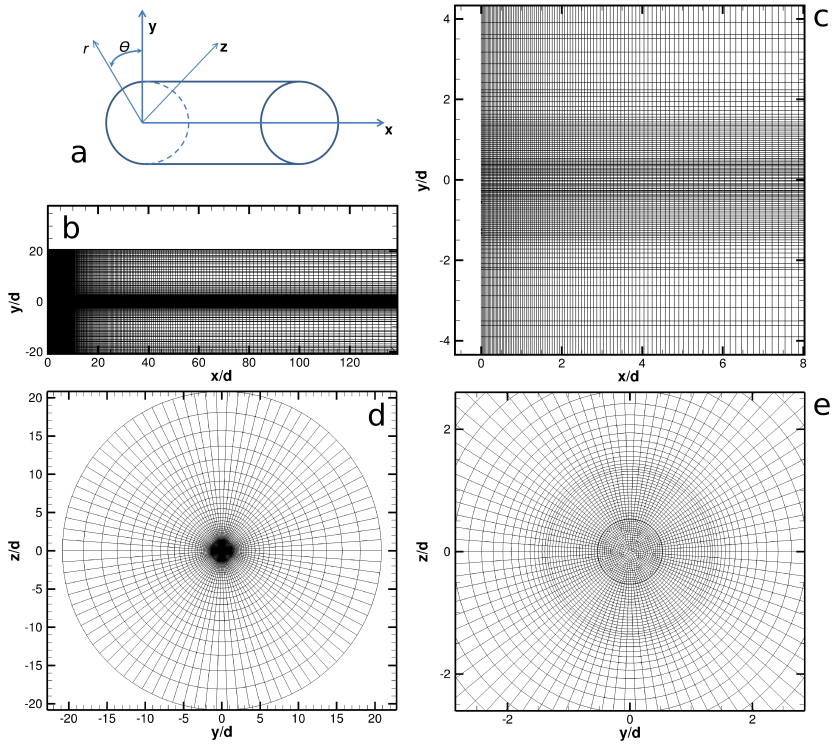

Fig. 2 Details of the LES-A1 grid: general scheme (a), description of the grid in $x-y$ (b) and $y-z$ (d) planes and zoom of the grid in $x-y$ (c) and $y-z$ (e) planes for the Sandia Flame D. x, y and z are the domain coordinates in stream-wise, transverse and span-wise directions, θ ans r are the circumferential and radial coordinates, respectively

The A2 grid (Fig. 3) was designed with the purpose to investigate the effect of the inlet boundary conditions. The axial and radial dimensions of the computational domain for the A2 grid were set to $72.5 \times d$ and $20.83 \times d$ with the subsequent resolution of $460 \times 80 \times 80$ in the axial, radial and circumferential

directions. The pre-inlet section of the grid for the jet, pilot and co-flow (Fig. 2c) had the axial length of $8.05 \times d$ with the uniform axial spacing with 120 cells. The jet pipe, the pilot and co-flow were resolved with 20, 20 and 40 cells in the radial direction, respectively. The grid clustering was applied in radial direction to resolve strong shear layers between jet, pilot and co-flow.

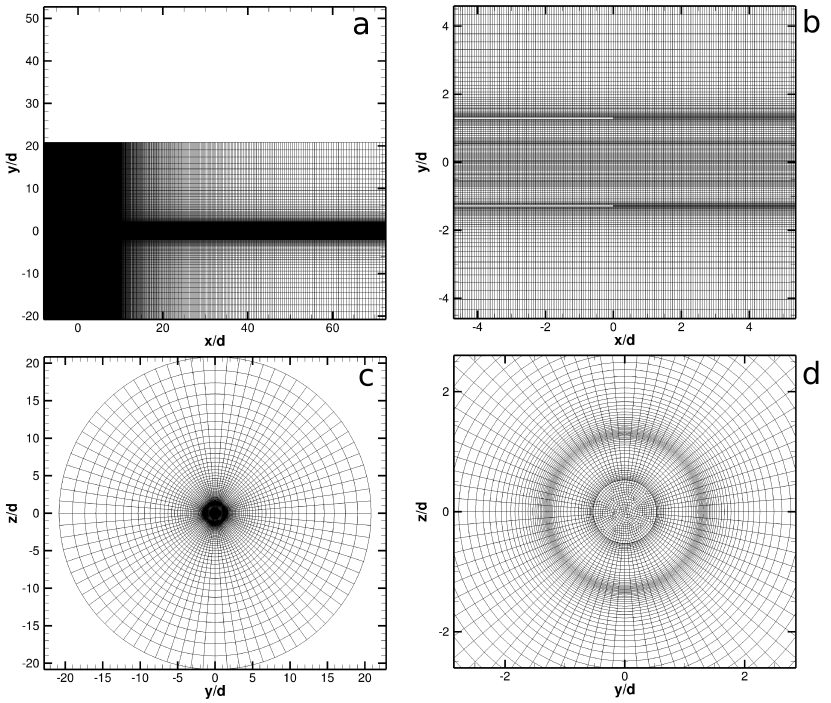

Fig. 3 Details of the LES-A2 grid: description of the grid in $x-y$ (a) and $y-z$ (c) planes and zoom of the grid in $x-y$ (b) and $y-z$ (d) planes for the Sandia Flame D

5 Results and discussion

5.1 Present predictions

All simulated cases are listed in Table 1 (where the following abbreviations are used: C – code OF or AF, TM – turbulence model (SKE or TKE), TCM – turbulence-chemistry interaction model (EDC or β-PDF), CH – chemistry mechanism, R – radiation sub-model, M – mesh).

Time-averaged results from the simulations are discussed and compared with the experimental data by Schneider et al. [51], who performed LDV veloc-

Table 1 Run matrix

Run	C	TM	TCM	CH	R	M
ke-EDC-GLB	OF	SKE	EDC	Single Step	P1	RAS-A2
ke-EDC-GRI3	OF	SKE	EDC	GRI3.0	P1	RAS-A2
ke-β-PDF	AF	SKE	β-PDF	–	P1	RAS-A2
A1-LES-EDC-GLB	OF	TKE	EDC	Single Step	P1	LES-A1
A2-LES-EDC-GLB	OF	TKE	EDC	Single Step	P1	LES-A2
A1-LES-β-PDF	AF	TKE	β-PDF	–	P1	LES-A1

ity measurements, and Barlow and Frank [2], who measured the temperature and the concentrations of chemical species. The averages have been obtained from the computational results by sampling over two flow-through times for RAS and $10 - 15$ flow-through times for LES, where the flow-through time is defined as the ratio between the axial length of the computational domain to the jet bulk velocity. Hereafter, the time-averaging operator is denoted by $\langle\rangle$. The tilde mark denoting Favre-averaging (or filtered Favre-averaging) is omitted for the simplicity.

5.2 RAS results

Fig. 4 displays axial and radial distributions of the mean axial velocities. In general, good agreement between predictions and experimental data could be observed. One can see, that the present results under-estimated to some extent the jet velocity along the central axis. The divergence between the β-PDF approach and the measured data was more significant and could be possibly explained by the compressibility effects. Hewson and Kerstein [21] carried out a detailed investigation of such phenomena and suggested that the dilatation of the flow was a possible explanation for these discrepancies. According to Hewson and Kerstein [21] dilatation pushes the fluid downstream leading to higher mixture fractions on the axis and affecting the dissipation rate. Agreement between calculations and measurement along the centerline as well as between radial profiles at $x/d = 7.5$ was very satisfactory. At $x/d = 30$ and $x/d = 45$ the calculated velocities were slightly lower (especially for the assumed β-PDF approach) compared to the experimental data which indicated that the decay of the jet was under-estimated and can be explained by using the standard k-ϵ model with a not-corrected $C_{\epsilon 1}$ constant [47],[42].

A comparison of the predicted flame temperatures is displayed in Fig. 5. Scalar data are presented in Fig. 6. Along the central axis, the peak mean temperature agreed well with the experimental data. The maximum peak temperatures obtained by all runs $\langle T_p \rangle = 1955 - 1960$ K matched well the measured peak temperature $\langle T_p \rangle = 1945$ K. One can observe a small shift between predicted and measured peak locations approximately of $6 \times d$ for the β-PDF approach which can be explained by the dilatation effect [21]. The worst prediction was obtained by the EDC-based approach where the single-step chemistry was used.

The calculated mean species $\langle Y_{O2}\rangle$, $\langle Y_{N2}\rangle$, $\langle Y_{H2}\rangle$, $\langle Y_{H2O}\rangle$, $\langle Y_{CO2}\rangle$, $\langle Y_{CO}\rangle$ and $\langle Y_{CH4}\rangle$ by the EDC-based approach with the GRI3.0 chemistry had the similar behavior as the mean temperature and reasonably agreed with the experimental data. Strong deviations were observed only for $\langle Y_{OH}\rangle$, $\langle Y_{NO}\rangle$ which showed only the correct trends.

The production of NO is highly dependent on temperature. Thus, one of the possible reasons for such discrepancies may be the incorrect treatment of radiation which can have a significant effect on the predicted NO levels [12]. In the present study an optically thin assumption was used for the treatment of the radiative losses. Frank et al. [12] showed that the optically thin radiation sub-model did not accurately predict the radiant fraction for this flame which reflects the complexity of the NO formation process. Based on spectral characteristics of the radiant emission and transmittance, they found that an optically thin assumption was inappropriate for partially premixed CH_4/air jet flames. Thus, it will be interesting in future work to calculate this flame with another radiation sub-model.

Prediction of OH in any combustion simulation is particularly challenging due to the strong nonlinearity of the species evolution [48]. The level of agreement displayed by OH was reasonable good, however the calculated maximum mass fraction was over-predicted significantly compared with the respected measured data.

In general, the predictions of the flame was in good agreement with the reported measurements. It should also be noted that the choice of the detailed chemical reaction mechanism affects the prediction of the peak values and peak positions of the scalars, especially minor species, such as CO, OH an NO [33]. In this study, the full GRI-Mech 3.0 mechanism [4] was used. Choosing another chemical kinetic mechanism with the same level of detail would have given slightly different predictions but minor differences for the major species and the temperature [59].

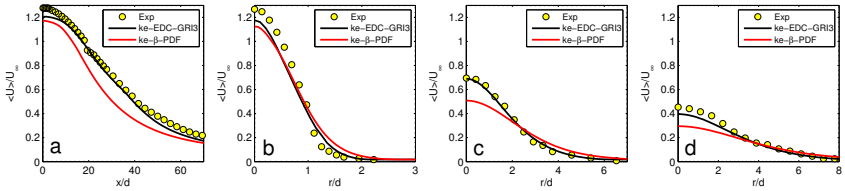

Fig. 4 Comparison of predicted and measured mean axial velocity along the axis (a) and at $x/d = 7.5$ (b), $x/d = 30$ (c) and $x/d = 45$ (d) for the Sandia Flame D

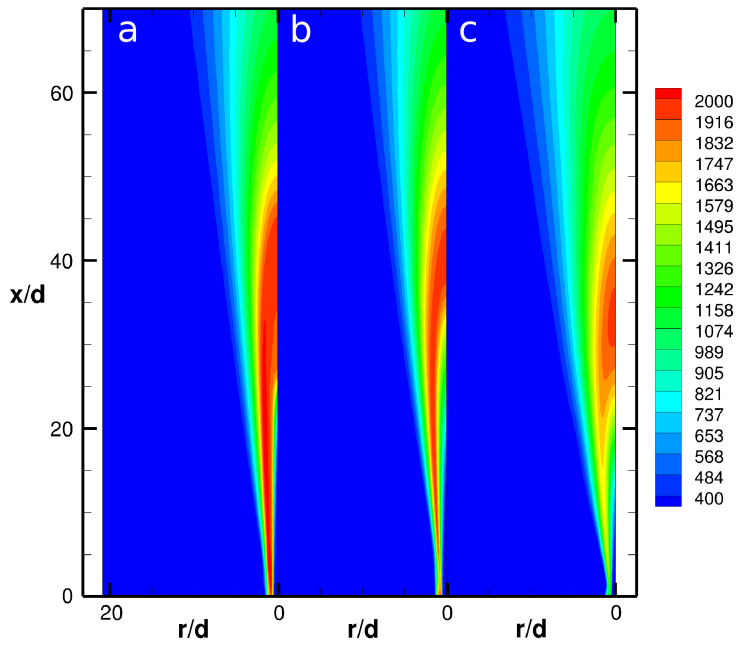

Fig. 5 Iso-contours of mean temperature (K) for the Sandia Flame D: ke-EDC-GLB (a), ke-EDC-GRI3 (b) and ke-β-PDF (c)

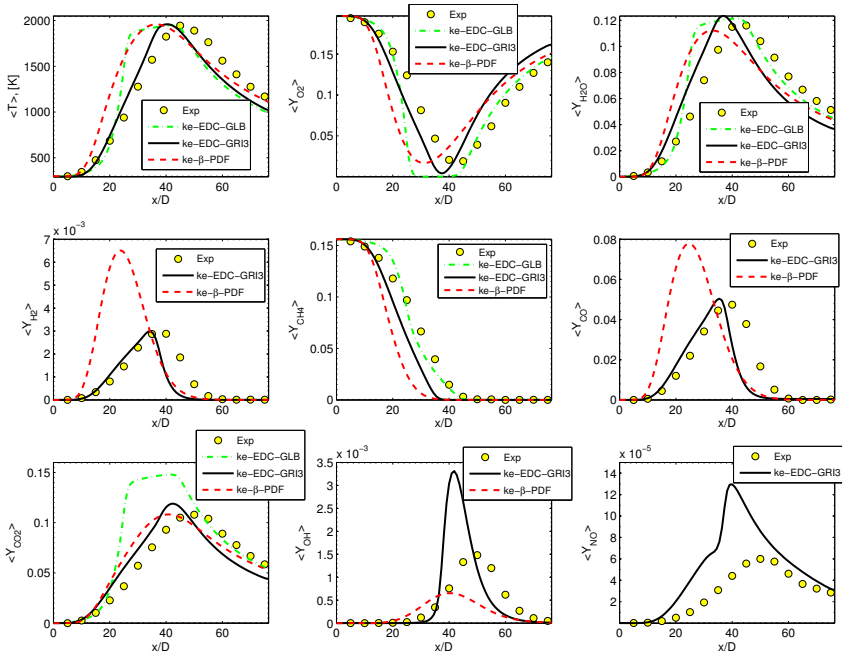

Fig. 6 Influence of the turbulence-chemistry interaction model for the Sandia Flame D: mean temperature and mean composition profiles along the axis

5.3 LES results

Fig. 7a,b shows instantaneous temperature fields of the computed flow. Fig. 7c gives an overview of the local coherent structures visualized by means of λ_2 (defined according to Jeong and Hussain [28]) at the same instance. It is interesting to note that close to the nozzle, the region around the reaction zone was dominated by the molecular diffusion and hardly showed turbulent motion and might be regarded as being laminar [45]. This phenomena has been found in many experiments and can be explained by the fact that fuels with Lewis numbers different from unity were sources of strong differential diffusion effects, which could survive even far downstream of the transition to turbulence [45],[46]. Further downstream, the formation of large-scale coherent structures took place due to the growth of perturbations. The iso-surface of λ_2 identified the vortex cores that originate from the roll-up of the shear layer between jet flow and pilot and between pilot and co-flow which are convected further downstream by the mean flow.

Figs. 8-9 compare one-dimensional Fourier energy spectra and one-dimensional wavelet energy spectra (illustrates the time-frequency evolution of the scalogram) extracted from the run A2-LES-EDC-GLB at downstream locations ($x/d = 10$ and $x/d = 20$) on the centerline of the wake. The spectral analysis was done in the same manner as in our previous work [37]. One can see that the flow near the axial location $x/d = 10$ was mostly laminar and became turbulent further downstream ($x/d = 20$). The inertial subrange was reproduced clearly for a large spectral range, assuming that sub-grid modeling was not over-dissipative and the flow was fully turbulent at $x/d = 20$. Moreover, the spectra were also consistent with the presence of small scales that can be observed clearly at the scalogram displayed in Fig. 9.

The mean axial velocity and its root-mean-square (RMS) values along the centerline are displayed in Fig. 10. All runs were in reasonable agreement with the experimental data, although the RMS values obtained by the EDC-based approach seem to be under-predicted in the core region of the jet where combustion takes place. However, such discrepancies could be explained by the the nature of the applied inlet boundary condition, insufficient grid resolution and the effects of the applied TVD schemes leading to the limited resolution of the finest scales.

A strange peak in the mean axial velocity distribution obtained by A2-LES-EDC-GLB was observed in Fig. 10a located somewhere between $20 \times d$ and $30 \times d$. This unphysical behavior, probably, could be explained by the design of the A2 grid. Indeed, the A2 grid had the uniform cell distribution along the axis up to $x/d \sim 10$ whereupon the sudden grid expansion (coarsening) started. It is well known that spurious solution oscillations could be observed quite often while numerical approximation of compressible flow equations on non-uniform grids [37].

The calculated mean temperature and mean mass fractions of O_2, N_2, CH_4, CO_2 and H_2O and their RMS values along the centerline are shown in Figs. 11-12. In general all profiles agreed reasonably with the experimental data. The

mean temperature profiles collapsed well with the experimental data for all runs. However, it seems that transition to the turbulence was slightly delayed by A2-LES-EDC-GLB and A1-LES-β-PDF. The predicted fluctuations of the temperature matched reasonably the experimental data. One can observe some discrepancies between predicted and measured values of the temperature RMS around the first peak (approximately at $x/d = 30$) caused mainly due to sudden heat release and expansion of the gases near the nozzle which leads to the production of momentum and turbulence kinetic energy.

Agreement between simulations and measured data for the RMS values of N_2, O_2, CH_4 and H_2O was reasonable. Behavior of these species have the same trend as for the temperature. The profiles of the RMS values for composition along the axis replicated the behavior of the temperature RMS. The mean mass fraction of CO_2 was slightly over-predicted by both runs.

Fig. 13 shows scatter plots of the temperature as a function of mixture fraction by the experiment and the assumed β-PDF approach at three axial distances. The experimental conditional mean of the temperature is shown in Fig. 13 as well. Overall, the agreement between calculations and the experiment was good. One can observe that the maximum temperature at $x/d = 7.5$ was under-predicted by approximately 200 K. The match between the predicted and conditional mean temperatures was good up to $\langle f \rangle = 0.5$ and $\langle f \rangle = 0.3$ at $x/d = 30$ and $x/d = 45$, respectively. It is interesting to note that the deviations between the LES-based and the URANS-based results for the β-PDF approach were minimum.

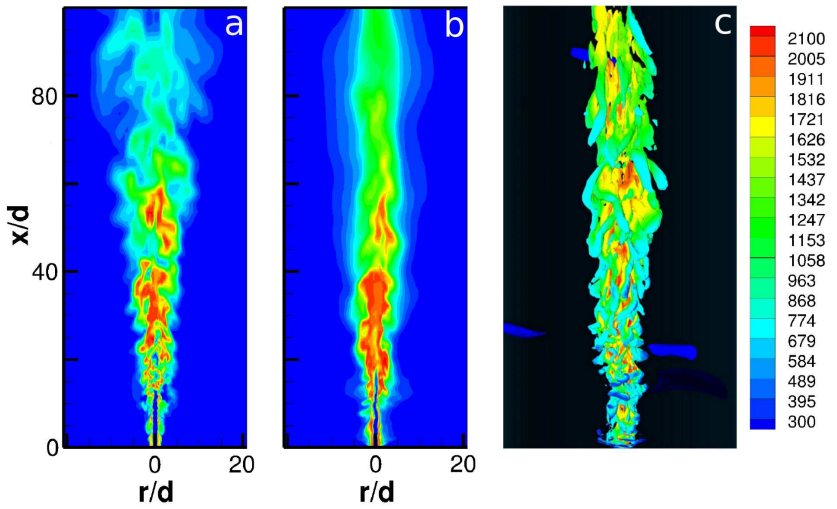

Fig. 7 Instantaneous iso-surfaces of temperature (K) obtained by A1-LES-β-PDF (a), A1-LES-EDC-GLB (b) and λ_2 visualization (colored by temperature) by A1-LES-EDC-GLB (c) for the Sandia Flame D

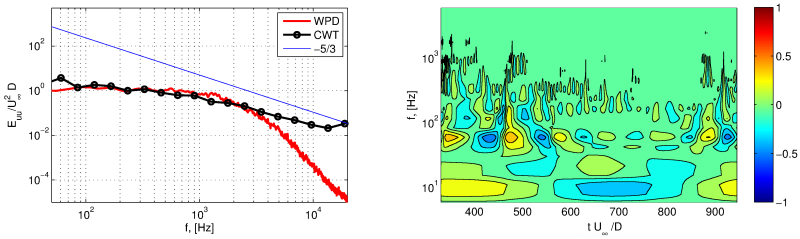

Fig. 8 Fourier power spectra (WPD) and wavelet coefficient energy (CWT) with its associated scalogram of the axial velocity at $x/d = 10$ obtained by A2-LES-EDC-GLB for the Sandia Flame D

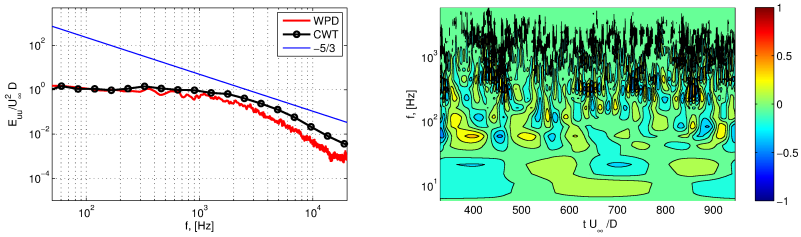

Fig. 9 Fourier power spectra (WPD) and wavelet coefficient energy (CWT) with its associated scalogram of the axial velocity at $x/d = 20$ obtained by A2-LES-EDC-GLB for the Sandia Flame D

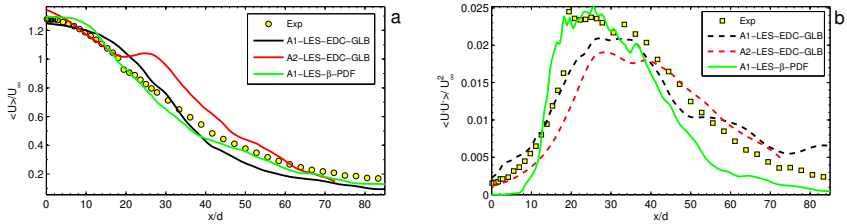

Fig. 10 Mean axial velocity (a) and its fluctuations (b) along the axis for the Sandia Flame D

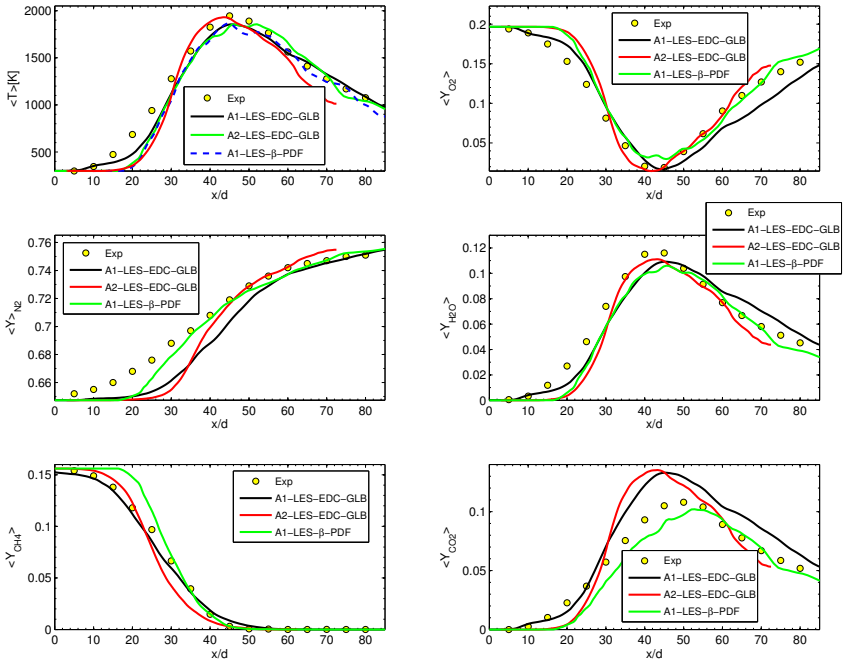

Fig. 11 Mean temperature and composition along the axis for the Sandia Flame D

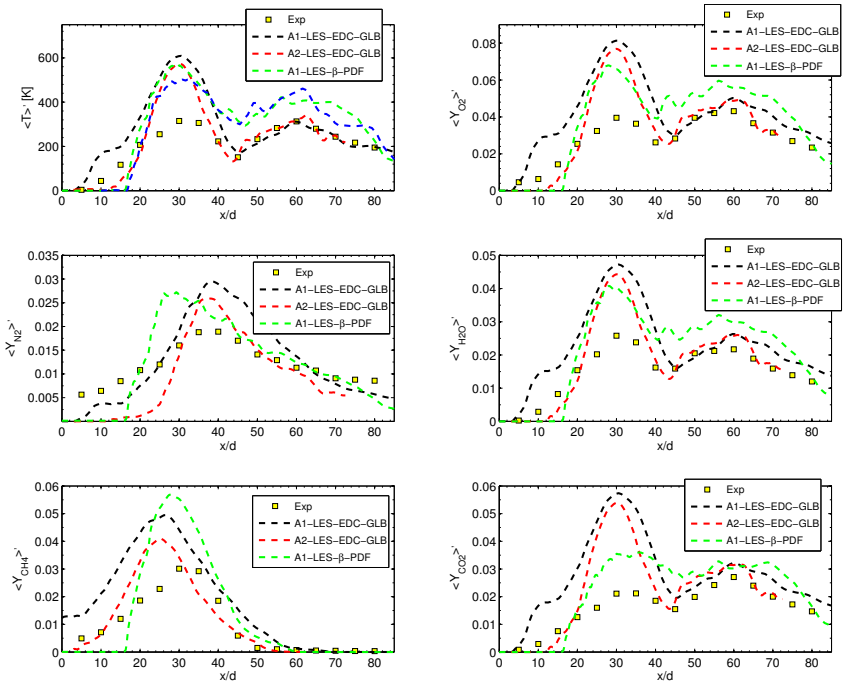

Fig. 12 Fluctuations of mean temperature and composition along the axis for the Sandia Flame D

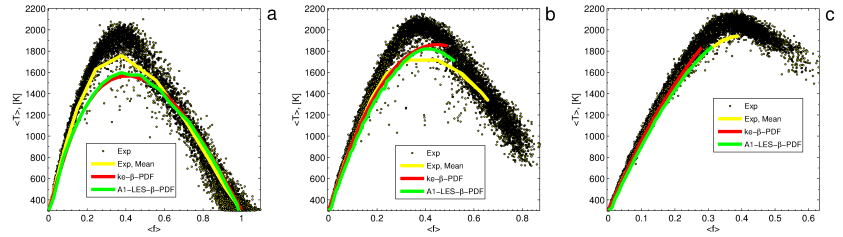

Fig. 13 Scatter plots of temperature versus mixture fraction at three axial locations $x/d = 7.5$ (a), $x/d = 30$ (b) and $x/d = 45$ (c) for the Sandia Flame D

6 Concluding remarks

The Eddy Dissipation Concept, which has been successfully used in RANS/URANS calculations of turbulent flames has been formulated as a combustion model for the large-eddy simulations and implemented in the OpenFOAM toolbox. The model has been applied both for RAS and LES of the turbulent methane/air combustion for the Sandia flame D. The assumed β-PDF approach was used as well to check the influence of modeling of the turbulence-chemistry interaction. The EDC-based and the β-PDF-based results were compared to the experimental data. It is important, that the present results were obtained without any adjustment or calibration of the model constants and agreement was quite reasonable for all quantities for both RAS and LES predictions. The remaining differences have been discussed. It is believed that one of the main reasons for the observed discrepancies between the RAS predictions and experimental data was the round-jet anomaly of the standard k-ϵ turbulence model. The lack of the grid resolution and the insufficient inlet boundary conditions can be considered as the main limitations for the present LES.

Acknowledgements This work was conducted as a part of the CenBio Center for environmentally-friendly energy. The authors would like to thank the Norwegian Meta center for Computational Science (NOTUR) for providing the uninterrupted HPC computational resources and the useful technical support. The authors also gratefully acknowledge the useful correspondence with the reviewers including their suggestions for improvements of this paper.

References

1. ANSYS FLUENT R12. Theory guide. Tech. rep., Ansys Inc. (2009)
2. Barlow, R. S. and Frank, J. H., Effects of turbulence on species mass fractions in methane/air jet flames, Proc. Combust. Inst. 27, 1087–1095 (1998)
3. Barlow, R. S., Fiechtner, G. J., Carter, C. D., and Chen, J.-Y., Experiments on the Scalar Structure of Turbulent CO/H2/N2 Jet Flames, Combust. Flame, 120, 549-569 (2000)
4. Bowman, C.T., Hanson, R.K., Davidson, D.F., Gardiner, W.C., Lissianski, V., Smith, G.P., Golden, D.M., Frenklach, M., Goldenberg, M.: GRI-Mech (2008). http://www.me.berkeley. edu/gri-mech/. Accessed February 2013
5. Chase, M., NIST-JANAF Thermochemical tables, 4th Ed., J. Phys. Chem. Ref. Data, Monographs and Supplements, 9 (1998)
6. Cheng, P., Dynamics of a radiating gas with application to flow over a wavy wall, AIAA Journal, 4(2), 238-245 (1966)
7. Dally, B.B., Masri, A.R., Barlow, R.S. and Fiechtner, G.J., Instantaneous and mean compositional structure of bluff- body stabilised nonpremixed flames. Combust. Flame, 114, 119–148 (1998)
8. Dunn, M. J., Masri, A. R. and Bilger, R. W., A new piloted premixed jet burner to study strong finite-rate chemistry effects, Combust. Flame 151(1-2), 46–60 (2007)
9. Dunn, M. J., Masri, A. R., Bilger, R. W., Barlow, R. S. and Wang, G. H., The compositional structure of highly turbulent piloted premixed flames issuing into a hot coflow, Proc. Combust. Inst. 32(2), 1779–1786 (2009)
10. Ertesvåg, I. S. and Magnussen, B. F., The eddy dissipation turbulence energy cascade model, Combust. Sci. Technol. 159, 213–235 (2000)
11. Feymark, A., Alin, N., Bensow, R., Fureby, C., Numerical simulation of an oscillating cylinder using large eddy simulation and implicit large eddy simulation, J. Fluids Eng., 134, 031205 (2012)

12. Frank, J.H., Barlow, R.S., Lundquist, C., Radiation and nitric oxide formation in turbulent non-premixed jet flames, Proc. Comb. Inst, 28, 447–454 (2000)
13. Garnier, E., Adams, N., Sagaut, P., Large Eddy Simulation for Compressible Flows. Springer, New York (2009)
14. Germano, M., Piomelli, U., Moin, P., Cabot, W.H., Dynamic subgrid-scale eddy viscosity model, In Summer Workshop, Center for Turbulence Research, Stanford, CA (1996)
15. Geurts, B., Elements of direct and large-eddy simulation, R.T.Edwards, Philadelphia (2004)
16. Gordon, S., McBride, B.J., Computer Program for Calculation of Complex Equilibrium Composition, Rocket Performance, Incident and Reflected Shocks and Chapman-Jouguet Detonations, NASA SP-273 (1971)
17. Gran, I. R. and Magnussen, B. F., A numerical study of a bluff-body stabilized diffusion flame. Part 2. Influence of combustion modeling and finite-rate chemistry, Combust. Sci. Technol. 119, 191-217. (1996)
18. Hairer, E. and Wanner, G., Solving ordinary differential equations II: Stiff and differential-algebraic problems, Springer Series in Computational Mathematics, 2nd rev. ed, Springer-Verlag (1996)
19. Harten, A., High resolution schemes for hyperbolic conservation laws, J. Comput. Phys., 49, 357-393 (1983)
20. Hestens, M, Steifel, E., Methods of conjugate gradients for solving systems of algebraic equations, J. Res. Nat. Bur. Stand, 29, 409–436 (1952)
21. Hewson, J.C., Kerstein, A.R., Stochastic simulation of transport and chemical kinetics in turbulent CO/H2/N2 flames. Combust. Theory Model., 5, 669-897 (2001)
22. Hossain, M., Jones, J.C., Malalasekera, W., Modelling of a bluff-Body nonpremixed flame using a coupled radiation/flamelet combustion model, Flow Turbul. Combust., 67, 217–234 (2001)
23. Hottel, H. C, and Sarofim, A.F., Radiative Transfer, McGraw-Hill, New York (1967)
24. Hutchinson, B., Raithby, G., A multigrid method based on the additive correction strategy. J Numer Heat Transfer, 9, 511–37 (1986)
25. Issa, R., Solution of the implicitly discretized fluid flow equations by operator splitting, J. Comput. Phys., 62, 40–65 (1986)
26. Jacobs, D., Preconditioned conjugate gradient methods for solving systems of algebraic equations, Tech. rep., Central Electricity Research Laboratories, Leatherhead, Surrey, England (1980)
27. Jasak, H., Weller, H.G., Gosman A.D., High resolution NVD differencing scheme for arbitrarily unstructured meshes, Int. J. Numer. Meth. Fluids, 31, 431–449 (1999)
28. Jeong, J., Hussain, F., On the identification of a vortex, J. Fluid Mech. 285, 69–94 (1995)
29. Jones, W.P., Whitelaw, J.H., Calculation methods for reacting turbulent flows: a review, Combust. Flame, 48, 1-26 (1982)
30. Jones, W.P., Prasad V.N., Large eddy simulation of the Sandia Flame Series (D-F) using the Eulerian stochastic field method, Combust. Flame, 157, 1621-1636 (2010)
31. Launder, B. E. and Spalding, D. B., The numerical computation of turbulent flows, Comput. Method Appl. M. 3(2), 269–289 (1974)
32. Lilleberg, B., On mathematical modeling and numerical simulation of chemical kinetics in turbulent lean premixed combustion, PhD thesis, Norwegian University of Science and Technology, 2011:206, Trondheim (2011)
33. Lilleberg, B., Christ D., Ertesvåg, I.S., Rian, K.E., Kneer, R., Numerical Simulation with an Extinction Database for Use with the Eddy Dissipation Concept for Turbulent Combustion, Flow Turbul. Combust., 91, 319-346 (2013)
34. Lilly, D.K., A proposed modification of the Germano subgrid scale closure model, Phys. Fluids, 4, 633-635 (1992)
35. Lysenko, D.A., Ertesvåg, I.S., Rian, K.E., Modeling of turbulent separated flows using OpenFOAM, Comput. Fluids, 80, 408-422 (2013)
36. Lysenko, D.A., Ertesvåg, I.S., Rian, K.E., Large-eddy simulation of the flow over a circular cylinder at Reynolds number 3900 using the OpenFOAM toolbox, Flow Turbul. Combust., 89, 491–518 (2012)

37. Lysenko, D.A., Ertesvåg, I.S., Rian, K.E., Large-eddy simulation of the flow over a circular cylinder at Reynolds number 2×10^4, Flow Turbul. Combust., DOI 10.1007/s10494-013-9509-1
38. Lysenko, D.A., Ertesvåg, I.S., Rian, K.E., Lilleberg, B., Christ D., Numerical simulation of turbulent flames using the Eddy Dissipation Concept with detailed chemistry, In: Skallerud B, Andersson HI, editors. Computational mechanics, Trondheim; pp. 159–178 (2013)
39. Magnussen, B.F., Hjertager, B.H., On mathematical modeling of turbulent combustion with special emphasis on soot formation and combustion, Proc. Combust. Inst. 16, 719–729 (1976)
40. Magnussen, B.F., Modeling of NOx and soot formation by the Eddy Dissipation Concept. Int.Flame Research Foundation, 1st topic Oriented Technical Meeting., 17-19 Oct. 1989. Amsterdam, Holland
41. Marshak, R.E. Note on the spherical harmonics method as applied to the Milne problem for a sphere, Phys. Rev., 71, 443-446 (1947)
42. McGuirk, J.J., Rodi, W., The calculation of three-dimensional turbulent free jets. In turbulent Shear Flows I: Selected papers from the First International Symposium on Turbulent Shear Flows, editors: Durst, F., Launder, B.E., Schmidt, F.W., and Whitelaw, J.H., Springer-Verlag, Germany, 71-83 (1979)
43. Nik, M.B., Yilmaz, S.L., Givi, P., Sheikhi, M.R.H., Pope, S.B., Simulation of Sandia Flame D Using Velocity–Scalar Filtered Density Function, AIAA J., 48(7), 1513-1522 (2010)
44. Panjwani, B., Large eddy simulation of turbulent combustion with chemical kinetics, PhD thesis, Norwegian University of Science and Technology, 2011:73, Trondheim (2011)
45. Pitsch, H., Steiner, H., Large-eddy simulation of a turbulent piloted methane/air diffusion flame (Sandia Flame D), Phys. Fluids, 12(10), 2541-2554 (2000)
46. Pitsch, H., Unsteady flamelet modeling of differential diffusion in turbulent jet diffusion flames Original Research Article, Combust. Flame, 123(3), 358-374 (2000)
47. Pope, S.B., An explanation of the turbulent round-jef/plane-jet anomaly, AIAA J., 16, 279-281 (1978)
48. Raman, V., Pitsch, H., Fox, R.O., Hybrid large-eddy simulation/Lagrangian filtered-density-function approach for simulating turbulent combustion, Comb. Flame, 143, 56-78 (2005)
49. Rhie, C., Chow, W., Numerical study of the turbulent flow past an airfoil with trailing edge separation. AIAA J, 21, 1525–32 (1983)
50. Sagaut, P., Large Eddy Simulation for Incompressible Flows, 3rd ed., Springer Berlin, 2006
51. Schneider, C., Dreizler, A., Janicka, J., Hassel, E.P., Flow field measurements of stable and locally extinguishing hydrocarbon-fueled jet flames, Combust. Flame 135, 185–190 (2003)
52. Sivathanu, Y.R., Faeth, G.M., Generalized state relationships for scalar properties in non-premixed Hydrocarbon/Air flames, Combust. Flame, 82, 211-230 (1990)
53. Smith, T.F., Shen, Z.F. and Friedman, J.N. , Evaluation of coefficients for the weighted sum of gray gases model, J. Heat Trans-T., ASME 104(4), 602–608 (1982)
54. Vandoormaal, J.P., Raithby, G.D., Enhancements of the SIMPLE method for predicting incompressible fluid flows, Numer. Heat Transfer, 7, 147–163 (1984)
55. Warnatz, J., Maas, U., Dibble R.W., Combustion, 4th ed. Springer. Berlin Heidelberg New York (2006)
56. Waterson, N.P., Deconinck, H., Design principles for bounded higher-order convection schemes – a unified approach, J Comput. Phys., 224, 182–207 (2007)
57. Weller, H.G., Tabor, G., Jasak H., Fureby, C., A tensorial approach to computational continuum mechanics using object-oriented techniques, Comp. Phys., 12(6), 620–631 (1998)
58. Yoshizawa, A., Statistical theory for compressible shear flows, with the application to subgrid modelling, Phys. Fluids 29(2152), 1416-1429 (1986)
59. Zahirović, S., Scharler, R., Kilpinen, P., Obernberger, I.: Validation of flow simulation and gas combustion sub-models for the CFD-based prediction of NOx formation in biomass grate furnaces, Combust. Theory Model., 15, 61–87 (2011)